A Wavelet-Based Method for Multifractal Image Analysis: From Theoretical Concepts to Experimental Applications

A. ARNÉODO,[1] N. DECOSTER,[2] P. KESTENER,[1] AND S. G. ROUX[3]

[1]*Centre de Recherche Paul Pascal, Avenue Schweitzer, 33600, Pessac, France*
[2]*Noveltis, Parc Technologique du Canal, 2 avenue de l'Europe, 31520, Ramonville Saint Agne, France*
[3]*Laboratoire de Physique, Ecole Normale Supérieure de Lyon, 46 allée d'Italie, 69364, Lyon cedex 07, France*

ISSN 1076-5670/03

I. Introduction

Ever since the explosive propagation of fractal ideas [1,2] throughout the scientific community in the late 1970s and early 1980s, there have been numerous applications to surface science [3–13]. Both real space imaging techniques (including scanning tunneling microscopy, atomic force microscopy, transmission electron microscopy, secondary electron microscopy, and optical imaging techniques) and diffraction techniques (including electron, atom, light, and X-ray scattering) have been extensively used to study rough surfaces [12]. The characterization of surface roughness is an important problem from a fundamental point of view as well as for the wealth of potential applications in applied sciences. Indeed, a wide variety of natural and technological processes lead to the formation of complex interfaces [1–18]. Assigning a fractal dimension to those irregular surfaces has now become routine in various fields including topography, defect and fracture studies, growth phenomena, erosion and corrosion processes, catalysis, and many other areas in physics, chemistry, biology, geology, meteorology, and material sciences [1–18]. For *isotropic* and *self-similar* interfaces when magnified equally in all directions, algorithms (e.g., box-counting algorithms, fixed-size and fixed-mass correlation algorithms) were designed and shown to provide a good estimate of the fractal dimension D_F [19–27]. For rough surfaces that are well described by *self-affine* fractals displaying *anisotropic* scale invariance [1,2,4,5,7,28–31], various methods (e.g., divider, box, triangle, slit-island, power spectral, variogram, and distribution methods) of computing D_F were shown to give different results [32–36]. Limited resolution as well as finite-size effects are well known for introducing biases in the estimate of D_F, which are indeed method dependent [32,36,37]. For a documented discussion of the possible reasons for these differences in fractal dimension measurements, we refer the reader to the review article of Lea-Cox and Wang [38]. An alternative strategy consists in computing the so-called *roughness exponent* H [1,2,4,7] that describes the scaling of the width (or thickness) of the rough interface with respect to measurement scale. Different methods (e.g., height–height correlation function, variance and power spectral methods, detrented fluctuation analysis, first return and multireturn probability distributions) [33–36,39–42] are available to estimate this exponent that is supposed to be related to the fractal dimension $D_F = d - H$ of self-affine surfaces embedded in a d-dimensional space. Again a number of artifacts may pollute the estimate of the roughness exponent [36]. Since sensitivity and accuracy are method dependent, the usually recommendation is to simultaneously use different tools in order to appreciate, in a quantitative way, the level of confidence in the measured exponent.

But beyond some practical algorithmic limitations, there exists a more fundamental intrinsic insufficiency of fractal dimension measurement in the sense that the fractal dimension D_F as well as the roughness exponent H are global quantities that do not account for possible fluctuations (from point to point) of the local regularity properties of a fractal surface. Box-counting and correlation algorithms were successfully adapted to resolve *multifractal* scaling for isotropic self-similar fractals by computation of the *generalized fractal dimensions* D_q [20–26]. As to self-affine fractals, Parisi and Frisch [43] proposed, in the context of the analysis of fully developed turbulence data, an alternative multifractal description based on the investigation of the scaling behavior of the so-called structure functions [18,44]: $S_p(l) = <(\delta f_l)^p> \sim l^{\zeta_p}$ (p integer > 0), where $\delta f_l(x) = f(x+l) - f(x)$ is an increment of the recorded signal over a distance l. Then, after reinterpreting the roughness exponent as a local quantity [43,45–49]: $\delta f_l(x) \sim l^{h(x)}$, the $D(h)$ *singularity spectrum* is defined as the Hausdorff dimension of the set of points x where the local roughness (or Hölder) exponent $h(x)$ of f is h. In principle, $D(h)$ can be attained by Legendre transforming the structure function scaling exponents ζ_p [43,48,49]. Unfortunately, as noticed by Muzy *et al.* [50], there are some fundamental drawbacks to the structure

function method. Indeed, it generally fails to fully characterize the $D(h)$ singularity spectrum since only the strongest singularities of the function f itself (and not the singularities present in the derivatives of f) are a priori amenable to this analysis. Even though one can extend this study from integer to real positive p values by considering the increment absolute value, the structure functions generally do not exist for $p < 0$. Moreover, singularities corresponding to $h > 1$, as well as regular behavior, bias the estimate of ζ_p [48–50].

In previous work [47–50], one of the authors (A.A.), in collaboration with Bacry and Muzy, has shown that there exists a natural way of performing a multifractal analysis of self (multi)affine functions, which consists in using the *continuous wavelet transform* [51–66]. By using *wavelets* instead of boxes, as in classic multifractal formalism [24,67–71], one can take advantage of freedom in the choice of these "Generalized oscillating boxes" to get rid of possible smooth behavior that might either mask singularities or perturb the estimation of their strength h [47–50]. The other fundamental advantage of using wavelets is that the skeleton defined by the *wavelet transform modulus maxima* (WTMM) [72,73] provides an adaptative space-scale partitioning from which one can extract the $D(h)$ singularity spectrum via the scaling exponents $\tau(q)$ of some partition functions defined on the skeleton. The so-called WTMM method [47–50] therefore provides access to the entire $D(h)$ spectrum via the usual Legendre transform $D(h) = \min_q[qh - \tau(q)]$. We refer the reader to Refs. [74,75] for rigorous mathematical results. Since the WTMM method is mainly devoted to practical applications to stochastic systems, let us point out that the theoretical treatment of random multifractal functions requires special attention. A priori, there is no reason that all the realizations of the same stochastic multifractal process correspond to a unique $D(h)$ curve. Each realization has its own unique distribution of singularities and one crucial issue is to relate these distributions to some averaged versions computed experimentally. As emphasized by Hentschel [76], one can take advantage of the analogy that links the multifractal description to statistical thermodynamics [24,49,67,68,77], by using methods created specifically to study disorder in spin-glass theory [78]. When carrying out replica averages of the random partition function associated with a stochastic function, one gets multifractal spectra $\tau(q,n)$ that generally depend on the number of members n in the replica average (let us note that $n = 0$ and $n = 1$, respectively, correspond to commonly used quenched and annealed averaging [76]). Then, by Legendre transforming $\tau(q,n)$, some type of average $D(h)$ spectra is found [76]. Some care is thus required when interpreting these average spectra in order to avoid some misunderstanding of the underlying physics.

Applications of the WTMM method to one-dimensional (ID) signals have already provided insight into a wide variety of outstanding problems [62], e.g., the validation of the cascade phenomenology of fully developed turbulence [47–49,79–87], the discovery of a Fibonacci structural ordering in 1D cuts of diffusion-limited aggregates (DLA) [88–92], the characterization and the understanding of long-range correlations in DNA sequences [93–98], and the demonstration of the existence of a causal cascade of information from large to small scales in financial time series [99,100]. Let us also note that from a fundamental point of view, the WTMM multifractal formalism [47–50,74] has been recently revisited [101–104] in order to incorporate in this statistical "*canonical*" description (which applies for *cusp-like singularities* only), the possible existence of *oscillating singularities* [73,101,105]. This new "*grand canonical*" description [102–104] allows us to compute the singularity spectrum $D(h,\beta)$, which accounts for the statistical contribution of singularities of Hölder exponent h and oscillation exponent β (where β characterizes the local power-law divergence of the instantaneous frequency).

In a recent work [106–110], we have generalized the canonical WTMM method from 1D to two-dimensional (2D), with the specific goal of achieving multifractal analysis of rough surfaces with fractal dimension D_F anywhere between 2 and 3. During the past few years, increasing interest has been paid to the application of the wavelet transform (WT) to image processing [26,61,62,65,111–113]. In this context, Mallat and collaborators [72,73] have extended the WTMM representation in 2D in a manner inspired from Canny's multiscale edge detectors commonly used in computer vision [114]. Our strategy [107,108] consists of using this representation to define a three-dimensional (3D) WT skeleton from which one can compute partition functions and ultimately extract multifractal spectra. This article is mainly devoted to a detailed description of the 2D WTMM methodology with some test applications to random monofractal and multifractal self-affine surfaces displaying isotropic as well as anisotropic (with respect to space variables) scale similarity properties. As an illustration of the efficiency and reliability of this method, we will report the main results of its application to experimental 2D data in various domains, namely geophysics, hydrodynamics, and medecine.

The article is organized as follows. In Section II, we describe the 2D WTMM representation introduced by Mallat *et al.* [72,73] as the equivalent of multiscale Canny edge detection. We present the continuous WT as a mathematical microscope that is well suited for characterizing the local regularity of rough surfaces. For practical purposes, the WTMM representation is emphasized as a very efficient and accurate numerical tool for scanning the singularities of fractal landscapes. We then describe the

2D WTMM method as a natural generalization of box-counting algorithms and structure function techniques previously used for multifractal analysis of isotropic self-similar interfaces and multiaffine surfaces [107,108]. Section III is devoted to the application of the 2D WTMM method to fractional Brownian surfaces [1,2,4,28] that display isotropic (with respect to space variables) scaling properties. For this class of isotropic homogeneous random rough surfaces, we address the issues of statistical convergence and finite-size effects [108]. We illustrate the ability of the 2D WTMM method to reveal and to master anisotropic scale invariance hidden in the roughness fluctuations of a random surface. We also report the results of test applications to synthetic random multifractal rough surfaces generated with a random $\mathcal{W}$-cascade process on a separable wavelet orthogonal basis [109]. On a more general ground, we show that the 2D WTMM method can be used for many purposes in image processing including edge detection, pattern recognition, and image denoising. The next sections are devoted to the description of the most significant results obtained when applying the 2D WTMM method to three different experimental situations. In Section IV, we review the outcomes of the statistical analysis of high-resolution LANDSAT satellite images of cloudy scenes. This study brings into light the underlying multiplicative structure of marine stratocumulus clouds [107,110]. The multifractal properties of the stratocumulus radiance fields are further compared to previous experimental estimates performed on velocity and temperature fluctuations in high Reynolds number turbulence. In Section V, we report the preliminary results of the application of the 2D WTMM method to 2D cuts of the dissipation and enstrophy fields computed from direct high-resolution numerical simulations of statistically stationary 3D homogeneous and isotropic fully developed turbulent flows at a Reynolds number around 1000 ($R_\lambda \simeq 1150$). This study reveals that both fields display log-normal multifractal properties but that the enstrophy field turns out to be much more intermittent than the dissipation field. From a comparison with previous experimental investigations of 1D data, we comment about the reliability of the results obtained when using 1D surrogate dissipation data. In Section VI, we apply the 2D WTMM method to perform a multifractal analysis of digitized mammograms [115]. We show that this method can be used to classify fatty and dense areas of breast tissue. We further demonstrate that this method provides a very efficient way to detect tumors as well as microcalcifications, which correspond to much stronger singularities than those involved in the background tissue roughness fluctuations. These preliminary results indicate that the texture discriminatory power of the 2D WTMM method may lead to significant improvement in computer-assisted diagnosis in digitized mammograms. We conclude in Section VII.

II. Image Processing with the 2D Continuous Wavelet Transform

A. Analyzing Wavelets for Multiscale Edge Detection

The edges of the different structures that appear in an image are often the most important features for pattern recognition. Hence, in computer vision [116,117], a large class of edge detectors looks for points where the gradient of the image intensity has a modulus that is locally maximum in its direction. As originally noticed by Mallat and collaborators [72,73], with an appropriate choice of the analyzing wavelet, one can reformalize the Canny's multiscale edge detector [114] in terms of a 2D wavelet transform. The general idea is to start by smoothing the discrete image data by convolving it with a filter and then to compute the gradient on the smoothed signal.

Let us consider two wavelets that are, respectively, the partial derivative with respect to x and y of a 2D -smoothing function $\phi(x,y)$:

$$\psi_1(x,y) = \frac{\partial \phi(x,y)}{\partial x} \qquad \text{and} \qquad \psi_2(x,y) = \frac{\partial \phi(x,y)}{\partial y} \tag{1}$$

We will assume that ϕ is a well-localized (around $x = y = 0$) isotropic function that depends on $|\mathbf{x}|$ only. In this work, we will mainly use the Gaussian function:

$$\phi(x,y) = e^{-(x^2+y^2)/2} = e^{-|\mathbf{x}|^2/2} \tag{2}$$

as well as the isotropic Mexican hat:

$$\phi(\mathbf{x}) = (2 - \mathbf{x}^2)e^{-|\mathbf{x}|^2/2} \tag{3}$$

The corresponding analyzing wavelets ψ_1 and ψ_2 are illustrated in Figure 1. They have one and three vanishing moments when using, respectively, the Gaussian function [Eq. (2)] and the Mexican hat [Eq. (3)] as smoothing function.

For any function $f(x,y) \in L^2(\mathbb{R})$, the wavelet transform with respect to ψ_1 and ψ_2 has two components and therefore can be expressed in a vectorial form:

$$\mathbf{T}_\psi[f](\mathbf{b},a) = \left\{ \begin{array}{l} T_{\psi_1}[f] = a^{-2} \displaystyle\int d^2\mathbf{x}\ \ \psi_1[a^{-1}(\mathbf{x}-\mathbf{b})]\, f(\mathbf{x}) \\ T_{\psi_2}[f] = a^{-2} \displaystyle\int d^2\mathbf{x}\ \ \psi_2[a^{-1}(\mathbf{x}-\mathbf{b})]\, f(\mathbf{x}) \end{array} \right\} \tag{4}$$

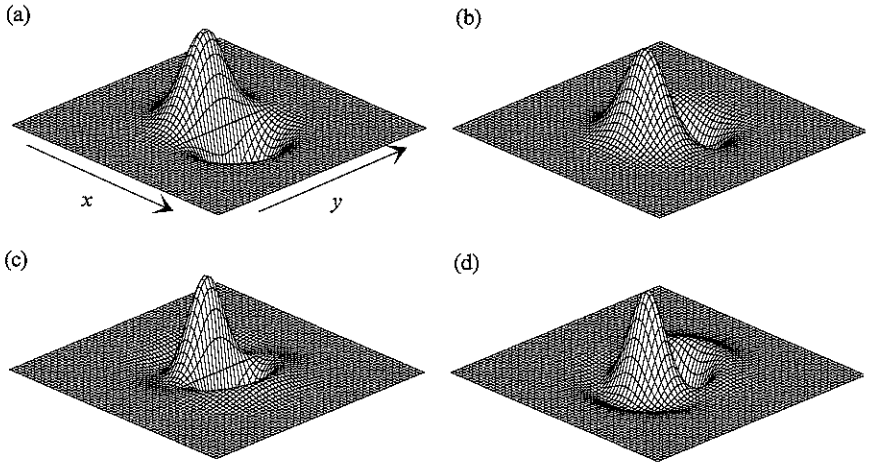

FIGURE 1. The analyzing wavelets ψ_1 and ψ_2 defined in Eq. (1). First-order analyzing wavelets obtained from a Gaussian smoothing function ϕ [Eq. (2)]: (a) ψ_1; (b) ψ_2. Third-order analyzing wavelets obtained from the isotropic Mexican hat smoothing function ϕ [Eq. (3)]: (c) ψ_1; (d) ψ_2.

Then, after a straightforward integration by parts, one gets:

$$\begin{aligned}\mathbf{T}_\psi[f](\mathbf{b},a) &= a^{-2}\nabla\left\{\int d^2\mathbf{x}\ \phi\left[a^{-1}(\mathbf{x}-\mathbf{b})\right] f(\mathbf{x})\right\} \\ &= \nabla\{T_\phi[f](\mathbf{b},a)\} \\ &= \nabla\{\phi_{\mathbf{b},a} * f\}\end{aligned} \tag{5}$$

If $\phi(\mathbf{x})$ is simply a smoothing filter like the Gaussian function [Eq. (2)], then Eq. (5) amounts to define the 2D wavelet transform as the gradient vector of $f(\mathbf{x})$ smoothed by dilated versions $\phi(a^{-1}\mathbf{x})$ of this filter. If $\phi(\mathbf{x})$ has some vanishing moments, then $T_\phi[f](\mathbf{b},a)$ in Eq. (5) is nothing but the continuous 2D wavelet transform of $f(\mathbf{x})$ as originally defined by Murenzi [118,119], provided $\phi(\mathbf{x})$ be an isotropic analyzing wavelet so that the integration over the angle θ becomes trivial.

As far as notations are concerned, we will mainly use the representation involving the modulus and the argument of the wavelet transform:

$$\mathbf{T}_\psi[f](\mathbf{b},a) = \left[\mathcal{M}_\psi[f](\mathbf{b},a), \mathcal{A}_\psi[f](\mathbf{b},a)\right] \tag{6}$$

with

$$\mathcal{M}_\psi[f](\mathbf{b},a) = \left\{\left[T_{\psi_1}[f](\mathbf{b},a)\right]^2 + \left[T_{\psi_2}[f](\mathbf{b},a)\right]^2\right\}^{1/2} \tag{7}$$

and

$$\mathcal{A}_\psi[f](\mathbf{b},a) = \mathrm{Arg}\left[T_{\psi_1}[f](\mathbf{b},a) + iT_{\psi_2}[f](\mathbf{b},a)\right] \tag{8}$$

B. *Characterizing the Local Regularity Properties of Rough Surfaces with the Wavelet Transform Modulus Maxima*

In the present work, we will use the term *rough surface* for an irregular surface on which there are no overhanging regions. This means that the surface can be correctly described by a single-valued self-affine function satisfying $\forall \mathbf{x}_0 = (x_0, y_0) \in \mathbb{R}^2, \forall \mathbf{x} = (x, y) \in \mathbb{R}^2$ in the neighborhood of $\mathbf{x}_0, \exists H \in \mathbb{R}$ such that, for any $\lambda > 0$, one has [1,2,4,5,7,28–30]:

$$f(x_0 + \lambda x, y_0 + \lambda^\alpha y) - f(x_0, y_0) \simeq \lambda^H \left[f(x_0 + x, y_0 + y) - f(x_0, y_0)\right] \tag{9}$$

If f is a stochastic process, this identity holds in law for fixed λ and $\mathbf{x}_0$. According to the value of the exponent α, this self-affine function will display either isotropic scale invariance with respect to the space variables ($\alpha = 1$) or anisotropic scale invariance ($\alpha \neq 1$) [36,120–123]. The Hurst exponent H characterizes the global regularity of the function f. Let us note that if $H < 1$, then f is nowhere differentiable and that the smaller the exponent H, the more singular f. For $H = 1$ and $\alpha = 1$, the rough surface defined by f in $\mathbb{R}^3$, is a self-similar fractal in the sense that it is invariant under some isotropic dilations [1,2,36,121–123].

In various contexts [1–18], several methods have been used to estimate the Hurst exponent of self-affine functions. In most studies, isotropic scale invariance was used as a prerequisite for the application of commonly used methods to the analysis of 1D fractal landscapes, e.g., the height–height correlation function, the variance and power spectral methods, the detrented fluctuation analysis, and the first return and multireturn probability distributions [33–36,39–42]. The strategy followed in these studies reduces the analysis of rough surfaces to the investigation of self-affine (1D) profiles obtained through 2D cuts in a three-dimensional representation. As long as the estimate of the Hurst exponent H is independent of the intersection plane, there is no inconsistency in the methodology. When H is found to be sensitive to the orientation of the intersecting plane, this means that the isotropic scale invariance hypothesis does not apply and that one needs to have recourse to methods fully adapted to the characterization of rough surfaces. Unfortunately, to our knowledge, most of the methods listed above have been extended to self-affine functions from $\mathbb{R}^2$ to $\mathbb{R}$ under the implicit assumption of isotropic scaling.

But fractal functions generally display multiaffine properties in the sense that their roughness (or regularity) fluctuates from point to point [43,45–49]. To describe these multifractal functions, one thus needs to change slightly the definition of the Hurst regularity of f so that it becomes a local quantity $h(\mathbf{x}_0)$. A rigorous definition of the *Hölder exponent* (as the strength of a singularity of a function f at the point $\mathbf{x}_0$) is given by the largest exponent $h(\mathbf{x}_0)$ such that there exists a polynomial of degree $n < h(\mathbf{x}_0)$ and a constant $C > 0$, so that for any point $\mathbf{x}$ in the neighborhood of $\mathbf{x}_0$ one has [72,73,106–108]

$$|f(\mathbf{x}) - P_n(\mathbf{x} - \mathbf{x}_0)| \leq C|\mathbf{x} - \mathbf{x}_0|^{h(\mathbf{x}_0)} \tag{10}$$

If f is n times continuously differentiable at the point $\mathbf{x}_0$, then one can use for the polynomial $P_n(\mathbf{x} - \mathbf{x}_0)$ the order-n Taylor series of f at $\mathbf{x}_0$ and thus prove that $h(\mathbf{x}_0) > n$. Thus $h(\mathbf{x}_0)$ measures how irregular the function f is at the point $\mathbf{x}_0$. The higher the exponent $h(\mathbf{x}_0)$, the more regular the function f. In this work, we will mainly consider fractal functions of two variables that possess only cusp-like singularities. (We refer the reader to Ref. [124], for rigorous mathematical results concerning 2D oscillating singularities or chirps.) But the situation is a little more tricky than in 1D. Indeed one has to distinguish two main cases depending on whether scale invariance is under isotropic or anisotropic dilations [1,2,36,108,121–123,125].

1. *Isotropic Dilations*

Local scale invariance under isotropic dilations means that locally, around the point $\mathbf{x}_0$, the function f behaves as

$$f(\mathbf{x}_0 + \lambda\mathbf{u}) - f(\mathbf{x}_0) \simeq 1\lambda^{h(\mathbf{x}_0)}[f(\mathbf{x}_0 + \mathbf{u}) - f(\mathbf{x}_0)] \tag{11}$$

where $\lambda > 0$ and $\mathbf{u}$ is a unit vector. If the scaling exponent $h(\mathbf{x}_0)$ does not depend upon the direction of $\mathbf{u}$, then f displays isotropic local scale invariance around $\mathbf{x}_0$ and the corresponding singularity is of Hölder exponent $h(\mathbf{x}_0)$. If, on the contrary, the scaling exponent depends upon the direction of $\mathbf{u}$, then the Hölder exponent is the minimum value of h over all the possible orientations of $\mathbf{u}$. Thus f displays anisotropic scale invariance around $\mathbf{x}_0$ with one, several, or a continuum of privileged directions along which the variation of f defines the Hölder exponent of the singularity located at $\mathbf{x}_0$.

2. *Anisotropic Dilations*

Local scale invariance under anisotropic dilations means that locally around the point $\mathbf{x}_0$, the function f behaves as [120–123,125]

$$f[\mathbf{x}_0 + \Lambda_\alpha(\lambda)r_\theta\mathbf{u}] - f(\mathbf{x}_0) \simeq 1\lambda^{h(\mathbf{x}_0)}[f(\mathbf{x}_0 + \mathbf{u}) - f(\mathbf{x}_0)] \tag{12}$$

where $\lambda > 0$ and $\mathbf{u}$ is a unit vector. r_θ is a rotation matrix and $\Lambda_\alpha(\lambda)$ is a positive diagonal 2×2 matrix that accounts for anisotropic self-affine scale transformation in the θ-rotated referential with origin $\mathbf{x}_0$:

$$\Lambda_\alpha(\lambda) = \begin{pmatrix} \lambda & 0 \\ 0 & \lambda^\alpha \end{pmatrix} \tag{13}$$

The function f thus displays anisotropic scale invariance around $\mathbf{x}_0$ and the Hölder exponent is given by the behavior of f in the direction $\theta(\alpha < 1)$ or $\theta + \pi/2(\alpha > 1)$.

Very much like the wavelet transform analysis of cusp singularities in 1D [47–49,74], in order to recover the Hölder exponent $h(\mathbf{x}_0)$ of a function f from $\mathbb{R}^2$ to $\mathbb{R}$, one needs to study the behavior of the wavelet transform modulus inside a cone $|\mathbf{x} - \mathbf{x}_0| < Ca$ in the (space-scale) half space [106,108,126]. As originally proposed by Mallat and collaborators [72,73], a very efficient way to perform point-wise regularity analysis is to use the wavelet transform modulus maxima. In the spirit of Canny edge detection [114], at a given scale a, the WTMM are defined as the points $\mathbf{b}$ where the wavelet transform modulus $\mathcal{M}_\psi[f](\mathbf{b}, a)$ [Eq. (7)] is locally maximum along the gradient direction given by the wavelet transform argument $\mathcal{A}_\psi[f](\mathbf{b}, a)$ [Eq. (8)]. These modulus maxima are inflection points of $f * \phi_a(\mathbf{x})$. As illustrated in the examples just below, these WTMM lie on connected chains hereafter called *maxima chains* [106–108]. In theory, one only needs to record the position of the local maxima of $\mathcal{M}_\psi$ along the maxima chains together with the value of $\mathcal{M}_\psi[f]$ and $\mathcal{A}_\psi[f]$ at the corresponding locations. At each scale a, our wavelet analysis thus reduces to store those WTMM maxima (WTMMM) only. They indicate locally the direction where the signal has the sharpest variation. This orientation component is the main difference between 1D and 2D wavelet transform analysis. These WTMMM are disposed along connected curves across scales called *maxima lines* [107,108]. We will define the WT skeleton as the set of maxima lines that converges to the (x, y)-plane in the limit $a \to 0^+$. This WT skeleton is likely to contain all the information concerning the local Hölder regularity properties of the function f under consideration [108].

Example 1. Isotropic singularity interacting with a localized smooth structure. Let us first illustrate the above definitions on the function f_1 shown in Figure 2:

$$f_1(\mathrm{x}) = Ae^{-(\mathrm{x}-\mathrm{x}_1)^2/2\sigma^2} + B|\mathrm{x} - \mathrm{x}_0|^{0.3} \tag{14}$$

This function is C^∞ everywhere except at $\mathbf{x} = \mathbf{x}_0$ where f_1 is isotropically singular with a Hölder exponent $h(\mathbf{x}_0) = 0.3$. Its 2D wavelet transform [Eq. (4)] with a first-order analyzing wavelet [the smoothing function $\phi(\mathbf{x})$ is

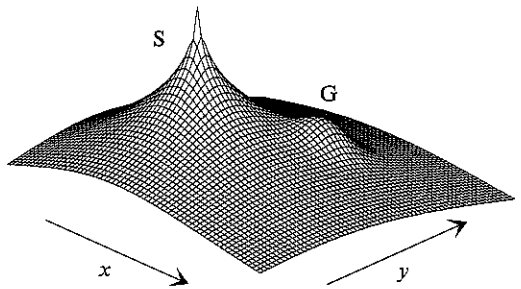

FIGURE 2. Three-dimensional representation of the function $f_1(\mathbf{x}) = Ae^{-(\mathbf{x}-\mathbf{x}_1)2/2\sigma 2} + B|\mathbf{x}-\mathbf{x}_0|^{0.3}$. The isotropic singularity S is located at $\mathbf{x}_0 = (-256, -256)$. The Gaussian localized structure G of width $\sigma = 128$ is located at $\mathbf{x}_1 = (256, 256)$. The parameter values are $A = 1$ and $B = -1$.

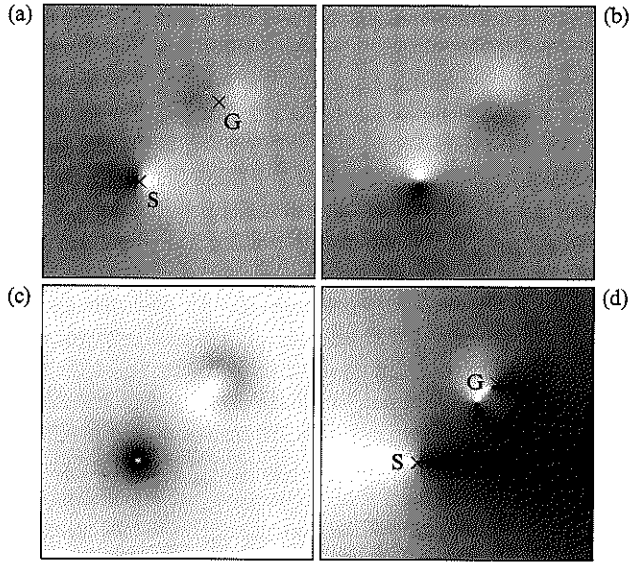

FIGURE 3. Wavelet transform [Eq. (4)] of the function f_1 shown in Figure 2, with a first-order analyzing wavelet (ϕ is the isotropic Gaussian function). (a) $T_{\psi_1}[f_1]$; (b) $T_{\psi_2}[f_1]$ coded using 32 gray levels from white (min T_ψ) to black (max T_ψ). (c) $\mathcal{M}_\psi[f_1]$ coded from white ($\mathcal{M}_\psi = 0$) to black (max $\mathcal{M}_\psi$). (d) $|\mathcal{A}_\psi[f_1]|$ coded from white ($|\mathcal{A}_\psi| = 0$) to black ($|\mathcal{A}_\psi| = \pi$). The considered scale is $a = 2^3\sigma_W$ where $\sigma_W = 13$ (pixels) is the characteristic size of ψ at the smallest resolved scale.

the isotropic Gaussian function] is shown in Figure 3 for a given scale $a = 2^3\sigma_w$, where $\sigma_w = 13$ is the width (in pixel units) of the analyzing wavelet at the smallest scale where it is still well enough resolved. Indeed σ_w is the smallest scale (or the highest resolution) accessible to our wavelet transform microscope. $T_{\psi 1}[f_1]$ and $T_{\psi_2}[f_1]$ [Eq. (4)] are shown in Figure 3a and b, respectively. The corresponding modulus $\mathcal{M}_\psi[f_1]$ and argument $\mathcal{A}_\psi[f_1]$ are represented in Figure 3c and d. From a simple visual inspection of Figure 3c, one can convince oneself that the modulus is radially symmetric around $\mathbf{x}_0$ where is located the singularity S. This is confirmed in Figure 3d where $\mathcal{A}_\psi[f_1]$ rotates uniformly from 0 to 2π around $\mathbf{x}_0$. The WTMM as well as the WTMMM are shown in Figure 4 for various values of the scale parameter a ranging from $a = 2^{3.5}\sigma_W$ (Fig. 4a) to $2^{7.5}$ (Fig. 4f). At small scale, there exist mainly two maxima chains. One is a closed curve around $\mathbf{x}_0$ at which the

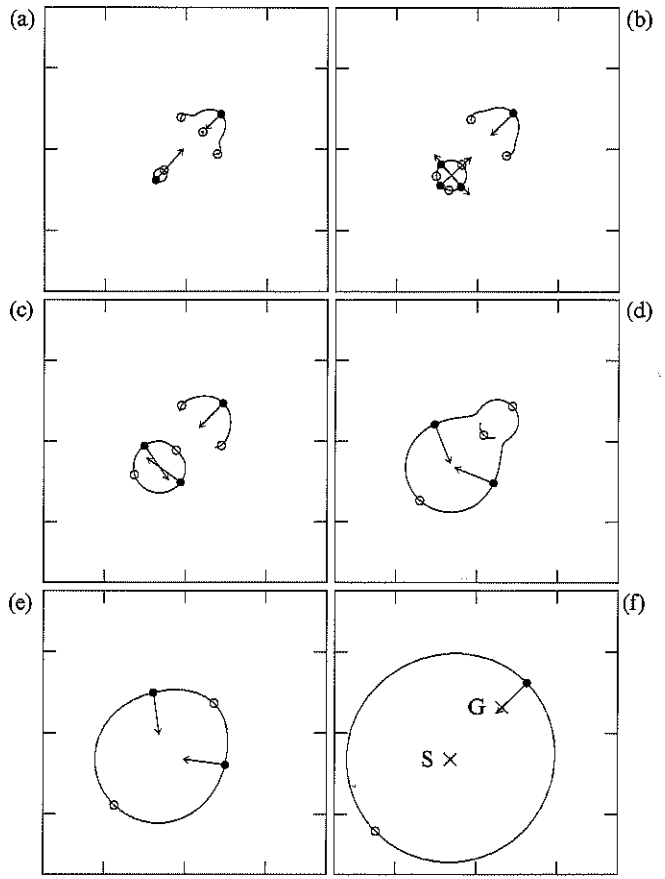

FIGURE 4. Maxima chains (solid line) defined by the WTMM of the function f_1 (Fig. 3). The local maxima (respectively minima) along these chains are indicated by (•) [respectively (○)] from which originates an arrow whose length is proportional to $\mathcal{M}_\psi[f_1]$ and its direction (with respect to the x-axis) is given by the WTMM argument $\mathcal{A}_\psi[f_1]$. The scale parameter is $a = 2^{3.5}$ (a), $2^{4.7}$ (b), $2^{5.5}$ (c), $2^{6.3}$ (d), $2^{6.8}$ (e), and $2^{7.5}$ (f) in σ_w units. Same first-order analyzing wavelet as in Figure 3.

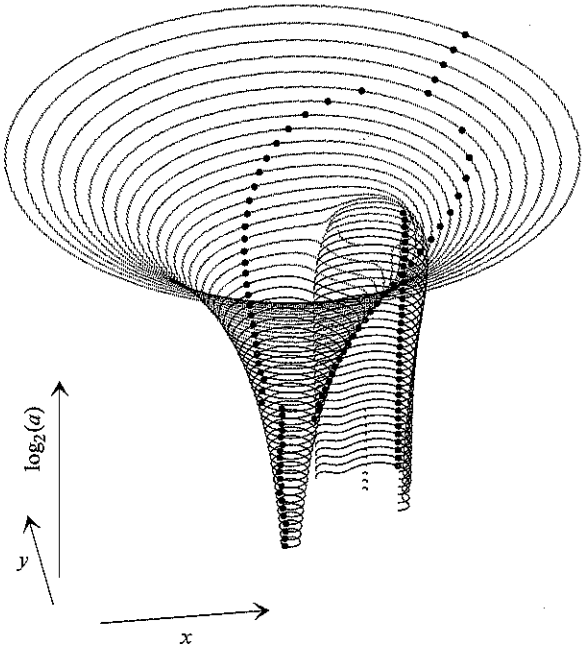

FIGURE 5. Three-dimensional representation of the topological evolution of the WTMM chains of f_1 in the space-scale half-hyperplane. The WTMMM (•) are disposed on connected curves called maxima lines. These maxima lines are obtained by linking each WTMMM computed at a given scale to the nearest WTMMM computed at the scale just above. There exist two maxima lines, $\mathcal{L}_{\mathbf{x}_0}(a)$ and $\mathcal{L}_{\mathbf{x}_1}(a)$, pointing, respectively,to the singularity S and to the smooth localized structure G in the limit $a \to 0^+$.

singularity S is located. The other one is an open curve that partially surrounds G. On each of these maxima chains, one finds only one WTMMM (•) whose corresponding arguments are such that the gradient vector points to S and G, respectively. As far as the singularity S is concerned, this means that the direction of largest variation of f_1 around S is given by $\theta_{\mathbf{x}_0} = \mathcal{A}_\psi[f_1] + \pi$, where $\mathcal{A}_\psi[f_1]$ is the argument of the corresponding WTMMM. When increasing the scale parameter, the maxima chains evolve; in particular the closed maxima chain around S swells (its characteristic size behaves like a) until it connects with the maxima chain associated with G (Fig. 4d) to form a single closed curve surrounding both S and G (Fig. 4f). The topological evolution of the maxima chains in the space-scale half-hyperplane is illustrated in Figure 5. This three-dimensional representation enlightens the existence of two maxima lines obtained by linking the WTMMM step by step (i.e., as continuously as possible) from small to large scales. One of these maxima

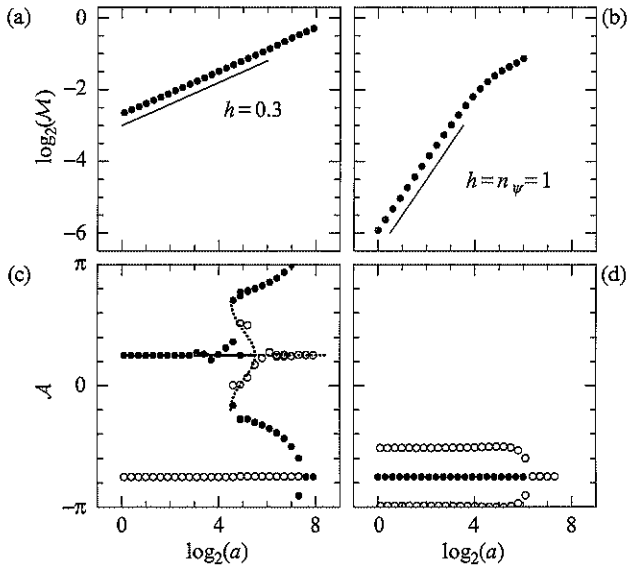

FIGURE 6. Evolution of $\mathcal{M}_\psi[f_1]$ and $\mathcal{A}_\psi[f_1]$ when following, from large scale to small scale, the maxima lines $\mathcal{L}_{\mathbf{x}_0}(a)$ and $\mathcal{L}_{\mathbf{x}_1}(a)$ pointing, respectively, to the singularity S [(a) and (c), respectively] and to the localized smooth structure G [(b) and (d), respectively]. The symbols (•) and (○) have the same meaning as in Figure 4. Same first-order analyzing wavelet as in Figure 3.

lines points to the singularity S in the limit $a \to 0^+$. As shown in Figure 6a, along this maxima line $[\mathcal{L}_{\mathbf{x}_0}(a)]$, the wavelet transform modulus behaves as [72,73]

$$\mathcal{M}_\psi[f_1][\mathcal{L}_{\mathbf{x}_0}(a)] \sim a^{h(\mathbf{x}_0)}, \qquad a \to 0^+ \tag{15}$$

where $h(\mathbf{x}_0) = 0.3$ is the Hölder exponent of S. Moreover, along this maxima line, the wavelet transform argument evolves toward the value (Fig. 6c):

$$\mathcal{A}_\psi[f_1](\mathcal{L}_{\mathbf{x}_0}(a)) = \pi + \theta_{\mathbf{x}_0} \tag{16}$$

in the limit $a \to 0^+$, where $\theta_{\mathbf{x}_0}$ is nothing but the direction of the largest variation of f_1 around $\mathbf{x}_0$, i.e., the direction to follow from $\mathbf{x}_0$ to cross the maxima line at a given (small) scale. From the maxima line $\mathcal{L}_{\mathbf{x}_0}(a)$, one thus gets the required amplitude as well as directional informations to characterize the local Hölder regularity of f_1 at $\mathbf{x}_0$. Note that along the other maxima line $\mathcal{L}_{\mathbf{x}_1}(a)$ that points to $\mathbf{x}_1$ where the smooth localized structure G is located, the wavelet transform modulus behaves as (Fig. 6b)

$$\mathcal{M}_\psi[f_1](\mathcal{L}_{\mathbf{x}_1}(a)) \sim a^{n_\psi}, \qquad a \to 0^+ \tag{17}$$

where $n_\psi = 1$ is the order of the analyzing wavelet.

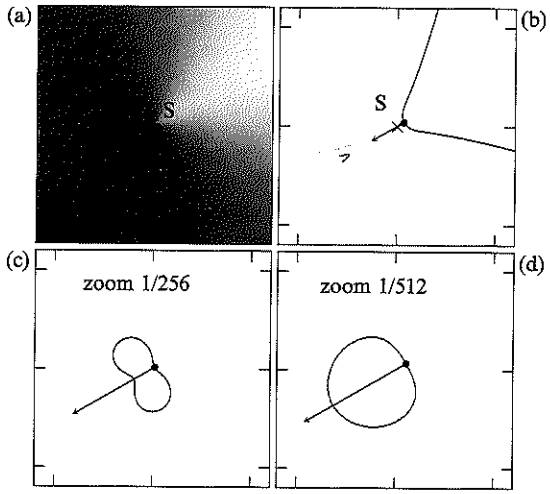

FIGURE 7. WTMM analysis of the function $f_2(\mathbf{x})$ defined in Eq. (18). (a) $f_2(\mathbf{x})$ as coded using 32 gray levels from white (min f_2) to black (max f_2). The maxima chains (solid line) and the WTMMM (•) are shown for the following values of the scale parameter $a = 2$ (b), 2^8 (c), and 2^{11} (d) in σ_w units. Same first-order analyzing wavelet as in Figure 3.

Example 2. Anisotropic singularity. Let us illustrate with a specific example, the possibility for a function $f_2(\mathbf{x})$ to display anisotropic local scale invariance with respect to isotropic dilations. In Figure 7a the following function is represented:

$$f_2(\mathbf{x}) = f_2(\rho, \theta) = -\rho^{h(\theta)} \tag{18}$$

with

$$h(\theta) = 0.3 \sin(\theta - 2\pi/3) + 0.5 \tag{19}$$

The exponent $h(\theta)$ is nothing but the Hölder exponent at $\rho = 0$ of the 1D profile obtained when intersecting the image in Figure 7a along the direction θ. As far as the whole 2D problem is concerned, the Hölder exponent of the singularity S is $h(\mathbf{x}_0) = \min_\theta h(\theta) = 0.2$. It quantifies the sharpest variation of $f_2(\mathbf{x})$, which occurs in the direction $\theta_{\mathbf{x}_0} = \pi/6$. As shown in Figure 7b–d for different zooms, there exists at each scale only one WTMMM, which belongs to a unique maxima line $\mathcal{L}_{\mathbf{x}_0}(a)$ pointing to the singularity S. Note that this WTMMM is located in the direction $\theta_{\mathbf{x}_0} = \pi/6$ from the origin. When following $\mathcal{L}_{\mathbf{x}_0}(a)$ from large to small scales, $\mathcal{M}_\psi[f_2][\mathcal{L}_{\mathbf{x}_0}(a)]$ behaves as a power law with an exponent $h(\mathbf{x}_0) = 0.2$ (Fig. 8a), in remarkable agreement with the theoretical prediction for the Hölder exponent of S. Moreover, when investigating $\mathcal{A}_\psi[f_2][\mathcal{L}_{\mathbf{x}_0}(a)]$, one further gets directional

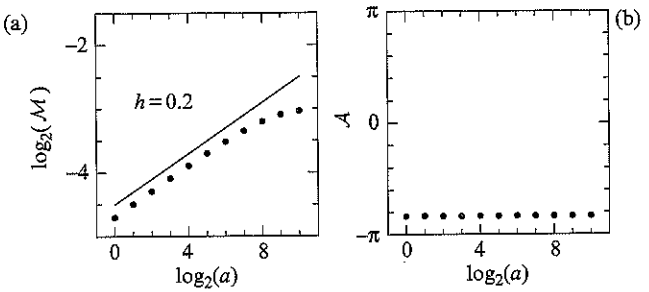

FIGURE 8. Evolution of (a) $\mathcal{M}_\psi[f_2]$ and (b) $\mathcal{A}_\psi[f_2]$ when following, from large to small scales, the maxima line $\mathcal{L}_{\mathbf{x}_0}(a)$ (•), which points to the singularity S. Same first-order analyzing wavelet as in Figure 7.

information: $\mathcal{A}_\psi[f_2] = -5\pi/6 = \theta_{\mathbf{x}_0} - \pi$, from which one learns about the possible existence of some preferential direction as far as the Hölder regularity properties are concerned.

We will not treat here the case of local scale invariance with respect to anisotropic self-affine dilations. We send the reader to Arneodo *et al.* [108] where the 2D WTMM method has been be applied to random self-affine rough surfaces.

C. The 2D Wavelet Transform Modulus Maxima (WTMM) Method

Before describing the methodology to be used to perform a multifractal analysis of rough surfaces, we need to define the notion of singularity spectrum of a fractal function from $\mathbb{R}^2$ into $\mathbb{R}$ [108].

1. *Definition*

Let f be a function from $\mathbb{R}^2$ into $\mathbb{R}$ and S_h the set of all the points $\mathbf{x}_0$ so that the Hölder exponent [Eq. (10)] of f at $\mathbf{x}_0$ is h. The singularity spectrum $D(h)$ of f is the function that associates with any h, the Hausdorff dimension of S_h:

$$D(h) = d_H\{\mathbf{x} \in \mathbb{R}^2,\ h(\mathbf{x}) = h\} \tag{20}$$

In the previous section, we have seen that the maxima lines defined from the WTMMM computed at different scales can be used as a scanner of singularities. They allow us to detect the positions where the singularities are located as well as to estimate their strength h. A rather naive way to compute the $D(h)$ singularity spectrum would thus consist in identifying the

set of maxima lines along which the wavelet transform modulus behaves with a power-law exponent h [Eq. (15)] and then to use classical box-counting techniques [19–27] to compute the fractal dimension $D(h)$ of the set of points $\{\mathbf{x}_n\} \subset \mathbb{R}^2$ to which these maxima lines converge. Unfortunately, when investigating deterministic as well as random fractal functions, the situation is somewhat more intricate than when dealing with isolated singularities. The characteristic feature of these singular functions is the existence of a hierarchical distribution of singularities [47–50,62–65]. Locally, the Hölder exponent $h(\mathbf{x}_0)$ is then governed by the singularities that accumulate at $\mathbf{x}_0$. This results in unavoidable oscillations around the expected power-law behavior of the wavelet transform modulus [47–50,79]. The exact determination of h from log–log plots on a finite range of scales is therefore somewhat uncertain [127,128]. Note that there have been many attempts to circumvent these difficulties in 1D [79,129]. But in 2D (rough surfaces) as well as in 1D (multiaffine profiles), there exist fundamental limitations (which are not intrinsic to the wavelet technique) to the local measurement of the Hölder exponents of a fractal function. Therefore, the determination of statistical quantities like the $D(h)$ singularity spectrum requires a method that is more feasible and more appropriate than a systematic investigation of the wavelet transform local scaling behavior as experienced [127,128].

2. *Methodology*

Our strategy will consist in mapping the methodology developed [47–50] for multifractal analysis of irregular 1D landscapes to the statistical characterization of roughness fluctuations of 2D surfaces [107,108]. The 2D WTMM method relies upon the space-scale partitioning given by the wavelet transform skeleton. As discussed in Section II.B, this skeleton (see Fig. 12) is defined by the set of maxima lines that points to the singularities of the considered function and therefore is likely to contain all the information concerning the fluctuations of point-wise Hölder regularity. Let us define $\mathcal{L}(a)$ as the set of all maxima lines that exist at the scale a and that contain maxima at any scale $a' \leq a$. The important feature is that each time the analyzed image has a Hölder exponent $h(\mathbf{x}_0) < n_\psi$, there is at least one maxima line pointing toward $\mathbf{x}_0$ along which Eq. (15) is expected to hold. In the case of fractal functions, we thus expect that the number of maxima lines will diverge in the limit $a \to 0^+$, as the signature of the hierarchical organization of the singularities. The WTMM method consists in defining the following partitions functions directly from the WTMMM that belong to the wavelet transform skeleton:

$$\mathcal{Z}(q,a) = \sum_{\mathcal{L} \in \mathcal{L}(a)} \left[\sup_{(\mathbf{x},a') \in \mathcal{L},\, a' \leq a} \mathcal{M}_\psi[f](\mathbf{x},a') \right]^q \tag{21}$$

where $q \in \mathbb{R}$. As compared to classic box-counting techniques [19–27], the analyzing wavelet ψ plays the role of a generalized "oscillating box", the scale a defines its size, while the WTMM skeleton indicates how to position our oscillating boxes to obtain a partition (of $S = \cup S_h$) at the considered scale. Without the "sup" in Eq. (21), one would have implicitely considered a uniform covering with wavelets of the same size a. As emphasized [47–50,74], the "SUP" can be regarded as a way of defining a "Hausdorff-like" scale-adaptative partition that will prevent divergencies to show up in the calculation of $\mathcal{Z}(q,a)$ for $q < 0$.

Now, from the analogy that links the multifractal formalism to thermodynamics [48,49,67–69,76,77], one can define the exponent $\tau(q)$ from the power-law behavior of the partition function:

$$\mathcal{Z}(q,a) \sim a^{\tau(q)}, \qquad a \to 0^+ \tag{22}$$

where q and $\tau(q)$ play, respectively, the role of the inverse temperature and the free energy. The main result of the wavelet-based multifractal formalism is that in place of the energy and the entropy (i.e., the variables conjugated to q and τ), one has the Hölder exponent h [Eq. (10)] and the singularity spectrum $D(h)$ [Eq. (20)]. This means that the $D(h)$ singularity spectrum of f can be determined from the Legendre transform of the partition function scaling exponent $\tau(q)$:

$$D(h) = \min_q [qh - \tau(q)] \tag{23}$$

From the properties of the Legendre transform, it is easy to convince oneself that *homogeneous* (monofractal) fractal functions that involve singularities of unique Hölder exponent $h = \partial\tau/\partial q$ are characterized by a $\tau(q)$ spectrum that is a *linear* function of q. On the contrary, a *nonlinear* $\tau(q)$ curve is the signature of nonhomogeneous functions that display *multifractal* properties, in the sense that the Hölder exponent $h(\mathbf{x})$ is a fluctuating quantity that depends upon the spatial position $\mathbf{x}$ (in other words the local roughness exponent is fluctuating from point to point).

3. *Remark*

The exponents $\tau(q)$ are much more than simply some intermediate quantities of a rather easy experimental access. For some specific values of q, they have well known meaning [48].

- $q = 0$: From Eqs. (21) and (22), one deduces that the exponent $\tau(0)$ accounts for the divergence of the number of maxima lines in the limit $a \to 0^+$. This number basically corresponds to the number of wavelets of size a required to cover the set S of singularities of f. In full analogy with standard box-counting arguments [19–27], $-\tau(0)$ can be identified to the fractal dimension (capacity) of this set:

$$-\tau(0) = d_F\{\mathbf{x}, h(\mathbf{x}) < +\infty\} \tag{24}$$

- $q = 1$: As pointed out [48], the value of the exponent $\tau(1)$ is related to the fractal dimension (capacity) of the rough surface $\mathcal{S}$ defined by the function f. More precisely [130]:

$$d_F(\mathcal{S}) = \max[2, 1 - \tau(1)] \tag{25}$$

- $q = 2$: It is easy to show that the exponent $\tau(2)$ is intimately related to the scaling exponent β of the spectral density:

$$S(k) = \frac{1}{2\pi}\int d\theta \mid \hat{f}(k,\theta)|^2 \sim k^{-\beta} \tag{26}$$

where

$$\beta = 4 + \tau(2) \tag{27}$$

From a practical point of view, the computation of the $D(h)$ singularity spectrum, via the Legendre transform defined in Eq. (23), first requires a smoothing of the $\tau(q)$ curve. This procedure has a main disadvantage. This smoothing operation prevents the observation of any nonanalycity in the curves $\tau(q)$ and $D(h)$ and the interesting physics of *phase transitions* [49,71,131,132] in the scaling properties of fractal functions can be completely missed. As suggested [49,131,133–137], one can avoid directly performing the Legendre transform by considering the quantities h and $D(h)$ as mean quantities defined in a canonical ensemble, i.e., with respect to their Boltzmann weights computed from the WTMMM [49,79]:

$$W_\psi[f](q, \mathcal{L}, a) = \frac{|\sup_{(\mathbf{x},a')\in\mathcal{L},\, a'\le a} \mathcal{M}_\psi[f](\mathbf{x}, a')|^q}{\mathcal{Z}(q,a)} \tag{28}$$

where $\mathcal{Z}(q,a)$ is the partition function defined in Eq. (21). Then one computes the expectation values:

$$h(q,a) = \sum_{\mathcal{L}\in\mathcal{L}(a)} \ln\left|\sup_{(\mathbf{x},a')\in\mathcal{L},\, a'\le a} \mathcal{M}_\psi[f](\mathbf{x},a')\right| W_\psi[f](q,\mathcal{L},a) \tag{29}$$

and

$$D(q,a) = \sum_{\mathcal{L}\in\mathcal{L}(a)} W_\psi[f](q,\mathcal{L},a)\ln\left[W_\psi[f](q,\mathcal{L},a)\right] \tag{30}$$

from which one extracts

$$h(q) = \lim_{a\to 0+} h(q,a)/\ln a \tag{31}$$

$$D(q) = \lim_{a\to 0+} D(q,a)/\ln a \tag{32}$$

and therefore the $D(h)$ singularity spectrum.

4. *Numerical Implementation*

In this section, we briefly review the main steps of the numerical implementation of the 2D WTMM method. Let us consider an $n \times n$ digitized image of a rough surface.

- *Step 1*: Computation of the 2D wavelet transform. We compute the two components T_{ψ_1} and T_{ψ_2} of the wavelet transform [Eq. (4)] in the Fourier domain, using 2D Fast Fourier Transform (FFT) [138] and inverse FFT. We start our analysis by choosing the analyzing wavelet among the class of radially isotropic wavelets defined in Section II.A (Fig. 1). To master edge effects we focus only on the $n/2 \times n/2$ central part of the image where our wavelet coefficients can be shown to be not affected by the boundary of the original image. This means that we will be careful not to increase the scale parameter a above a critical value $a_{\max}$ so that the $n/2 \times n/2$ central wavelet coefficients remain safe of finite-size effects. In the opposite limit, we will define a lower bound $a_{\min}$ to the accessible range of scales so that the analyzing wavelet is still well resolved at that scale. (We refer the reader to Section 1.3.3 of Decoster's Ph.D. thesis [139] for a detailed practical definition of the accessible $[a_{\min}, a_{\max}]$ range of scales.) Under those precautions, one can be confident of our wavelet transform microscope as far as the investigation of the scale invariance properties in the range $a \in [a_{\min}, a_{\max}]$ is concerned.
- *Step 2*: Computation of the wavelet transform skeleton. As explained in Section II.B, at a given scale a, we identify the wavelet transform modulus maxima as the points where $\mathcal{M}_\psi[f](\mathbf{b}, a)$ [Eq. (7)] is locally maximum along the gradient direction given by $\mathcal{A}_\psi[f](\mathbf{b}, a)$ [Eq. (8)]. Then we chain the points that are nearest neighbors (which actually have compatible arguments). Along each of these maxima chains, we locate the local maxima previously called WTMMM. Note that the two ends of an open maxima chain are not allowed positions for the WTMMM. Once

computed the set of WTMMM for a finite number of scales ranging from $a_{\min}$ to $a_{\max}$, one proceeds to the connection of these WTMMM from scale to scale. One starts at the smallest scale $a_{\min}$ and we link each WTMMM to their nearest neighbor found at the next scale just above. We proceed iteratively from scale to scale up to $a_{\max}$. All the WTMMM that then remain isolated are suppressed. All the WTMMM that are connected on a curve across scales that does not originate from the smallest scale $a_{\min}$ are also suppressed. We then store the modulus $\mathcal{M}_\psi$ and the argument $\mathcal{A}_\psi$ of the WTMMM that belong to the so-called maxima lines. Those lines are supposed to converge, in the limit $a \to 0^+$, to the points where the singularities of the image under study are located. As explained in Section II.B, to define the wavelet transform skeleton, one has to select these maxima lines that satisfy Eq. (15) from those that satisfy Eq. (17) and that are wavelet dependent. This is done by increasing the order of the analyzing wavelet; for n_ψ large enough, the spurious maxima lines are suppressed by a simple thresholding on $\mathcal{M}_\psi$ at the smallest scale $a_{\min}$. Their roots are definitely rejected as misleading singularity locations.

- *Step 3*: Computation of the multifractal spectrum. According to Eq. (21), one uses the wavelet transform skeleton to compute the partition function $\mathcal{Z}(q,a)$ on the discrete set of considered scales $a_{\min} \leq a \leq a_{\max}$. Then, for a given value of $q \in [q_{\min}, q_{\max}]$, one extracts the exponent $\tau(q)$ [Eq. (22)] from a linear regression fit of $\ln \mathcal{Z}(q,a)$ vs. $\ln a$. As a test of the robustness of our measurement, we examine the stability of our estimate of $\tau(q)$ with respect to the range of scales $[a^*_{\min}, a^*_{\max}] \subset [a_{\min}, a_{\max}]$ over which the linear regression fit is performed. After estimating the exponent $\tau(q)$ for a discrete set of q-values, we smooth the $\tau(q)$ curve using standard procedure. Then, one determines the $D(h)$ singularity spectrum by Legendre transforming the $\tau(q)$ curve according to Eq. (23). As a check of the reliability of our results, we use the alternative strategy defined in Eq. (28) to (32) to estimate the $D(h)$ singularity spectrum without performing explicitly the Legendre transform. When dealing specifically with stochastic process, we generally have several images at our disposal somehow corresponding to different realizations of this process. In this case, we will mainly proceed to two different averagings corresponding to the following:

  - *Quenched averaging*: We extract the $\tau(q)$ curve from averaging $< \ln \mathcal{Z}(q,a) >$ over the number of images:

$$e^{<\ln \mathcal{Z}(q,a)>} \sim a^{\tau(q)}, \qquad a \to 0^+ \tag{33}$$

In other words, the $\tau(q)$ spectrum is obtained by averaging over the $\tau(q)$ curves extracted from each individual image.

  - *Annealed averaging*: One can alternatively compute the $\tau(q)$ spectrum after averaging the partition functions obtained for each image:

$$< \mathcal{Z}(q,a) > \sim a^{\tau(q)}, \qquad a \to 0^+ \tag{34}$$

Note that in most of the examples discussed in this work, we have not observed any significant discrepency between the $\tau(q)$ spectra obtained using either one of these averagings. Consequently, in the following we will mainly show the results obtained when estimating the $\tau(q)$ and $D(h)$ multifractal spectra using annealed averaging.

- *Step 4*: Computation of the WTMMM probability density functions. From the computation of the joint probability density function $P_a(\mathcal{M}, \mathcal{A})$, we first proceed to a test of the possible independence of $\mathcal{M}$ and $\mathcal{A}$. If it is so, we then investigate separately the scale dependence of $P_a(\mathcal{M})$ and $P_a(\mathcal{A})$. From the investigation of the shape of $P_a(\mathcal{A})$, and of its possible evolution when varying a, one can then quantify some possible departure from isotropic scaling as well as the existence of possible privileged directions. When $P_a(\mathcal{M}, \mathcal{A})$ does not factorize, then $\mathcal{M}$ and $\mathcal{A}$ are intimately related. In this case, one can try to compute the $\tau_{\mathcal{A}}(q)$ and $D_{\mathcal{A}}(h)$ multifractal spectra by conditioning the statistics of the modulus fluctuations to a given value of the argument. The $\mathcal{A}$-dependence of these spectra quantifies what one could call anisotropic multifractal scaling properties.

III. Test Applications of the WTMM Method to Monofractal and Multifractal Rough Surfaces

A. Fractional Brownian Surfaces

Since its introduction by Mandelbrot and Van Ness [140], the fractional Brownian motion (fBm) has become a very popular model in signal and image processing [1–18,28–30]. In one dimension, fBm has proved useful for modeling various physical phenomena with long-range dependence, e.g., "$1/f$" noises. The fBm exhibits a power spectral density $S(\omega) \sim 1/\omega^\beta$, where the spectral exponent $\beta = 2H + 1$ is related to the Hurst exponent H. 1D fBm has been extensively used as test stochastic signals for Hurst exponent measurements. The performances of classic methods [33–36,39–42,141–143] (e.g., height–height correlation function, variance and power spectral methods, first return and multireturn probability distributions, maximum likelihood techniques) have been recently competed by wavelet-based

techniques [144–157]. Comparative analysis of different wavelet-based estimators for the self-similarity parameter H of fBm can be found [152–154].

FBm's are homogeneous random self-affine functions that have been specifically used to calibrate the 1D WTMM methodology [47–49,79]. This method was shown to be a very efficient tool to diagnose the monofractal scaling properties of fBm. Moreover, it provides very accurate new estimators of the Hurst exponent with remarkable performances [158]. The purpose of this section is to carry out a test application of the 2D WTMM methodology described in Section II, on several realizations of 2D fBm [108].

The generalization of Brownian motion to more than one dimension was first considered by Levy [159]. The generalization of fBm follows along similar lines. A 2D fBm $B_H(\mathbf{x})$ indexed by $H \in [0,1]$ is a process with stationary zero-mean Gaussian increments and whose correlation function is given by [1,2,28,159,160]

$$< B_H(\mathbf{x})B_H(\mathbf{y}) > = \frac{\sigma^2}{2}(|\mathbf{x}|^{2H} + |\mathbf{y}|^{2H} - |\mathbf{x}-\mathbf{y}|^{2H}) \tag{35}$$

where $< \cdots >$ represents the ensemble mean value. The variance of such a process is

$$\mathrm{var}(B_H(\mathbf{x})) = \sigma^2|\mathbf{x}|^{2H} \tag{36}$$

from which one recovers the classic behavior $\mathrm{var}[B_{1/2}(\mathbf{x})] = \sigma^2|\mathbf{x}|$ for uncorrelated Brownian motion with $H = 1/2$. 2D fBms are self-affine processes that are statistically invariant under isotropic dilations [Eq. (11)]:

$$B_H(\mathbf{x}_0 + \lambda\mathbf{u}) - B_H(\mathbf{x}_0) \simeq \lambda^H[B_H(\mathbf{x}_0 + \mathbf{u}) - B_H(\mathbf{x}_0)] \tag{37}$$

where $\mathbf{u}$ is a unitary vector and $\simeq$ stands for the equality in law. The index H corresponds to the Hurst exponent; the higher the exponent H, the more regular the fBm surface. But since Eq. (37) holds for any $\mathbf{x}_0$ and any direction $\mathbf{u}$, this means that almost all realizations of the fBm process are continuous, everywhere nondifferentiable, isotropically scale-invariant as characterized by a unique Hölder exponent $h(\mathbf{x}) = H, \forall\mathbf{x}$ [1,2,28,158]. Thus fBm surfaces are the representation of homogeneous stochastic fractal functions characterized by a singularity spectrum that reduces to a single point

$$\begin{aligned} D(h) &= 2 \qquad \text{if } h = H \\ &= -\infty \qquad \text{if } h \neq H \end{aligned} \tag{38}$$

By Legendre transforming $D(h)$ according to Eq. (23), one gets the following expression for the partition function exponent [Eq. (22)]:

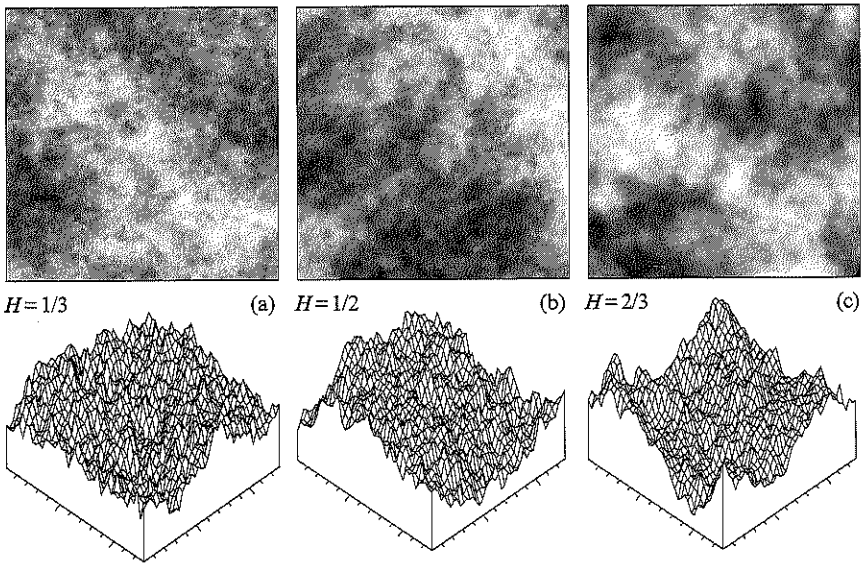

FIGURE 9. FBm surfaces (128×128) generated with the Fourier transform filtering synthesis method. (a) $H = 1/3$; (b) $H = 1/2$; (c) $H = 2/3$. In the top panels, $B_H(\mathbf{x})$ is coded using 32 gray levels from white (min B_H) to black (max B_H).

$$\tau(q) = qH - 2 \tag{39}$$

$\tau(q)$ is a linear function of q, the signature of monofractal scaling, with a slope given by the index H of the fBm.

We have tested the 2D WTMM method described in Section II on fBm surfaces generated by the so-called Fourier transform filtering method [28,29,160]. We have used this particular synthesis method because of its implementation simplicity. Indeed it amounts to a fractional integration of a 2D "white noise" and therefore it is expected to reproduce quite faithfully the expected isotropic scaling invariance properties [Eqs. (37)–(39)]. From a visual inspection of Figure 9a ($H = 1/3$), 9b ($H = 1/2$), and 9c ($H = 2/3$), one can convince oneself that the fBm surfaces become less and less irregular when increasing the index H. This is nothing but the traduction that the fractal dimension of fBm surfaces increases from 2 to 3 when H covers [0,1] [Eq. (25)]:

$$d_F(\mathrm{f}\,Bm\mathcal{S}) = 1 - \tau(1) = 3 - H \tag{40}$$

When increasing H, a fBm surface becomes more and more similar to a smooth Euclidean 2D surface.

In Figure 10 are reported the results of a power-spectral analysis of a (1024×1024) image of a fBm rough surface with Hurst exponent $H = 1/3$.

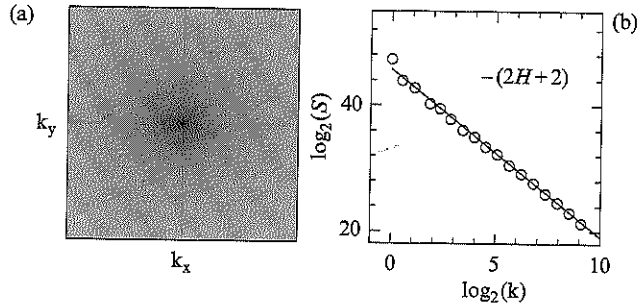

FIGURE 10. Power spectrum analysis of a (1024 × 1024) image of a fBm surface $B_{1/3}(\mathbf{x})$. (a) in $|\hat{B}_{1/3}(\mathbf{k})|$ as coded using 32 gray levels from white (min $\ln|\hat{B}_{1/3}|$) to black (max $\ln|\hat{B}_{1/3}|$). (b) The spectral density $S(|\mathbf{k}|)$ vs. $|\mathbf{k}|$ in a logarithmic representation. The solid line corresponds to the theoretical power-law prediction with exponent $\beta = 2H + 2 = 8/3$ [Eq. (41)].

In Figure 10a, the Fourier transform of $B_{1/3}(\mathbf{x})$ does not display any significant departure from radial symmetry. Isotropic scaling is actually confirmed when averaging $\hat{B}_{1/3}(\mathbf{k})$ over several of such images. In Figure 10b, the power spectral density is shown to behave as a power law as a function of the wavevector modulus $|\mathbf{k}|$, with an exponent that is in perfect agreement with the theoretical prediction for the spectral exponent [Eq. (27)]:

$$\beta = 4 + \tau(2) = 2 + 2H \tag{41}$$

Along the lines of the numerical implementation procedure described in Section II.C, we have wavelet transformed 32 (1024 × 1024) images of $B_{H=1/3}$ with an isotropic first-order analyzing wavelet. To master edge effects, we then restrain our analysis to the 512 × 512 central part of the wavelet transform of each image. In Figure 11 the computation of the maxima chains and the WTMMM for an individual image at three different scales is illustrated. In Figure 11b the convolution of the original image (Fig. 11a) with the isotropic Gaussian smoothing filter ϕ [Eq. (5)] is shown. According to the definition of the wavelet transform modulus maxima, the maxima chains correspond to well-defined edge curves of the smoothed image. The local maxima of $\mathcal{M}_\psi$ along these curves are located at the points where the sharpest intensity variation is observed. The corresponding arrows clearly indicate that locally, the gradient vector points in the direction (as given by $\mathcal{A}_\psi$) of maximum change of the intensity surface. When going from large scale (Fig. 11d) to small scale (Fig. 11c), the characteristic average distance between two nearest neighbor WTMMM decreases like a. This means that the number of WTMMM and, in turn, the number of maxima lines proliferate across scales like a^{-2}. The corresponding wavelet transform skeleton is shown in Figure 12. As confirmed just

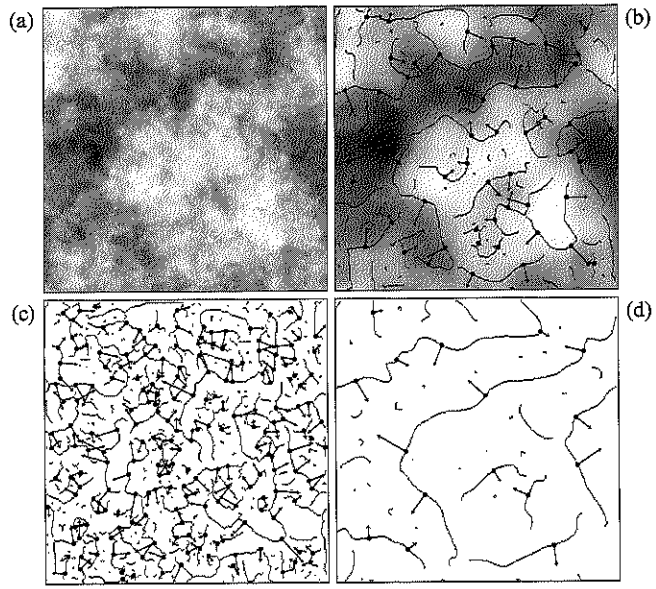

FIGURE 11. 2D wavelet transform analysis of $B_{H=1/3}(\mathbf{x})$. ψ is a first-order radially symmetric analyzing function (see Fig. 1). (a) Thirty-two gray-scale coding of the central 512 ×512 portion of the original image. In (b) $a = 2\sigma_W$, (c) $a = 2^{0.1}\sigma_W$, and (d) $a = 2^{1.9}\sigma_W$ are shown the maxima chains; the local maxima of $\mathcal{M}_\psi$ along these chains are indicated by (•) from which originate an arrow whose length is proportional to $\mathcal{M}_\psi$ and its direction (with respect to the x-axis) is given by $\mathcal{A}_\psi$. In (b), the smoothed image $\phi_{\mathbf{b},a} * B_{1/3}$ [Eq. (5)] is shown as a gray-scale coded background from white (min) to black (max).

below, when extrapolating the arborescent structure of this skeleton to the limit $a \to 0^+$, one recovers the theoretical result that the support of the singularities of a 2D f Bm has a dimension $d_F = 2$, i.e., $B_{H=1/3}(\mathbf{x})$ is nowhere differentiable [1,2,28,29,159].

The local scale invariance properties of a f Bm rough surface are investigated in Figure 13. When looking at the behavior of $\mathcal{M}_\psi$ along some maxima lines belonging to the wavelet transform skeleton, despite some superimposed fluctuations, one observes a rather convincing power-law decrease with an exponent $h(\mathbf{x}_0)$ that does not seem to depend upon the spatial location $\mathbf{x}_0$. Moreover, the theoretical value for the Hölder exponent $h(\mathbf{x}_0) = H = 1/3$ provides a rather good fit of the slopes obtained at small scale in a logarithmic representation of $\mathcal{M}_\psi$ vs. a [Eq. (15)]. When looking at the simultaneous evolution of $\mathcal{A}_\psi$ along the same maxima lines, one observes random fluctuations. Unfortunately, because of the rather limited range of scales accessible to our mathematical microscope, $a \in [\sigma_W, 2^4\sigma_W]$, there is no hope of demostrating numerically that $\mathcal{A}_\psi$ actually performs a random walk over $[0, 2\pi]$.

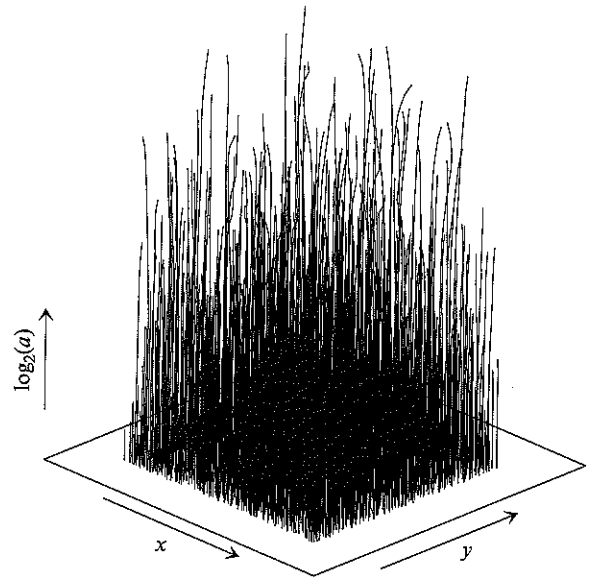

FIGURE 12. Wavelet transform skeleton of the 2D fBm image shown in Figure 11a. This skeleton is defined by the set of maxima lines obtained after linking the WTMMM detected at different scales. Same analyzing wavelet as in Figure 11.

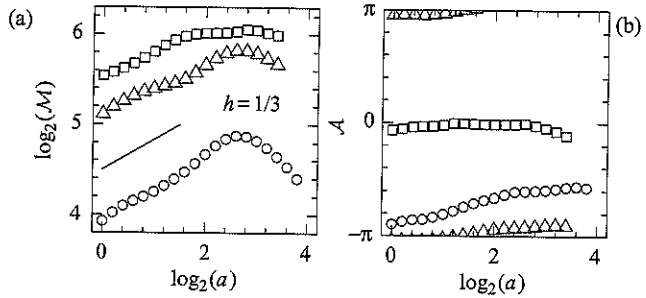

FIGURE 13. Characterizing the local Hölder regularity of $B_{H=1/3}(\mathbf{x})$ from the behavior of the WTMMM along the maxima lines. Three maxima lines are investigated. (a) $\log_2 \mathcal{M}_\psi$ vs. $\log_2 a$; (b) $\mathcal{A}_\psi$ vs. $\log_2 a$. Same analyzing wavelet as in Figure 11. The solid line in (a) corresponds to the theoretical slope $h = H = 1/3$. a is expressed in σ_W units.

In Figure 14 the results of the computation of the $\tau(q)$ and $D(h)$ spectra using the 2D WTMM method described in Section II are reported. As shown in Figure 14a, the annealed average partition function $\mathcal{Z}(q,a)$ [over 32 images of $B_{1/3}(\mathbf{x})$] displays a remarkable scaling behavior over more than three octaves when plotted versus a in a logarithmic representation

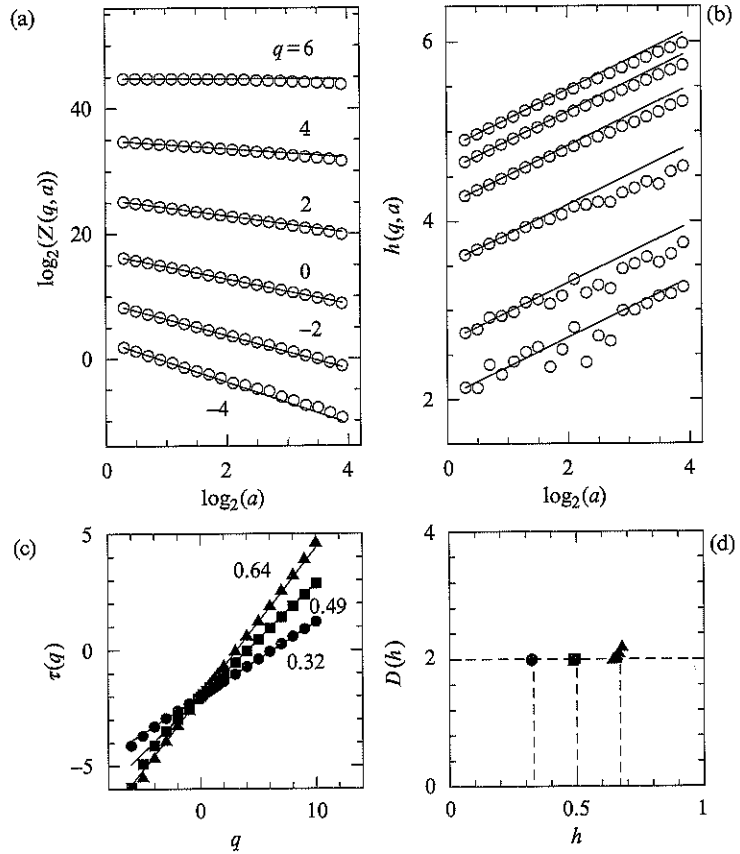

FIGURE 14. Determination of the $\tau(q)$ and $D(h)$ spectra of 2D fBm with the 2D WTMM method. (a) $\log_2 \mathcal{Z}(q,a)$ vs. $\log_2 a$; the solid lines correspond to the theoretical predictions $\tau(q) = qH - 2$ [Eq. (39)] with $H = 1/3$. (b) $h(q, a)$ vs. $\log_2 a$; the solid lines correspond to the theoretical slope $H = 1/3$. (c) $\tau(q)$ vs. q for $H = 1/3$(•), 1/2 (■), and 2/3 (▲); the solid lines correspond to linear regression fit estimates of H. (d) $D(h)$ vs. h as obtained from the scaling behavior of $D(q, a)$ vs. $\log_2 a$ [Eq. (30)]; the symbols have the same meaning as in (c). Same analyzing wavelet as in Figure 11. These results correspond to annealed averaging over 32 (1024 × 1024) fBm images. a is expressed in σ_W units.

[Eqs. (21) and (22)]. Moreover, for a wide range of values of $q \in [-4, 6]$, the data are in good agreement with the theoretical $\tau(q)$ spectrum [Eq. (39)]. When proceeding to a linear regression fit of the data over the first two octaves, one gets the $\tau(q)$ spectra shown in Figure 14c for three values of the fBm index $H = 1/3$, 1/2, and 2/3. Whatever H, the data systematically fall on a straight line, the signature of homogeneous (monofractal) scaling properties. However, the slope of this straight line provides a slight

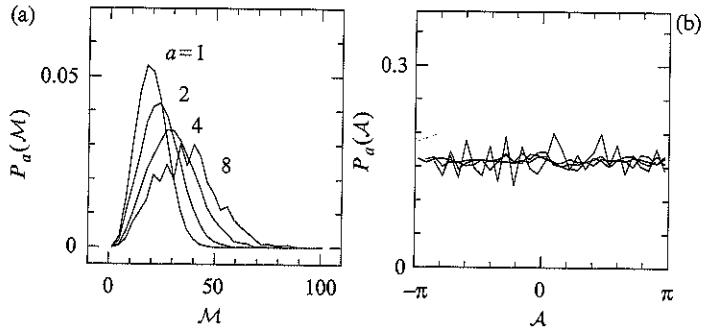

FIGURE 15. Pdfs of the WTMMM coefficients of $B_{1/3}(\mathbf{x})$ as computed at different scales $a = 1, 2, 4$, and 8 (in σ_W units). (a) $P_a(\mathcal{M})$ vs. $\mathcal{M}$. (b) $P_a(\mathcal{A})$ vs. $\mathcal{A}$. ψ is the first-order analyzing wavelet shown in Figure 1. These results correspond to averaging over 32 (1024×1024) fBm images.

underestimate of the corresponding Hurst exponent H. Let us point out that a few percent underestimate has also been reported when performing similar analysis of 1D fBm [47–49,98]. Theoretical investigation of finite-size effects and statistical convergence has been recently performed to explain this experimental observation [98].

In Figure 15 are shown the pdfs $P_a(\mathcal{M}) = \int d\mathcal{A} P_a(\mathcal{M}, \mathcal{A})$ and $P_a(\mathcal{A}) = \int d\mathcal{M} P_a(\mathcal{M}, \mathcal{A})$, computed for four different values of the scale parameter with $B_{1/3}(\mathbf{x})$. As seen in Figure 15a, $P_a(\mathcal{M})$ is not a Gaussian [in contrast to the pdf of the continuous 2D wavelet coefficients when using Eq. (7)], but decreases fast to zero at zero. This explains that when concentrating on the wavelet transform skeleton, the discrete sum on the r.h.s. of Eq. (21) no longer diverges when considering negative q values. This remark is at the heart of the 2D WTMM method; by allowing us to compute the $\tau(q)$ spectrum for negative as well as positive q values, the 2D WTMM method is a definite step beyond the 2D structure function method that is intrinsically restricted to positive q values. The corresponding pdfs $P_a(\mathcal{A})$ are represented in Figure 15b. $P_a(\mathcal{A})$ clearly does not evolve across scales. Moreover, except some small amplitude fluctuations observed at the largest scale, $P_a(\mathcal{A}) = 1/2\pi$ is a flat distribution as expected for statistically isotropic scale-invariant rough surfaces. The results reported in Figure 16 not only corroborate statistical isotropy but they bring unambiguous evidence for the independence of $\mathcal{M}$ and $\mathcal{A}$. For two different scales, the pdf of $\mathcal{M}$, when conditioned by the argument $\mathcal{A}$, is shown to be shape invariant. We refer the reader to Arneodo *et al.* [108] for a similar detailed discussion of the results of the application of the 2D WTMM method to anisotropic monofractal self-affine rough surfaces.

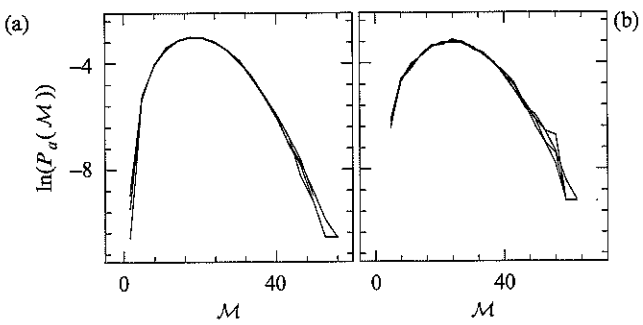

FIGURE 16. Pdf of $\mathcal{M}$ as conditioned by $\mathcal{A}$. The different curves correspond to fixing $\mathcal{A}$ (mod π) to $0 \pm \pi/8, \pi/4 \pm \pi/8, \pi/2 \pm \pi/8$ and $3\pi/4 \pm \pi/8$. (a) $a = 1$; (b) $a = 2$ (in σ_W units). Same 2D WTMM computations for $B_{1/3}$ as in Figure 15.

B. Multifractal Rough Surfaces Generated by Random Cascades on Separable Wavelet Orthogonal Basis

This section is devoted to the application of the 2D WTMM method to multifractal functions synthetized from $\mathcal{W}$-cascades on separable wavelet orthogonal basis as defined in Decoster *et al.* [109]. A 2D random $\mathcal{W}$-cascade is built recursively on the two-dimensional square grid of separable wavelet orthogonal basis, involving only scales that range between a given large scale L and the scale 0 (excluded). Thus the corresponding fractal function $f(\mathbf{x})$ will not involve scales greater than L. For that purpose, we will use compactly supported wavelets defined by Daubechies [58,109]. Moreover we will mainly concentrate here on multifractal rough surfaces that display isotropic scaling and that are generated with a 2D log-normal $\mathcal{W}$-cascade. If m and σ^2 are, respectively, the mean and the variance of $\ln W$, where $\mathcal{W}$ is a multiplicative random variable with log-normal probability distribution, then, as shown in Decoster *et al.* [109], a straightforward computation leads to the following $\tau(q)$ spectrum:

$$\begin{aligned} \tau(q) &= -\log_2 < W^q > -2, \ \forall q \in \mathbb{R} \\ &= -\frac{\sigma^2}{2 \ln 2} q^2 - \frac{m}{\ln 2} q - 2 \end{aligned} \tag{42}$$

where $< \cdots >$ means ensemble average. The corresponding $D(h)$ singularity spectrum is obtained by Legendre transforming $\tau(q)$ [Eq. (23)]:

$$D(h) = -\frac{(h + m/\ln 2)^2}{2\sigma^2/\ln 2} + 2 \tag{43}$$

According to the convergence criteria established in 1D [161], we will consider only parameter values that satisfy the conditions:

$$m < 0 \qquad \text{and} \qquad \frac{|m|}{\sigma^2} > 2\sqrt{\ln 2} \tag{44}$$

Moreover, by solving $D(h) = 0$, one gets the extremal values $h_{\min}$ and $h_{\max}$:

$$\begin{aligned} h_{\min} &= -\frac{m}{\ln 2} - \frac{2\sigma}{\sqrt{\ln 2}} \\ h_{\max} &= -\frac{m}{\ln 2} + \frac{2\sigma}{\sqrt{\ln 2}} \end{aligned} \tag{45}$$

Figure 17 illustrates the computation of the maxima chains and the WTMMM for an individual image of a multifractal rough surface generated with the log-normal $\mathcal{W}$-cascade model with parameter values: $m = -0.38 \ln 2$ and $\sigma^2 = 0.03 \ln 2$. Again Figure 17b illustrates perfectly the fact that the maxima chains correspond to edge curves of the original image after smoothing by a Gaussian filter ϕ. From the WTMMM defined on these maxima chains, one constructs the WT skeleton according to the procedure described in Section II.C. From the WT skeleton of 32 (1024×1024) images like the one in Figure 17a, one computes the annealed average of the partition functions $\mathcal{Z}(q, a)$. As shown in Figure 18a, when plotted versus the scale parameter a in a logarithmic representation, these annealed average partition functions display a rather impressive scaling

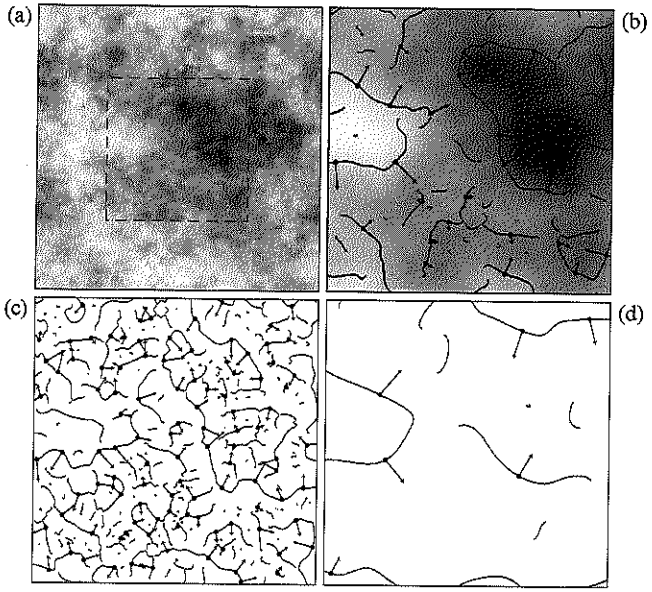

FIGURE 17. 2D wavelet transform analysis of a multifractal rough surface generated with the log-normal $\mathcal{W}$-cascade model with parameter values $m = -0.38 \ln 2$ and $\sigma^2 = 0.03 \ln 2$. ψ is the first-order radially symmetric analyzing wavelet shown in Figure 1. (a) Thirty-two gray-scale coding of the original (1024×1024) image. In (b) $a = 2^{2.9}\sigma_W$, (c) $a = 2^{1.9}\sigma_W$, and (d) $a = 2^{3.9}\sigma_W$ are shown the maxima chains and the WTMMM for the central (512×512) part of the original image [dashed square in (a)]. In (b), the smoothed image $\phi_{b,a} * f$ is shown as a gray-scale-coded background from white (min) to black (max).

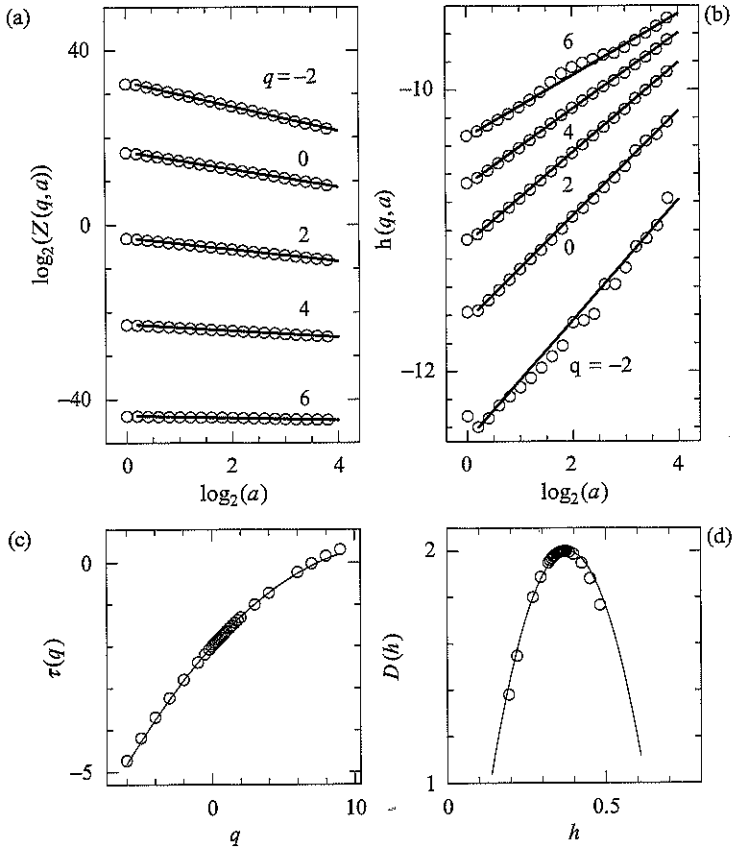

FIGURE 18. Determination of the $\tau(q)$ and $D(h)$ spectra of multifractal rough surfaces generated with the log-normal (○) random $\mathcal{W}$-cascade models, using the 2D WTMM method. ψ is the first-order radially symmetric analyzing wavelet shown in Figure 1. (a) $\log_2 \mathcal{Z}(q, a)$ vs. $\log_2 a$; the solid lines correspond to linear regression fit of the data over the first four octaves. (b) $h(q, a)$ vs. $\log_2 a$; the solid lines correspond to linear regression fit estimates of $h(q)$. (c) $\tau(q)$ vs. q as obtained from linear regression fit of the data in (a) over the first four octaves. (d) $D(h)$ vs. h, after Legendre transforming the $\tau(q)$ curve in (c). In (c) and (d), the solid lines represent the theoretical log-normal spectra given by Eqs. (42) and (43), respectively.

behavior over a range of scales of about four octaves (i.e., $\sigma_W \lesssim a \lesssim 16\sigma_W$, where $\sigma_W = 13$ pixels). Let us point out that scaling of quite good quality is found for a rather wide range of values of q: $-6 \lesssim q \lesssim 8$. When processing to a linear regression fit of the data over the first four octaves, one gets the $\tau(q)$ spectrum ($\circ$) shown in Figure 18c. For the range of q values where scaling is operating, the numerical data are in remarkable agreement with the theoretical nonlinear $\tau(q)$ spectrum given by Eq. (42). Similar quantitative agreement is observed on the $D(h)$ singularity spectrum in Figure 18d. Let us note that consistant parabolic shapes are obtained when using either the Legendre transform of the $\tau(q)$ data [Eq. (23)] or the formula (31) and (32) to compute $h(q)$ and $D(q)$. In Figure 18b are reported the results for the expectation values $h(q,a)$ [Eq. (29)] vs. $\log_2 a$; it is clear on this figure that the slope $h(q)$ depends upon q, the hallmark of multifractal scaling. Note that again, the theoretical predictions $h(q) = \partial\tau/\partial q = -\sigma^2 q/\ln 2 - m/\ln 2$ provide very satisfactory fits of the numerical data. From Eq. (45), the multifractal rough surfaces under study display intermittent fluctuations corresponding to Hölder exponent values ranging from $h_{\min} = 0.034$ to $h_{\max} = 0.726$. Unfortunately, to capture the strongest and weakest singularities, one needs to compute the $\tau(q)$ spectrum for very large values of $|q|$. This requires the processing of many more images of much larger size, which is not within current computer capabilities. Note that with the statistical sample studied here, one has $D(h(q=0) = 0.38) = 2.00 \pm 0.02$, which allows us to conclude that the rough surfaces under consideration are singular everywhere.

From the construction rule of these synthetic log-normal rough surfaces [109], the multifractal nature of these random functions is expected to be contained in the way the shape of the WT modulus pdf $P_a(\mathcal{M})$ evolves when varying the scale parameter a, as shown in Figure 19a. Indeed the joint probability distribution $P_a(\mathcal{M}, \mathcal{A})$ is expected to factorize as the signature of the implicit decoupling of $\mathcal{M}$ and $\mathcal{A}$ in the construction process. This decoupling is numerically retrieved in Figure 20 where, for two different scales, the pdf of $\mathcal{M}$, when conditioned by the argument $\mathcal{A}$, is shown to be shape invariant. When varying the scale parameter a, no significant angular-dependent evolution is observed in the distribution of the WTMMM. As seen in Figure 19b, $P_a(\mathcal{A})$ does not exhibit any significant change when increasing a, except some loss in regularity at large scales due to the rarefaction of the maxima lines. Let us point out that even though $P_a(\mathcal{A})$ looks globally rather flat, one can notice some small amplitude almost periodic oscillations at the smallest scales that reflects the existence of privileged directions in the wavelet cascading process. These oscillations are maximum for $\mathcal{A} = 0, \pi/2, \pi$ and $3\pi/2$, as the witness to the square lattice anisotropy underlying the 2D wavelet tree decomposition.

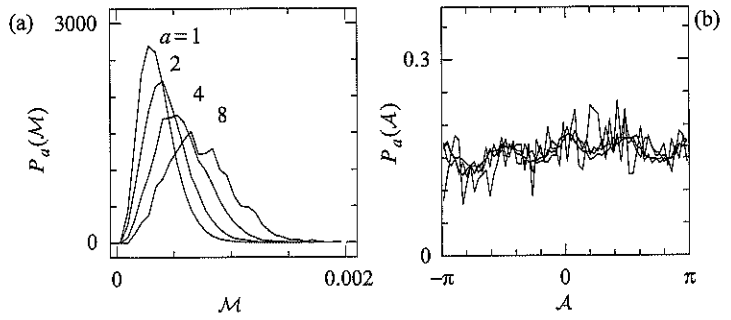

FIGURE 19. Pdfs of the WTMMM coefficients of synthetic multifractal rough surfaces generated with the log-normal $\mathcal{W}$-cascade model ($m = -0.38 \ln 2$ and $\sigma^2 = 0.03 \ln 2$). (a) $P_a(\mathcal{M})$ vs. $\mathcal{M}$. (b) $P_a(\mathcal{A})$ vs. $\mathcal{A}$. ψ is a first-order radially symmetric analyzing wavelet. Four different scales $a = 1, 2, 4, 8$ (in σ_W units) are shown. These results correspond to averaging over 32 (1024×1024) images.

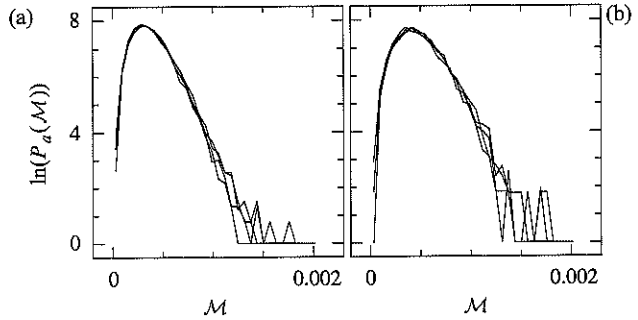

FIGURE 20. Pdfs of $\mathcal{M}$ when conditioned by $\mathcal{A}$. The different curves correspond to fixing $\mathcal{A}$ (mod π) to $0 \pm \pi/8, \pi/4 \pm \pi/8, \pi/2 \pm \pi/8$, and $3\pi/4 \pm \pi/8$. (a) $a = 2^{0.1}$; (b) $a = 2^{1.1}$ (in σ_W units). Same 2D WTMM computations as in Figure 19.

1. *Remark*

We have reported results obtained with the first-order radially symmetric analyzing wavelets shown in Figure 1. Possibly because of the range of Hölder exponent values that is restricted to $h \in [0, 1]$, but more probably because of the underlying multiplicative structure of the multifractal surface itself, a first-order analyzing wavelet leads to numerical multifractal spectra that are in remarkable agreement with the theoretical predictions. Let us point out that quite robust results are obtained with the third-order analyzing wavelet used in the previous subsection.

C. Distinguishing "Multiplicative from Additive" Processes Underlying the Scale Invariance Properties of Rough Surfaces from Space-Scale Correlation Analysis

Correlations in multifractals have already been experienced in the literature [162–164]. However, all these studies rely upon the computation of the scaling behavior of some partition functions involving different points; they thus mainly concentrate on spatial correlations of the local singularity exponents. The approach recently developed [85,100,165] is different since it does not focus on (or suppose) any scaling property but rather consists in studying the correlations of the logarithms of the amplitute of a space-scale decomposition of the signal. More specifically, if $\chi(\mathbf{x})$ is a bump function such that $\|\chi\|_1 = 1$, then by taking

$$\varepsilon^2(\mathbf{x}, a) = a^{-4} \int \chi[(\mathbf{x} - \mathbf{y})/a] |\mathbf{T}_\epsilon[f](\mathbf{y}, a)|^2 \, d^2\mathbf{y} \tag{46}$$

one has

$$\|f\|_2^2 = \iint \varepsilon^2(\mathbf{x}, a) d^2\mathbf{x} da \tag{47}$$

Thus, $\varepsilon^2(\mathbf{x}, a)$ can be interpreted as the local space-scale energy density of the considered multifractal function $f(\mathbf{x})$. Since $\varepsilon^2(\mathbf{x}, a)$ is a positive quantity, we can define the *magnitude* of the function f at the point $\mathbf{x}$ and scale a as

$$\omega(\mathbf{x}, a) = \frac{1}{2} \ln \varepsilon^2(\mathbf{x}, a) \tag{48}$$

We have shown [109] that a multiplicative process can be revealed and characterized through the correlations of its space-scale magnitudes:

$$C(\mathbf{x}_1, \mathbf{x}_2; a_1, a_2) = < \tilde{\omega}(\mathbf{x}_1, a_1) \tilde{\omega}(\mathbf{x}_2, a_2) > \tag{49}$$

where $< \cdots >$ stands for ensemble average and $\tilde{\omega}$ for the centered process $\omega - < \omega >$. When using $\mathcal{W}$-cascade process, one can compute analytically the "two-scale" correlation function $C(\Delta x, a_1, a_2)$, between the magnitude at scale a_1 and the magnitude at scale a_2. The function displays a logarithmic behavior as long as Δx is greater than the supremum of a_1 and a_2, namely [109,161,165]:

$$C(\Delta x, a_1, a_2) = \sigma^2 \left[\log_2 \left(\frac{L}{\Delta x} \right) - 2 + 2 \frac{\Delta x}{L} \right] \quad \text{when } \sup(a_1, a_2) \leq \Delta x < L \tag{50}$$

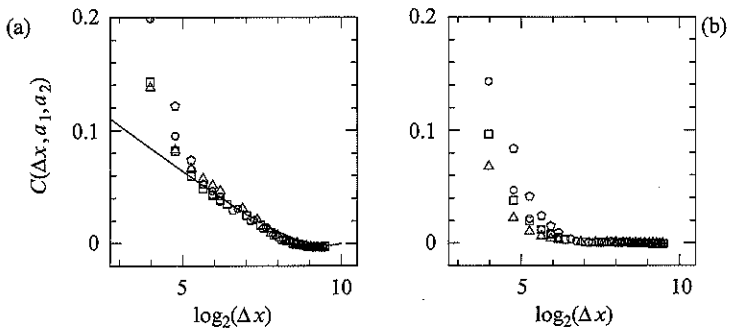

FIGURE 21. Magnitude correlation function $C(\Delta x, a_1, a_2)$ vs. $\log_2(\Delta x)$, as computed from the continuous wavelet transform of 32 (1024×1024) images. The analyzing wavelet ψ is the radially symmetric first-order wavelet shown in Figure 1. (a) Log-normal $\mathcal{W}$-cascades for parameter values $m = -0.38 \ln 2$ and $\sigma^2 = 0.03 \ln 2$. (b) Fractional Brownian surfaces $B_{H=1/3}(\mathbf{x})$. The symbols have the following meaning: $a_1 = a_2 = 2$(○); $a_1 = 1, a_2 = 2$(△); $a_1 = 1, a_2 = 2^2$(□) and $a_1 = 2, a_2 = 2^2$ (○) in σ_W units. In (a) the solid line represents the theoretical prediction given by Eq. (50). We have not shown any data points for $\Delta x \leq \sigma_W$(~ 13pixels).

Thus, the ultrametric structure of the wavelet representation of multifractal rough surfaces generated with the random $\mathcal{W}$-cascade model implies that the cross-correlation functions (across scales) decrease very slowly, independently of a_1 and a_2, as a logarithm function of the spatial distance Δx.

In Figure 21a the results of the computation of $C(\Delta x, a_1, a_2)$ when averaging over $32(1024 \times 1024)$ images of multifractal rough surfaces generated with the log-normal $\mathcal{W}$-cascade model for the same parameter values as in Figure 17a are shown. One can see that for $\Delta x > \sup(a_1, a_2)$, all the data points fall onto a unique curve when plotted versus $\log_2(\Delta x)$, independently of the considered pair of scales (a_1, a_2). Moreover, although the analyzing wavelet is different from the one used in the construction process of the $\mathcal{W}$-cascade, these numerical data are in striking good agreement with the theoretical prediction given by Eq. (50) for $\sigma^2 = 0.03 \ln 2$ and $L = 1024$. The observed slow (logarithmic) decay of the space-scale correlation functions is thus a clear indication that magnitudes in random cascades are correlated over very long distances [100,109,161,165–167]. Note that both the scale independence and the logarithmic decay are features that are not observed in "additive" models like fractional Brownian motions whose long-range correlations originate from the sign of their variations rather than from the amplitudes. In Figure 21b are plotted the correlation functions $C(\Delta x, a_1, a_2)$ computed from $32(1024 \times 1024)$ images of isotropic fractional Brownian surfaces with index $H = 1/3$ (see Fig. 9a). When compared with Figure 21a, the difference is

impressive: for $\Delta x > \sup(a_1, a_2)$, the magnitudes of $B_{H=1/3}(\mathbf{x})$ are found uncorrelated.

D. Using the 2D WTMM Method to Perform Image Processing Tasks

We now want to discuss the ability to use the WTMM method for specific purposes in image processing. We refer the reader to previous work [108] for edge detection and image denoising applications, and also to the work of Levy-Vehel [168,169] for previous attempts to use multifractal concepts for image analysis. In this subsection, we want to address a specific image processing segmentation problem that will be helpful when dealing with medical applications in Section VI. Indeed, in the past 20 years, many signal and image processing works have been devoted to medical research, especially mammography [170,171]. A major point is the detection and the characterization of clusters of microcalcifications, which are early signs of breast cancer (Section VI). Our goal is to demonstrate the ability of the 2D WTMM method to do, in a very attractive way, such a task with both synthetic surfaces and genuine mammographic scenes. Here by cluster or aggregate we mean a set of small objects in which the distances between them are small as compared to the size of the aggregate itself; otherwise there is no way of speaking of aggregate—all we have are isolated objects. Indeed the WTMM method allows us to discriminate two classes of singularities from the space-scale information embedded in the WT skeleton, and then to characterize separately the two resulting subsets by computing the corresponding partition functions and multifractal spectra [115].

In Figure 22, we show synthetic images of clusters of small spots of various heights over a background 2D fBm $B_H(\mathbf{x})$ rough surface of Hurst exponent $H = 0.6$. The trivial case of a single isolated spot is shown in Figure 22a. Figure 22b–d displays small spots located on a straight line, on the border of a filled-in Julia set and on a dense area, respectively. Let us recall that Julia sets are beautiful objects that arise in the study of iteration of rational functions on the complex plane [1,2,28]. Here we use the well-known example of a quadratic polynom as iterating function $f_c : z \to z^2 + c$, with $c = -0.85 + 0.20 * i$. The Julia set is just the set of initial seed z_0 such that the iterated sequence $(z_n)_{n\in\mathbf{N}}, z_{n+1} = z_n^2 + c$ does not go to infinity. In Figure 23 is shown the filled-in Julia set that we have used to compute Figure 22c. Each of these clusters has a known fractal dimension, respectively 0, 1, 1.68, and 2 for the point, line, Julia, and dense clusters. Although these spots are not singularities but localized structures with Gaussian shape of width $\sigma = 3$ pixels and random heights, the 2D WTMM

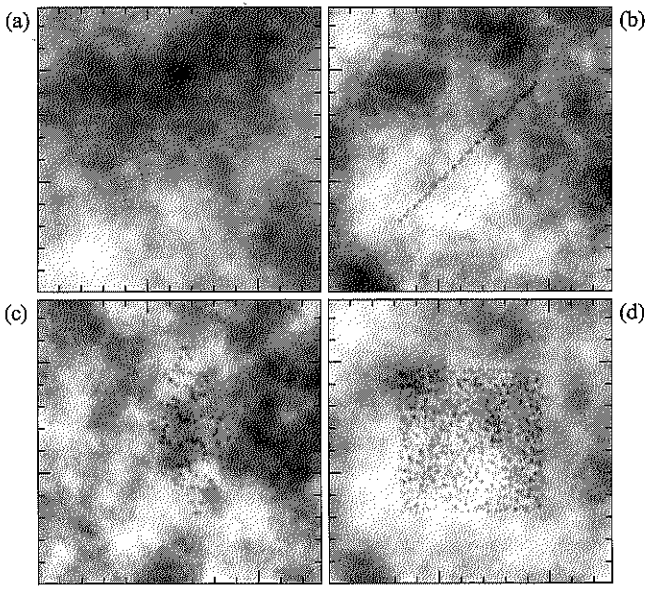

FIGURE 22. Synthetic rough surfaces (512×512) with a 2D fBm background of Hurst exponent $H = 0.6$ and containing a cluster of localized spots. (a) The cluster contains only one spot in the middle of the image; (b) the spots are located on a straight line; (c) the spots are located on a Julia set; (d) the spots are randomly distributed in a square. The spots are modeled by a gaussian of width $\sigma = 3$ pixels and height randomly chosen in the range [1.2, 1.8] in $\sigma_{B_{H=0.6}}$ unit. Same gray coding as in Figure 9.

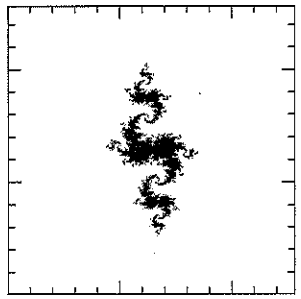

FIGURE 23. Filled-in Julia set with parameter $c = -0.85 + 0.20 * i$.

method can be used in a very efficient way to identify them and characterize the geometric properties of the aggregate to which they belong. As shown in Section II.B, in the WT skeleton, one expects the maxima lines pointing to the background texture to display local scaling properties corresponding to a 2D fBm surface, i.e. $h(x) = H = 0.6$ [Eq. (15)], whereas maxima lines pointing to clustered spots are expected to display different local scaling

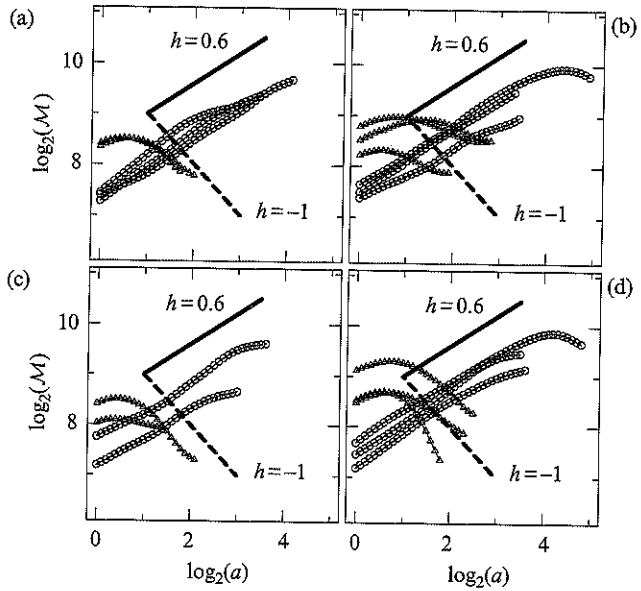

FIGURE 24. Scaling behavior of the WT modulus along some maxima lines of the WT skeletons computed from the images shown in Figure 22a, 22b, 22c and 22d respectively using the first-order radially symmetric analyzing wavelet shown in Figure 1. Symbols (○) are for maxima lines pointing to background $B_{H=0.6}$ texture singularities and (△) for those pointing to clustered small spots. The solid (resp. dashed) line corresponding to scaling exponent $h = 0.6$ (resp $h = -1$) is drawn the guide the eyes.

properties with exponent $h = -1$ since they are *seen* (at scales $a > \sigma_W > \sigma$ by our σ_W-resolved WT microscope) as Dirac singularities. Notice that because these spots are quite smooth localized structures, one expects the WTMM on these maxima lines to display a crossover at small scales ($a \gtrsim \sigma_W$) toward the behavior $\mathcal{M}_\psi[f](\mathbf{x}_0, a) \sim a^{n_\psi}, a \to 0^+$ [Eq. (17)] dictated by the number of zero moment of the analyzing wavelet. In Figure 24 are shown, in a logarithmic representation, the WT modulus versus scale parameter a for various maxima lines belonging to the WT skeletons computed from the four images in Figure 22. For each of the analyzed images, maxima lines pointing to small spots clearly display a crossover from some increase of $\mathcal{M}$ at small scales to a clear power-law decrease at large scales with a local scaling exponent $h \gtrsim -1$ that is negative and thus can be easily distinguished from the monotonous power-law increase $\mathcal{M}_\psi \sim a^{0.6}$ observed along the maxima line pointing to a $h = H = 0.6$ background singularity. Now if one proceeds to the computation of the partition functions $Z(q, a)$ on the subskeleton corresponding to identified small spots, one gets the results reported in Figure 25. Even though there are quite few maxima lines in this

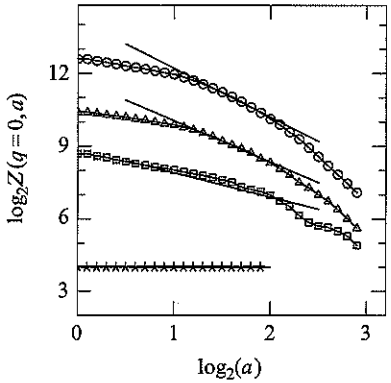

FIGURE 25. Determination of the fractal dimension $D_F = -\tau(0)$ of the cluster of localized spots in Figures 22a (○: isolated spot), 22b (△: linear cluster), 22c (□: Julia cluster) and 22d (*: dense cluster). $\log_2 Z(q = 0, a)$vs. $\log_2(a)$ as computed with the 2D WTMM method after discriminating the WT subskeleton corresponding to clustered spots as illustrated in Figure 24. The solid lines correspond to the theoretical fractal dimensions $D_F = 0, 1, 1.68$ and 2 respectively.

subskeleton, one gets a rather nice scaling behavior for small values of q. In particular the estimate of the exponent $\tau(0)$ for $q = 0$ achieves our aim to classify geometrically these clusters of localized spots. Within numerical uncertainties, one obtains the following estimates of the fractal dimensions $D_F = -\tau(0) = 0 \pm 0.02, 1 \pm 0.02, 1.7 \pm 0.04$ and 2 ± 0.02 for single spot, linear cluster, Julia cluster, and dense cluster. These results are in quite good agreement with the theoretical D_F values. They illustrate the ability of WTMM methodology to extract clustered objects from a nontrivial background and to retrieve a geometric characterization of the cluster, via the estimate of its fractal dimension D_F.

IV. Multifractal Analysis of High-Resolution Satellite Images of Cloud Structure

The problem of nonlinear variability over a wide range of scales has been considered for a long time with respect to the highly intermittent nature of turbulent flows in fluid dynamics [18,44]. Special attention has been paid to their asymptotic and possibly universal behavior when the dissipation length goes to zero, i.e., when the Reynolds number goes to infinity. Besides wind-tunnel and laboratory (grid, jet, etc.) experiments, the atmosphere is a huge natural laboratory in which high Reynolds number (fully developed) turbulent dynamics can be studied. Clouds, which are at the source of the

hydrological cycle, are the most obvious manifestation of the earth's turbulent atmospheric dynamics [10,172,173]. By modulating the input of solar radiation, they play a critical role in the maintenance of the earth's climate [174]. They are also one of the main sources of uncertainty in current climate modeling [175], where clouds are assumed to be homogeneous media lying parallel to the earth's surface; at best, a linear combination of cloudy and clear portions according to cloud fraction is used to account for horizontal inhomogeneity when predicting radiative properties. For many years, the lack of data hindered our understanding of cloud microphysics and cloud–radiation interactions. It is now well-recognized that clouds are variable in all directions and that fractal [172,173,176–181] and multifractal [10,182–184] concepts are likely to be relevant to the description of the complex 3D geometry of clouds. Until quite recently, the internal structure of clouds was probed by balloons or aircrafts that penetrated the cloud layer, revealing an extreme variability of 1D cuts of some cloud fields [184–192]. In particular, *in situ* measurements of cloud liquid water content (LWC) were performed during many intensive field programs (FIRE [193], ASTEX [194], SOCEX [195], etc.). Indeed, during the past 15 years, vast amounts of data on the distribution of atmospheric liquid water from a variety of sources were collected and analyzed in many different ways. All these data contain information on spatial and/or temporal correlations in cloudiness, enabling the investigation of scale invariance over a range from a few centimeters to hundred of kilometers. An attractive alternative to *in situ* probing is to use high-resolution satellite imagery that now provides direct information about the fluctuations in liquid water concentration in the depths of clouds [177,179–181,196–202]. These rather sophisticated remote sensing systems called "millimeter radars" are actually sensitive not only to precipating raindrops but also to suspended cloud droplets. Spectral analysis of the recorded 2D radiance field [196–202] confirms previous 1D findings that make it likely that cloud scenes display scaling over a wide range of scales.

One has to give credit to Lovejoy and co-workers [120–123,182,183,203–206] for applying the multifractal description to atmospheric phenomena. Using trace moment and double trace moment techniques [120–123, 204–206], they have brought experimental evidence for multiple scaling (or in other words, the existence of a continuum of scaling exponent values) in various geophysical fields. More recently, Davis and co-workers [184,192,202] have used the structure function method to study LWC data recorded during ASTEX and FIRE programs. Both these analyses converge to the conclusion that the internal marine stratocumulus (Sc) structure is multifractal over at least three decades in scales. Similar multifractal behavior has been reported by Wiscombe *et al.* [201] when analyzing liquid water path (LWP) data (i.e., column integrated LWC), from the Atmosperic Radiation Measurement (ARM) archives. Even though all these studies seem to agree, at least as far as their common diagnostic of multifractal scaling of the cloud structure, they all concern 1D data. To our knowledge, the structure function method has also been applied to 1D cuts of high-resolution satellite images [197,207], but we are not aware of any results coming from a specific 2D analysis. Our goal here is to take advantage of the 2D WTMM method to carry out a multifractal analysis of high-resolution satellite images of Sc cloudy scenes [106,107,110]. Beyond the issue of improving statistical characterization of *in situ* and remotly sensed data, there is a most challenging aspect, which consists in extracting structural information to constraint stochastic cloud models, which in turn will be used for radiative transfer simulations [180,182,202,208–215]. Then by comparing the multifractal properties of the numerically generated artificial radiation fields with those of actual measurements, one can hope to achieve some degree of closure.

A. Landsat Data of Marine Stratocumulus Cloud Scenes

Over the past 15 years, Landsat imagery has provided the remote sensing community at large with a very attractive and reliable tool for studying the Earth's environment [177,179–181,196–202,216,217]. One of the main advantages of high-resolution satellite imagery is its rather low effective cost as compared to outfitting and flying research aircraft. Moreover this instrument is well calibrated and it offers the possibility of reaching unusual high spatial, spectral, and radiometric resolutions [197,216]. Mainly two types of statistical analysis have been applied so far to Landsat imagery: spectral analysis of the 2D radiance field [196–200,216] and joint area and perimeter distributions for ensembles of individual clouds [177,179–181] defined by some threshold in radiance. One of the most remarkable properties of Landsat cloud scenes is their statistical scale-invariance over a rather large range of scales, which explains why fractal and multifractal concepts have progressively gained more acceptance in the atmospheric scientific community [10].

Of all cloud types, marine stratocumulus (Sc) are without doubt the ones that have attracted the most attention, mainly because of their first–order effect on the Earth's energy balance [10,173,197,216,218]. Being at once very persistent and horizontally extented, marine Sc layers carry considerable weight in the overall reflectance (albedo) of the planet and, from there, command a strong effect on its global climate [174]. Furthermore, with respect to climate modeling [175] and the major problem of cloud–radiation

interaction [182,196,197,208–211], they are presumably at their simplest in marine Sc that are relatively thin ($\sim 300 - 500$ m), with well-defined (quasiplanar) top and bottom, thus approximating the plane-parallel geometry in which radiative transfer theory is well developed [173,182, 197,209,210,213]. However, because of its internal homogeneity assumption, plane-parallel theory shows systematic biases in large-scale average reflectance [210,219] relevant to Global Circulation Model (GCM) energetics and large random errors in small-scale values [213,220] relevant to remote-sensing applications. Indeed, marine Sc have huge internal variability [184,192], not necessarily apparent to the remote observer.

In this section we challenge previous analysis [177,179–181,196–202, 216,217] of Landsat imagery using the 2D WTMM methodology [106–110] with the specific goal of improving statistical characterization of the highly intermittent radiance fluctuations of marine Sc, a prerequisite for developing better models of cloud structure and, in turn, furthering our understanding of cloud–radiation interaction. For that purpose, we analyze [110] a ($\simeq 196 \times 168$ km^2) original cloudy Landsat 5 scene captured with the TM camera (1 pixel = 30 m) in the 0.6–0.7 μm channel (i.e., reflected solar photons as opposed to their counterparts emitted in the thermal infrared) during the first ISCCP (International Satellite Cloud Climatology Project) Research Experiment (FIRE) field program [193], which took place over the Pacific Ocean off San Diego in the summer of 1987. For computational convenience, we actually select 32 overlapping 1024×1024 pixels^2 subscenes in this cloudy region. The overall extent of the explored area is about 7840 km^2. Figure 26a shows a typical (1024×1024) portion of the original image where the eight-bit gray scale coding of the quasinadir viewing radiance clearly reveals the presence of some anisotropic texture induced by convective structures that are generally aligned to the wind direction.

B. Application of the 2D WTMM Method to Landsat Images of Stratocumulus Clouds

We systematically follow the numerical implementation procedure described in Section II.C. We first wavelet transform the 32 overlapping (1024×1024) images, cut out of the original image, with the first-order ($n_\psi = 1$) radially symmetric analyzing wavelet defined in Figure 1. From the wavelet transform skeleton defined by the WTMMM, we compute the partition functions from which we extract the $\tau(q)$ and $D(h)$ multifractal spectra. We systematically test the robustness of our estimates with respect to some change in the shape of the analyzing wavelet, in particular when increasing the number of zero moments.

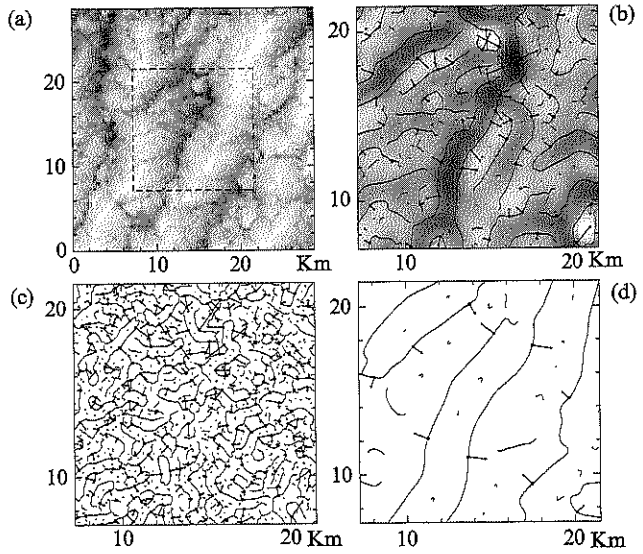

FIGURE 26. 2D wavelet transform analysis of a Landsat image of marine Sc clouds [110]. ψ (x) is the first-order radially symmetric analyzing wavelet shown in Figure 1. (a) A 256 gray-scale coding of a (1024×1024) portion of the original radiance image. In (b) $a = 2^{2.9}\sigma_W$, (c) $a = 2^{1.9}\sigma_W$, and (d) $a = 2^{3.9}\sigma_W$ (where $\sigma_W = 13$ pixels $\simeq 390$ m), are shown the maxima chains; the local maxima of $\mathcal{M}_\psi$ along these chains are indicated by (•) from which originates an arrow whose length is proportional to $\mathcal{M}_\psi$ and its direction (with respect to the x-axis) is given by $\mathcal{A}_\psi$; only the central (512×512) part delimited by a dashed square in (a) is taken into account to define the WT skeleton. In (b), the smoothed image $\phi_{b,a} * I$ is shown as a gray-scale coded background from white (min) to black (max).

1. *Numerical Computation of the Multifractal $\tau(q)$ and $D(h)$ Spectra*

Figure 26 illustrates the computation of the maxima chains and the WTMMM for the marine Sc subscene. After linking these WTMMM across scales, one constructs the WT skeleton from which one computes the partition functions $Z(q, a)$ [Eq. (21)]. As reported in Figure 27a, the annealed average partition functions (•) display some well-defined scaling behavior over the first three octaves, i.e., over the range of scales 390 m $\lesssim a \lesssim$ 3120 m, when plotted versus a in a logarithmic representation. Indeed the scaling deteriorates progressively from the large scale side when one goes to large values of $|q| \gtrsim 3$. As discussed [110], besides the fact that we are suffering from insufficient sampling, the presence of localized Dirac-like structures likely explains the fact that the observed crossover to a steeper power-law decay occurs at a smaller and a smaller scale when one increases $q > 0$. Actually for $q \gtrsim 3$, the crossover scale $a^* \lesssim 1200$ m becomes significantly smaller than the so-called integral scale, which is approximately

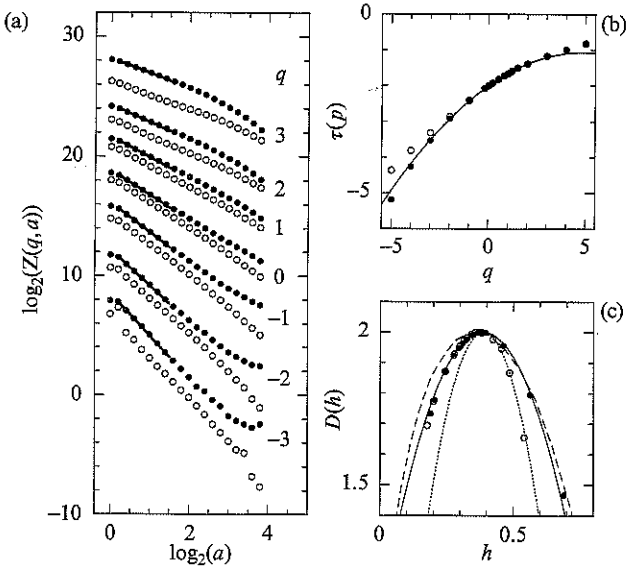

FIGURE 27. Determination of the $\tau(q)$ and $D(h)$ spectra of radiance Landsat images of marine Sc. The 2D WTMM method is used with either a first-order (•) or a third-order (○) radially symmetric analyzing wavelet (see Fig. 1). (a) $\log_2 Z(q,a)$ vs. $\log_2 a$; the solid lines correspond to linear regression fits of the data over the first octave and a half. (b) $\tau(q)$ vs. q as obtained from a linear regression fit of the data in (a). (c) $D(h)$ vs. h, after Legendre transforming the $\tau(q)$ curve in (b). In (b) and (c), the solid lines correspond to the theoretical multifractal spectra for log-normal $\mathcal{W}$-cascades with parameter values $m = -0.38 \ln 2$ and $\sigma^2 = 0.07 \ln 2$ [Eqs. (42) and (43)]. The $D(h)$ singularity spectrum of velocity (dotted line) and temperature (dashed line) fluctuations in fully developed turbulence are shown for comparison in (c).

given by the characteristic width $\lambda \simeq 1$ 5–6 km of the convective rolls (Fig. 26a). When processing to a linear regression fit of the data in Figure 27a over the first octave and a half (in order to avoid any bias induced by the presence of the observed crossover at large scales), one gets the $\tau(q)$ spectrum (•) shown in Figure 27b. In contrast to the fractional Brownian rough surfaces studied in Section III.A [108], this $\tau(q)$ spectrum unambiguously deviates from a straight line. When Legendre transforming this nonlinear $\tau(q)$ curve, one gets the $D(h)$ singularity spectrum reported in Figure 27c. Its characteristic single humped shape over a finite range of Hölder exponents is a clear indication of the multifractal nature of the marine Sc radiance fluctuations. We have checked [110] that the estimate of the $D(h)$ singularity spectrum from the scaling behavior of the partition functions $h(q,a)$ [Eq. (29)] and $D(q,a)$ [Eq. (30)] yields similar quantitative results.

In Figure 27 are also shown for comparison the results (○) obtained when applying the 2D WTMM method with a third-order ($n_\psi = 3$) radially symmetric analyzing wavelet (the smoothing function ϕ being the isotropic 2D Mexican hat). As seen in Figure 27a, the use of a wavelet that has more zero moments seems to somehow improve scaling. For the range of q-values investigated, the crossover scale turns out to be rejected at a larger scale, enlarging by some amount the range of scales over which scaling properties can be measured, especially for the largest values of $|q|$. The fact that one improves scaling when increasing the order of the analyzing wavelet suggests that perhaps some smooth behavior unfortunately deteriorates our statistical estimate of the multifractal spectra of the original Landsat radiance image. Let us recall that, as explained in Section II.B, smooth C^∞ behavior may give rise to maxima lines along which $\mathcal{M}_\psi \sim a^{n_\psi}$ (Fig. 6b); hence the larger n_ψ, the smaller is the overall contribution of those "spurious" maxima lines in the partition function summation over the WT skeleton. As seen in Figures 26a, the anisotropic texture induced by the convective streets or rolls might well be at the origin of the relative lack of well-defined scale invariance. When looking at the corresponding $\tau(q)$ spectrum (○) extracted from the data in Figure 27b, one gets quantitatively the same estimates for $q \gtrsim -1$. For more negative values of q, the data obtained with the third-order analyzing wavelet clearly depart from the previous estimates with the first-order wavelet. The slope of the new $\tau(q)$ spectrum is somehow weakened, which implies, from the Legendre transform properties, that the corresponding values of $h(q) = \partial\tau/\partial q$ are reduced. The computation of the $D(h)$ singularity spectrum (○) in Figure 27c enlightens this phenomenon: while the increasing left-hand branch (which corresponds to the strongest singularities) of the $D(h)$ curve appears to be quite robust with respect to the choise of ψ, the decreasing right-hand branch (associated to the weakest singularities) is modified when increasing the number of zero moments of ψ. As shown in Figure 27b and c, the $D(h)$ spectrum as well as the $\tau(q)$ spectrum data are very well fitted by the theoretical quadratic spectra predicted for log-normal random $\mathcal{W}$-cascades [Eqs. (42) and (43)]. However, with the first-order analyzing wavelet, the best fit is obtained with the parameter values $m = -0.38 \ln 2 = -0.263$ and $\sigma^2 = 0.07 \ln 2 = 0.049$, while for the third-order wavelet these parameters take slightly different values, namely $m = -0.366 \ln 2 = -0.254$ and $\sigma^2 = 0.06 \ln 2 = 0.042$. The variance parameter σ^2 that characterizes the inter mittent nature of marine Sc radiance fluctuations is therefore somehow reduced when going from $n_\psi = 1$ to $n_\psi = 3$. Actually the lack of statistical convergence because of insufficient sampling is actually the main reason for this uncertainty in the estimate of σ^2 [110]. As previously experienced [109] for synthetic multifractal rough surfaces, an accurate

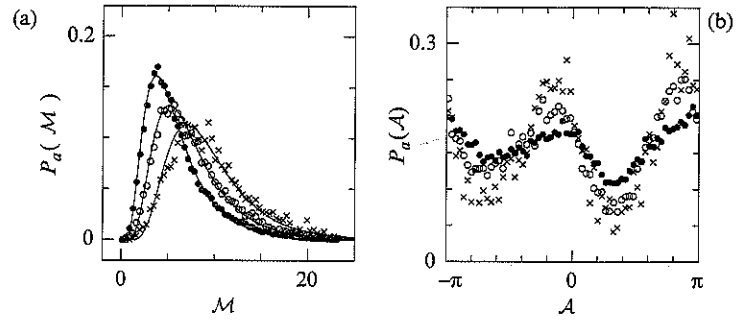

FIGURE 28. Pdfs of the WTMMM coefficients of the 32 (1024 × 1024) radiance Landsat images as computed with the first-order radially symmetric analyzing wavelet. (a) $P_a(\mathcal{M})$ vs. $\mathcal{M}$; (b) $P_a(\mathcal{A})$ vs. $\mathcal{A}$; the symbols correspond to the following scales: $a = 2^{0.3}\,\sigma_W = 480$, m(•), $2^{1.3}\sigma_W = 960$ m(○), and $2^{2.3}\,\sigma_W = 1920$ m (×). The solid lines in (a) correspond to log-normal distributions.

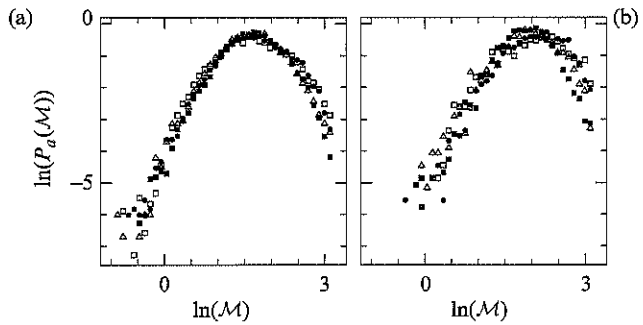

FIGURE 29. Pdfs of the WTMMM coefficients of the 32 (1024 × 1024) radiance Landsat images as computed with a first-order radially symmetric analyzing wavelet. Pdfs of $\mathcal{M}$ when conditioned by $\mathcal{A}$. The different symbols correspond to fixing $\mathcal{A}$ (mod π) to $0 \pm \pi/8$(○), $\pi/4 \pm \pi/8$ (□), $\pi/2 \pm \pi/8$ (△), and $3\pi/4 \pm \pi/8$ (▩). (a) $a = 2^{0.3}\sigma_W = 480$, m; (b) $a = 2^{1.3}\,\sigma_W = 960$, m.

estimate of the exponents $\tau(q)$ for $q \lesssim -3$ requires more than 32 (1024 × 1024) images. With the statistical sample of Landsat images we have at our disposal, one gets $D(h(q=0) = 0.37 \pm 0.02) = 2.00 \pm 0.01$, which is a strong indication that the radiance field is singular everywhere. From the estimate of $\tau(q=2) = -1.38 \pm 0.02$, one gets the following estimate of the spectral exponent: $\beta = \tau(2) + 4 = 2.62 \pm 0.02$, i.e., a value in good agreement with previous estimates [185–189,191,196–200,216].

2. *WTMMM Probability Density Functions*

This subsection is mainly devoted to the analysis of the joint probability distribution function $P_a(\mathcal{M}, \mathcal{A})$ [108–110] as computed from the wavelet transform skeletons of the 32 (1024 × 1024) radiance images with the first-order radially symmetric analyzing wavelet ($n_\psi = 1$). In Figure 28a and b are respectively shown the pdfs $P_a(\mathcal{M}) = \int d\mathcal{A} P_a(\mathcal{M}, \mathcal{A})$ and $P_a(\mathcal{A}) = \int d\mathcal{M} P_a(\mathcal{M}, \mathcal{A})$ for three different values of the scale parameter $a = 2^{0.3}\sigma_W$ (480 m), $2^{1.3}\sigma_W$ (960 m), and $2^{2.3}\sigma_W$ (1920 m). First let us focus on the results shown in Figure 28b for $P_a(\mathcal{A})$. This distribution is clearly scale dependent with some evidence of anisotropy enhancement when going from small to large scales, in particular when one reaches scales that become comparable to the characteristic width of the convective structures (i.e., a few kilometers wide). Two peaks around the values $\mathcal{A} \simeq 1 - \pi/6$ and $5\pi/6$ become more and more pronounced as the signature of a privileged direction in the analyzed images. As one can check from a visual inspection of Figure 26a, this direction is nothing but the perpendicular to the mean direction of the convective rolls that are generally aligned to the wind direction. This is another clear indication that at large scales, the wavelet transform microscope is sensitive to the convective roll texture, a rather regular modulation superimposed to the background radiance fluctuations [107–110].

Another important message that comes out from our analysis is illustrated in Figure 29. When conditioning the pdf of $\mathcal{M}$ by the argument $\mathcal{A}$, the shape of this pdf is shown to be independent of the considered value of $\mathcal{A}$, as long as the value of the scale parameter a remains small as compared to the characteristic width of the convective structures. The observation that the joint probability distribution actually factorizes, i.e., $P_a(\mathcal{M}, \mathcal{A}) = P_a(\mathcal{M}) P_a(\mathcal{A})$, indicates that $\mathcal{M}$ and $\mathcal{A}$ are likely to be independent [107,110]. This implies that all the multifractal properties of the marine Sc radiance fluctuations are contained in the way the shape of the pdf of $\mathcal{M}$ evolves when one decreases the scale parameter a. This evolution is illustrated in Figure 28a when using a first-order radially symmetric analyzing wavelet. Since by definition the WTMMM are different from zero, $P_a(\mathcal{M})$ decreases exponentially fast to zero at zero. As previously emphasized [108], this observation is at the heart of the 2D WTMM method, which, for this reason, does not suffer any problem with divergency when estimating the $\tau(q)$ spectrum for $q < 0$. As shown in Figure 28a for any scale significantly smaller than the integral scale (~ 5–6 km, as given by the characteristic width of the convective structures), all the data points fall, within a good approximation, on a log-normal curve [106,110]. As shown [110], this experimental feature is not specific to some particular shape of the analyzing wavelet since log-normal pdfs are also found when using a third-order radially symmetric analyzing wavelet.

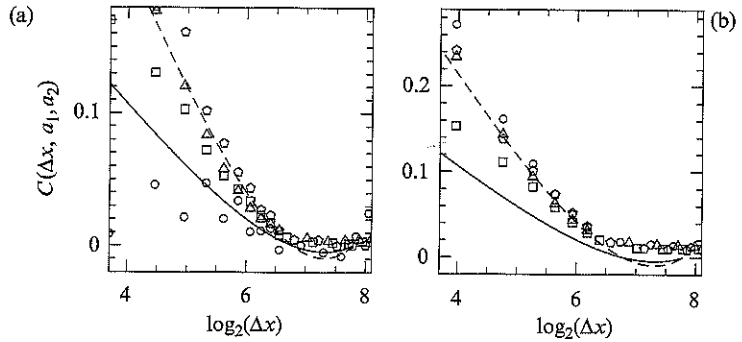

FIGURE 30. Magnitude correlation function $C(\Delta x, a_1, a_2)$ vs. $\log_2(\Delta x)$, as computed from the 32 (1024×1024) radiance Landsat images using a first-order radially symmetric analyzing wavelet. (a) WTMMM magnitude: $\omega(\mathbf{x}, a) = \ln[\mathcal{M}_\psi[f][\mathcal{L}_x(a)]]$. (b) Continuous WT magnitude: $\omega(\mathbf{x}, a) = \frac{1}{2} \ln \varepsilon^2(\mathbf{x}, a)$ [Eq. (48)]. The symbols have the following meaning: $a_1 = a_2 = 2\sigma_W = 780$, m(○); $a_1 = \sigma_W = 390$, m, $a_2 = 2\sigma a_W = 780$ m(△); $a_1 = \sigma_W = 390$ m, $a_2 = 4\sigma_W = 1560$ m (□): $a_1 = 2\sigma_W = 780$, m, $a_2 = \sigma_W = 1560$, m (⌂). The solid (dashed) lines correspond to the theoretical prediction [Eq. (50)] for multifractal rough surfaces generated with the random $\mathcal{W}$-cascade model with parameters $\sigma^2 = 0.08 \ln 2$ ($0.16 \ln 2$) and $L = 220$ pixels = 6.6 km.

C. *Space-Scale Correlation Function Analysis of Radiance Landsat Images*

As pointed out in Section III.C, the real demonstration of the existence of an underlying multiplicative structure consists in taking advantage of the space-scale unfolding provided by the continuous wavelet transform to compute the cross-scale correlation functions. In Figure 30 the results of the computation of $C(\Delta x, a_1, a_2)$ when averaging over the 32 (1024×1024) radiance Landsat images, using either the WTMMM (Fig. 30a) or the continuous WT (Fig. 30b) definition of the magnitude of f (Section III.C [110]) are reported. One can see that for $\Delta x > \sup(a_1, a_2)$, all the data points fall, in good approximation, onto a unique curve when plotted versus $\log_2(\Delta x)$, independently of the considered pair of scales (a_1, a_2). Moreover, a straight line of slope $-\sigma^2 = -0.012$ provides a rather reasonable fit of the data up to a separation distance $\Delta x \simeq 2^7$ pixels $\simeq$ 3.8 km, where decorrelation seems to be attained. Note that using the WTMMM instead of the continuous WT does not make any difference; this is a strong indication of the existence of some ultrametric properties underlying the branching structure of the space-scale wavelet representation of the radiance fluctuations. On top of the data in both Figure 30a and b, we have shown, for comparison, the theoretical prediction [Eq. (50)] for the "two-scale" correlation function of multifractal rough surfaces generated by the random $\mathcal{W}$-cascade model. This formula provides a reasonable fit of the data when adjusting the model parameters to $\sigma^2 = 0.16 \ln 2$ and $L = 220$ pixels = 6.6 km. Although the estimate of the integral scale seems to be of the right order of magnitude as regard to the characteristic width ($\lambda \sim$ 5–6 km) of the convective rolls, the value obtained for the intermittency parameter σ^2 is about twice as large as previous estimates derived from the WTMM computation of the $\tau(q)$ and $D(h)$ multifractal spectra in Figure 27. At this point, let us emphasize that a similar discrepancy has been previously noticed in the WTMM analysis of wind tunnel turbulent velocity fields [85,152]. It may suggest that simple scale-invariant self-similar cascades as pictured by the random $\mathcal{W}$-cascade model are not sophisticated enough to account for the space-scale structure of the radiance fluctuations in marine Sc clouds. The interpretation of this feature in terms of correlations between weights at a given cascade step or in terms of a more complex geometry of the tree underlying the multiplicative structure of the radiance field is underway. The possible importance of the intermittently distributed localized downward spike structures is also under consideration. Before drawing definite conclusions, there is clearly a need to repeat the "two-point" correlation function analysis on the background radiance fluctuations, once all the maxima lines corresponding to those Dirac-like singularities are removed from the WT skeleton.

D. *Comparative WTMM Multifractal Analysis of Landsat Radiance Field and Velocity and Temperature Fields in Fully Developed Turbulence*

Let us point out that a similar 1D WTMM analysis of the velocity fluctuations in high Reynolds number turbulence has come to conclusions very close to those of the present study [81–87,221]. Besides the presence of rather localized Dirac-like structures that witness the probing of vorticity filaments [62,84,127,221], the multifractal nature of turbulent velocity is likely to be understood in terms of a log-normal cascading process that is expected to be scale-invariant in the limit of very high Reynolds numbers [81–87]. In Figure 27c are shown for comparison the results obtained for the $D(h)$ singularity spectrum of the radiance Landsat images together with the $D(h)$ data extracted from the 1D analysis of a turbulent velocity signal recorded at the Modane wind tunnel ($R_\lambda \simeq 2000$) [82,85] [indeed $D(h) + 1$ is represented for the latter in order to compare 1D to 2D data]. The turbulent velocity $D(h)$ spectrum significantly differs from the results obtained for the marine Sc cloud. They have a common feature, i.e., the Hölder exponent most frequently encountered in the radiance field $h = m/\ln 2 = h(q = 0) = \partial\tau/\partial q|_{q=0} = 0.38 \pm 0.01$ is indistinguishable from the corresponding exponent $h = h(q = 0) = 0.39 \pm 0.01$ found for the turbulent velocity field. Note that these values are significantly larger than the theoretical value

$h = 1/3$ predicted by Kolmogorov in 1941 [222] to account for the observed $k^{-5/3}$ power-spectrum behavior. The main difference comes from the intermittency parameter, which is much stronger for the cloud, $\sigma^2/\ln 2 = 0.07 \pm 0.01 (n_\psi = 1)$ or $\sigma^2/\ln 2 = 0.06 \pm 0.01 (n_\psi = 3)$, than for the turbulent velocity, $\sigma^2/\ln 2 = 0.036 \pm 0.004$. This indicates that the radiance field is much more intermittent than the velocity field: the $D(h)$ singularity spectrum for the former is unambiguously wider than the corresponding spectrum for the later. For the sake of comparison, in Figure 27c we have also reported the multifractal $D(h)$ spectrum of the temperature fluctuations recorded in a $R_\lambda = 400$ turbulent flow [223]. The corresponding single humped curve is definitely much wider than the velocity $D(h)$ spectrum and it is rather close to the data corresponding to the marine Sc radiance field. It is well recognized, however, that liquid water is not really passive and that its identification with a passive component in atmospheric dynamics offers limited insight into cloud structure since, by definition, near-saturation conditions prevail and latent heat production affects buoyancy [202]. So cloud microphysical processes are expected to interact with the circulation at some, if not all, scales [224]. Nevertheless, our results in Figure 27c indicate that from a multifractal point of view, the intermittency captured by the Landsat satellite looks statistically equivalent to the intermittency of a passive scalar in fully developed 3D turbulence. The fact that the internal structure of Sc cloud somehow reflects some statistical properties of atmospheric turbulence is not such a surprise in this highly turbulent environment. The investigation of different sets of Landsat data is urgently required in order to test the degree of generality of the results reported in this first WTMM analysis of high-resolution satellite images. In particular, one may wonder to what extent the marine Sc Landsat data collected off the coast of San Diego on July 7, 1987 under specific observation conditions actually reflect the specific internal structure of Sc clouds. Work in this direction is currently in progress.

Finally, with respect to the issue of cloud modeling, the WTMM analysis of marine Sc Landsat data indicates that the 2D random $\mathcal{W}$-cascade models introduced [109] are much more realistic hierarchical models than commonly used multifractal models such as the fractionally integrated singular cascade [120,123,200,205,216] or the bounded cascade models [218,225]. We are quite optimistic in view of using the log-normal $\mathcal{W}$-cascade models with realistic parameter values for radiation transfer simulations. To our opinion, random $\mathcal{W}$-cascade models are a real breakthrough, not only for the general purpose of image synthesis, but more specifically for cloud modeling. It is likely that better cloud modeling will enable further progress in our understanding of cloud–radiation interactions possible.

V. Multifractal Analysis of 3D Turbulence Simulation Data

A. Multifractal Description of Intermittency

1. Intermittency Based on the Velocity Field

Since Kolmogorov's founding work in 1941 (K41) [222], fully developed turbulence has been intensively studied theoretically, numerically, and experimentally [18,44,226–229]. A standard way of analyzing a turbulent flow is to look for some universal statistical properties of the fluctuations of the velocity increments over a distance l:

$$\delta \mathbf{v}(\mathbf{r}, l\mathbf{e}) = \mathbf{v}(\mathbf{r} + l\mathbf{e}) - \mathbf{v}(\mathbf{r}) \tag{51}$$

where $\mathbf{e}$ is an arbitrary unit vector. For instance, investigating the scaling properties of the longitudinal structure functions:

$$S_p(l) = < (\mathbf{e}.\delta \mathbf{v}(\mathbf{r}, l\mathbf{e}))^p > \sim l^{\zeta_p}, \qquad p > 0 \tag{52}$$

where $< \cdots >$ stands for ensemble average, leads to a spectrum of scaling exponents ζ_p that has been widely used as a statistical characterization of turbulent fields [18,44,226,228,229]. Based upon assumptions of statistical homogeneity, isotropy, and constant mean energy dissipation per unit mass ϵ, K41 asymptotic theory predicts the existence of an inertial range $\eta \ll l \ll L$ for which the structure functions behave as

$$S_p(l) \sim \epsilon^{p/3} l^{p/3} \tag{53}$$

where η is the Kolmogorov dissipative scale and L the so-called integral scale. Although these assumptions are usually considered to be correct, there has been increasing numerical [18,226,230,231] and experimental [18,44,226,228,229,232–240] evidence that ζ_p deviates substantially from the K41 prediction $\zeta_p = \frac{1}{3}p$, at large p. The observed nonlinear behavior of the ζ_p spectrum actually characterizes some evolution of the longitudinal velocity increment probability density function (pdf) in the inertial range, from a Gaussian shape at large scales to stretched exponential tails toward smaller scales [228,234,235,241–245]. This evolution of the longitudinal velocity increment statistics across scales is at the heart of the multifractal description of the intermittency of small scales, pioneered by Parisi and Frisch in 1985 [43]. K41 theory is actually based on the assumption that at each point $\mathbf{r}$ of the fluid, the velocity field has the same scaling behavior $\mathbf{e}.\delta \mathbf{v}(\mathbf{r}, l\mathbf{e}) \sim l^{1/3}$, which yields the well-known $E(k) = k^{-5/3}$ energy spectrum [18]. By interpreting the nonlinear behavior of ζ_p as a direct consequence of the existence of spatial fluctuations in the local regularity of the velocity field, namely

$$\mathbf{e}.\delta\mathbf{v}(\mathbf{r}, l\mathbf{e}) \sim l^{h(\mathbf{r})} \tag{54}$$

where the exponent h depends upon $\mathbf{r}$, Parisi and Frisch [43] propose to capture intermittency in a geometric framework. For each h, if one calls $D(h)$ the fractal dimension of the set of spatial points $\mathbf{r}$ for which $h(\mathbf{r}) = h$, then by suitably inserting this local scaling behavior [Eq. (54)] into Eq. (52), one can bridge the so-called singularity spectrum $D(h)$ and the set of scaling exponent ζ_p by a Legendre transform:

$$D(h) = \min_p (ph - \zeta_p + d) \tag{55}$$

where $d = 3$ is the dimension of the velocity field. From the properties of the Legendre transform, a nonlinear ζ_p spectrum is equivalent to the assumption that there is more than a single exponent h. But as already mentioned in the introduction (Section I), Eq. (55) is valid for positive (integer) p values only, which precludes the computation of the entire $D(h)$ spectrum (in particular its right decreasing part corresponding to the weakest singularities is inaccessible to the structure function method) [50]. In the early 1990s, the 1D WTMM method [47–50] was introduced to overcome the insufficiencies of the numerical techniques commonly used to perform multifractal analysis (e.g., the structure function method, and the box-counting techniques). The use of wavelets (instead of increments or boxes) actually allows us to compute partition functions that scale like $Z(q, a) \sim a^{\tau(q)}$, where the exponents $\tau(q)$ are nothing but a generalization of the exponents ζ_p in the sense that q is now a real number going from $-\infty$ to $+\infty$. Then, as demonstrated [74,75], one can prove that by Legendre transforming the $\tau(q)$ spectrum, one gets both the increasing ($q > 0$) and the decreasing ($q < 0$) parts of the $D(h)$ singularity spectrum. Preliminary results obtained for high Reynolds wind tunnel experimental data with the 1D WTMM method have confirmed the nonlinearity of the $\tau(q)$ spectrum and consequently the multifractal nature of the longitudinal velocity fluctuations [47–49].

Let us note that from low to moderate Reynolds number turbulence, the inertial range revealed in numerical simulations as well as in experiments is rather small, which makes the estimate of the scaling exponents ζ_p and $\tau(q)$ not very accurate. Actually, the existence of scaling laws such as Eq. (52) for the structure functions [240,246,247], as well as for the WTMM partition functions [81–83,85], is not clear experimentally, even at the highest accessible Reynolds numbers. Indeed, there is a persistent curvature when one plots $\ln [S_p(l)]$ vs. $\ln (l)$, which means that, rigorously speaking, there is no scale invariance. This observation somehow questions the validity of the multifractal description. Benzi *et al.* [248–250] proposed some remedy to the observed departure from scale invariance by looking at the scaling behavior of one structure function against another. More precisely, ζ_p can be estimated from the behavior $S_p(l) \sim S_3(l)^{\zeta_p}$, if one assumes that $\zeta_3 = 1$ [18]. The relevance of the so-called extended self-similarity (ESS) hypothesis improves and further extends the scaling behavior toward the dissipative range [230,248–250]. From the application of ESS, some broad consensus among European researchers was reached in 1996 [240], at least as far as isotropic homogeneous turbulence is concerned. In this context, the ESS hypothesis has received strong support from the "propagator (across scales)" approach originally developed by Castaing and co-workers [235,246,251–257] and recently revisited with the wavelet transform methodology [81–83,85,221,258]. Let us notice that Castaing's approach can be linked to the recently proposed Fokker–Planck/Langevin description of intermittency [259–261]. According to this description, the velocity field is a Markov process across scales which suggests that the velocity increment pdf at different scales obeys a Fokker–Planck differential equation characterized by a drift and a diffusion coefficient. Even though this description remains, to a large extent, formal from a mathematical point of view and very phenomenological, it can be interesting because of its great versatility as far as scaling behavior is concerned [262]. Let us note that some theoretical works have tried to build some bridge between the Fokker–Planck approach and the Navier–Stokes dynamics [263,264]. Very recently, a systematic computation of the cumulants of the magnitude $\ln |\mathbf{e}.\delta\mathbf{v}(\mathbf{r}, l\mathbf{e})|$ of 1D longitudinal velocity profiles stemming from three different experimental setups and covering a broad range of Taylor-scaled Reynolds numbers from $R_\lambda = 89$ to 2500 has clearly revealed some inconsistency with the ESS hypothesis [87]. Indeed this study shows that the breaking of scale invariance is mainly contained in the first-order cumulant, which is found to strongly depend on Reynolds number and experimental conditions, whereas, surprisingly, the second-order cumulant displays universal scale invariance behavior from R_λ values as low as $R_\lambda \simeq 100$. Furthermore, when extrapolating these results to the limit of infinite Reynolds number, this study confirms the asymptotic validity of the log-normal multifractal description of the intermittency phenomenon; the ζ_p spectrum is quadratic:

$$\zeta_p = \tau(p) + d = -C_1 p - C_2 \frac{p^2}{2} \tag{56}$$

with a well-defined intermittency parameter $C_2 = 0.025 \pm 0.003$ [87]. Note that a plausible explanation to the scale invariance symmetry breaking observed in the magnitude first-order cumulant at finite Reynolds number [and which turns out to pollute the scaling behavior of $S_p(l)$ for every p] is the presence of anisotropic velocity fluctuations in the inertial range that are likely to originate from large-scale boundary and forcing effects. We refer

the reader to Refs. [265–268], which show how to master these anisotropic effects using the irreducible representations of the rotation group.

2. *Intermittency Based on the Energy Dissipation Field*

A central quantity in the K41 theory [222] is the mean energy dissipation ϵ, which is supposed to be constant [Eq. (53)]. The observed nonlinear behavior of the ζ_p spectrum [Eq. (56)] is generally interpreted as a direct consequence of the intermittency phenomenon displayed by ϵ, which is not spatially homogeneous but undergoes local intermittent fluctuations [18,226,227,235]. Under the so-called Kolmogorov refined similarity hypothesis (RSH) [269,270], the velocity structure functions can be rewritten as

$$\begin{aligned} S_p(l) &\sim < \epsilon_l(\mathbf{r})^{p/3} > l^{p/3} \\ &\sim l^{\tau_\epsilon(p/3)+p/3} \end{aligned} \tag{57}$$

where $\epsilon_l(\mathbf{r})$ is the spatial average of the energy dissipation over a ball of radius l centered at the point $\mathbf{r}$ and of volume $V_l \sim l^d$:

$$\epsilon_l(\mathbf{r}) = \frac{1}{V_l}\int_{V_l} \epsilon(\mathbf{r}')\mathrm{d}^d\mathbf{r}' \tag{58}$$

Note that the dissipation rate ϵ is related to the symmetric part of the strain tensor $(i,j = 1,2,3)$:

$$\begin{aligned} \epsilon &= \frac{\nu}{2}\sum\nolimits_{i,j}(\partial_j v_i + \partial_i v_j)^2 \\ &= 2\nu\sum\nolimits_{i,j} S_{ij}S_{ji}, \end{aligned} \tag{59}$$

where

$$S_{ij} = \frac{1}{2}(\partial_j v_i + \partial_i v_j) \tag{60}$$

According to Eq. (57), the scaling exponents of S_p are thus related to those of $\epsilon_l(\mathbf{r})$ [18]:

$$\zeta_p = \tau_\epsilon(p/3) + p/3 \tag{61}$$

By Legendre transforming both sides of this equation, one gets the following relationship between the singularity spectra of ϵ and $\mathbf{v}$:

$$\alpha = 3h, \qquad f_\epsilon(\alpha) = D(h) \tag{62}$$

where $f_\epsilon(\alpha)$ is the Hausdorff dimension of the set of spatial points such that $\epsilon_l(\mathbf{r})$ behaves like

$$\epsilon_l(\mathbf{r}) \sim l^{\alpha-1} \qquad \text{as} \qquad l \to 0 \tag{63}$$

Considered as a measure, the dissipation has singularities of exponent $\alpha - 1$ on sets of dimension:

$$f_\epsilon(\alpha) = \min_q(q(\alpha-1) - \tau_\epsilon(q) + d) \tag{64}$$

Several experimental and numerical works have tested various facets of the RSH hypothesis [164,221,227,250,251,271–282]. The support for the RSH is strong but not unequivocal. In the experiments, besides some possible artifact that may result from the use of the Taylor's hypothesis (which consists in substituting time derivatives for space derivatives) [18], the so-called surrogacy issue concerns the shortcoming of replacing ϵ by its surrogate:

$$\epsilon' = 15\nu\left(\frac{\partial u}{\partial x}\right)^2 \tag{65}$$

where u is the recorded longitudinal velocity component. Indeed the necessity of working with the surrogate dissipation amounts to assuming that the local dissipation ϵ is well approximated by an isotropic form, which is strictly valid in an ensemble-averaged sense in high Reynolds number flows and not obviously satisfied in real experimental conditions [283,284]. In the direct Navier–Stokes simulations (DNS), there are strong indications that the detailed structures of the pdfs of the energy dissipation and its 1D surrogate are different and that the velocity increments conditioned on ϵ'_l do not follow the RSH to the same degree as those conditioned on ϵ_l [282].

Since Richardson's cascade pioneering picture [285], multiplicative cascade models have enjoyed a lot of interest as the paradigm of methods for obtaining multifractal dissipation measures [1,2,18,67–71,76,122, 123,164,206,227]. The notion of cascade actually refers to a self-similar process whose properties are defined multiplicatively from coarse to fine scales. In that respect, it occupies a central place in the statistical theory of turbulence [18,69,226–228]. Over the past 40 years, since the log-normal model proposed by Kolmogorov [269] and Obukhov [270] (KO62) to account for the correction to K41 theory, refined cascade models have flourished in the literature such as the random β-model, the α-model, the p-model (for reviews see [18,69,227]), the log-stable models [120–123,286], and more recently the log-infinitely divisible cascade models [254,287–291] including the rather popular log-Poisson model advocated by She and Leveque [292]. Very generally, a self-similar cascade is defined by the way the scales are refined and the statistics of the multiplicative factor at each steps of the process [76,123,167,227,293,294]. One can thus distinguish

discrete cascades that involve discrete scale ratios leading to log-periodic corrections to scaling (discrete scale invariance [295,296]) from continuous cascades without preferable scale factors (continuous scale invariance). As far as the fragmentation process is concerned, one can specify whether some conservation laws are operating or not [76]; in particular one can discriminate between conservative (the measure is conserved at each cascade step) and nonconservative (only some fraction of the measure is transferred at each step) cascades. More fundamentally, there are two main classes of self-similar cascade processes: deterministic cascades that generally correspond to solvable models [69,227] and random cascades that are likely to provide more realistic models but for which some theoretical care is required as far as their multifractal limit and some basic multifractal properties (including multifractal phase transitions) are concerned [76]. As a notable member of the later class, the independent random cascades introduced by Mandelbrot [297,298] as a general model of random curdling in fully developed turbulence have a special status since they are the main random cascade model for which deep mathematical results have been obtained [299,300]. Recently, these multiplicative random cascade models have been recast in a Fokker–Planck/Langevin description of the pdf of $\ln(\epsilon_l)$ across scales [301,302].

There has been early experimental attemps to measure the $f_\epsilon(\alpha)$ singularity spectrum [Eq. (64)] of the dissipation rate ϵ with the specific goal to discriminate between the most popular multiplicative cascade models [69,227,303–305]. Surprisingly, the simplest version of the weighted curdling models proposed by Mandelbrot [297,298], namely the binomial model, turns out to account reasonably well (at least at a certain level of description) for the observed multifractal $\tau_\epsilon(q)$ and $f_\epsilon(\alpha)$ spectra (see Ref. [296] for a recent analysis). Indeed, all the existing cascade models appeal to adjustable parameters that are difficult to determine by plausible physical arguments and that generally provide enough freedom to account for the experimental data. Moreover, a quantitative validation of any model seems rather illusive since various technical difficulties may have disturbed the measurement of the dissipation multifractal spectra. We refer the reader to Ref. [306] for a review of the possible problems involved in the experimental process. We will mention only two main experimental limitations. The first one results from the fact that the multifractal model of turbulence implies a dependence of the viscous cutoff on the singularity exponent $\eta(\alpha)/L = Re^{-3/(3+\alpha)}$ [18,306–310]. It is thus a crucial question if the current hot-wire probes can resolve the scales implied by exponents α significantly less than 1, i.e., those that correspond to the strongest singularities of the dissipation measure. The second one is the fact that single probe measurement of the longitudinal velocity requires the use of the 1D surrogate dissipation ϵ' approximation [Eq. (65)], which may introduce severe bias in the estimate of the multifractal spectra mainly because of the presence of global and local anisotropic effects. A genuine 3D multifractal processing of turbulence dissipation data is at the moment feasible only for numerically simulated flows. But there is a price to pay for the additional gain of not using Taylor's frozen flow hypothesis; these simulations are still somehow limited in Reynolds number to regimes where scaling just begins to manifest itself, thus making reliable measurements of multifractal properties difficult [247,274,282,311]. Nevertheless several numerical studies [274,312] agree that, at least at low and moderate Reynolds numbers, the 1D-surrogate energy dissipation is in general more intermittent than the full field, which is found nearly log-normal in the inertial range [274,313]. Note that some departure from log-normality can be observed for high-order moments (large $q > 0$) [274] and is likely to define local anisotropic effects induced by strongly localized events [314,315].

Besides the experimental difficulties of measuring the energy dissipation field, there is some additional intrinsic limitation to the multifractal analysis of turbulent fields that comes from the numerical techniques commonly used in the literature to process the experimental as well as the numerical data. For instance, the multifractal spectra ζ_p of the longitudinal velocity and $\tau_\epsilon(q)$ of the energy dissipation are commonly computed using, respectively, the structure functions [18,43,44] and the box-counting [24,67,227] methods. The fact that the former method allows us to compute the longitudinal velocity exponents ζ_p for positive p values only explains why for many years the validity of the RSH relationships (61) and (62) has been partially tested [227,274]. More recent checks using the 1D WTMM method [221] and an alternative two-scale method [316,317] have clearly revealed the failure of Eq. (61) for negative p values when identifying ϵ with its surrogate ϵ'. This means that the decreasing part of the singularity spectra $f_{\epsilon'}(\alpha)$ and $D(h)$ (corresponding to the weakest singularities of both fields) significantly differs with respect to numerical uncertainty. Moreover, there is an implicit normalization constraint inherent to the box-counting technique, namely $\tau_\epsilon(1) = \tau'_\epsilon(1) = 0$, which makes this method quite inappropriate for studying nonconservative multiplicative cascade processes. Indeed a blind use of box-counting algorithms will always yield multifractal spectra that can be misleading compared to the theoretical spectra of the conservative cascading process.

3. *Intermittency Based on the Enstrophy Field*

An important step in the understanding of small-scale turbulence driven by expectations of universality is to proceed to a comparative statistical

analysis of dissipation and enstrophy in isotropic turbulence. Note that the enstrophy is related to the antisymmetric part of the strain tensor:

$$\begin{aligned}\Omega &= \frac{1}{2}\Sigma_{i,j}(\partial_j v_i - \partial_i v_j)^2 \\ &= 2\Sigma_{i,j}\omega_{ij}\omega_{ji}\end{aligned} \tag{66}$$

where

$$\omega_{ij} = \frac{1}{2}(\partial_j v_i - \partial_i v_j) \tag{67}$$

The relationship between $\epsilon = 2\nu S^2$ and $\Omega = 2\omega^2 (\omega = \nabla \wedge \mathbf{v}$ is the usual vorticity pseudovector) is

$$\frac{\epsilon}{\nu} = \Omega + 2\sum_{i,j}(\partial_j v_i \partial_i v_j) \tag{68}$$

From the incompressibility condition, one can show that the global averages of dissipation and enstrophy are related:

$$< \epsilon > = \nu < \Omega > \tag{69}$$

But this does not imply that their local averages $\epsilon_l(\mathbf{r})$ [Eq. (58)] and $\Omega_l(\mathbf{r})$ scale identically, where

$$\Omega_l(\mathbf{r}) = \frac{1}{V_l}\int_{V_l} \Omega(\mathbf{r}')\mathrm{d}^d\mathbf{r}'. \tag{70}$$

Nevertheless, if they do, this will imply that the power-law scaling of $< \Omega_l^q >$ and $< \epsilon_l^q >$ in the inertial range must be the same $\tau_\Omega(q) = \tau_\epsilon(q)$ and in turn the corresponding singularity spectra $f_\Omega(\alpha) = f_\epsilon(\alpha)$. There has been interesting recent controversy concerning the relative scaling properties of enstrophy and dissipation densities. Different theoretical studies have converged to the conclusion that the asymptotic scaling exponents must be equal in the limit of infinite Reynolds number [265,266,318–320]. Pioneering numerical DNS studies [321,322] have shown that the Ω field is more intermittent than the ϵ field. The 1D measurements of the streamwise components of ϵ and ω, obtained at both high and low Reynolds numbers [323,324], conclude that the degrees of intermittency in the dissipation and the enstrophy fields are not the same. This observation is corroborated by the analysis of circulation data [325]. More recent DNS studies at moderate Reynolds number ($R_\lambda = 216$) [326] confirm that there are differences between the two scalings. As suggested by Chen *et al.* [327], this difference is likely to result from the difference observed in the scaling exponents ζ_p^L and ζ_p^T of longitudinal and transverse structure functions, respectively [256,328–333]. More precisely, Chen *et al.* [327] reported numerical results that demonstrate the possible validity of a different RSH for the transverse direction (RSHT) that connects the statistics of the transverse velocity increments with the locally averaged enstrophy in the inertial range. The important implication of RSHT is the possible existence of two independent sets of scaling exponents related, respectively, to the symmetric (dissipation physics) and antisymmetric (vortex dynamics) parts of the strain rate. But some caution should be taken when extrapolating these results to high Reynolds numbers. The statistical analysis of the dissipation and enstrophy fields induced by a set of Burger vortices in He *et al.* [319] is very eloquent in that respect. For this model system, finite-range scaling exponents for ϵ and Ω are different but the asymptotic scaling exponents can be shown to be equal in the limit of infinite Reynolds number.

B. Application of the 2D WTMM Method to 2D Cuts of a Turbulent 3D Dissipation Field

In this section, we want to revisit previous multifractal analysis of the dissipation field $\epsilon(\mathbf{r})$ in isotropic turbulence using the 2D WTMM methodology described in Section II.C. Given the uncertain nature of the existing knowledge, it is important to study the scaling properties of both the dissipation and enstrophy fields without resorting to the artifacts mentioned in Section V.A. We thus employ the numerical data from DNS of isotropic turbulence carried out by Meneguzzi [334] with the same numerical code as previously developed by Vincent and Meneguzzi [231] but at a higher resolution. The DNS were performed using 512^3 mesh points in a 3D periodic box and a viscosity of 5×10^{-4}. A statistically steady state was obtained by forcing low Fourier modes in a deterministic way. The Taylor microscale Reynolds number $R_\lambda = 216$ is close to the value attained in the DNS reported [274,282,326,327]. Here we will examine only one snapshot of both dissipation and enstrophy 3D spatial fields. Indeed we will mainly proceed to a comparative multifractal analysis of 2D cuts of both fields using classical box-counting techniques and the 2D WTMM method. The corresponding $\tau_\epsilon(q)$, $\tau_\Omega(q)$, and $f_\epsilon(\alpha)$, $f_\Omega(\alpha)$ spectra will result from an annealed averaging over 512 (512×512) 2D cuts in a 512^3 cube.

Figure 31a is a picture of the fluctuations of the local dissipation as seen on an arbitrary 2D cut when using a 256 gray-level coding. The highly intermittent nature of these fluctuations is striking and further illustrated in Figure 31c on an arbitrary 1D spatial profile. We systematically follow the numerical implementation procedure described in Section II.C. We first wavelet transform the 512 (512×512) images of ϵ with the first-order

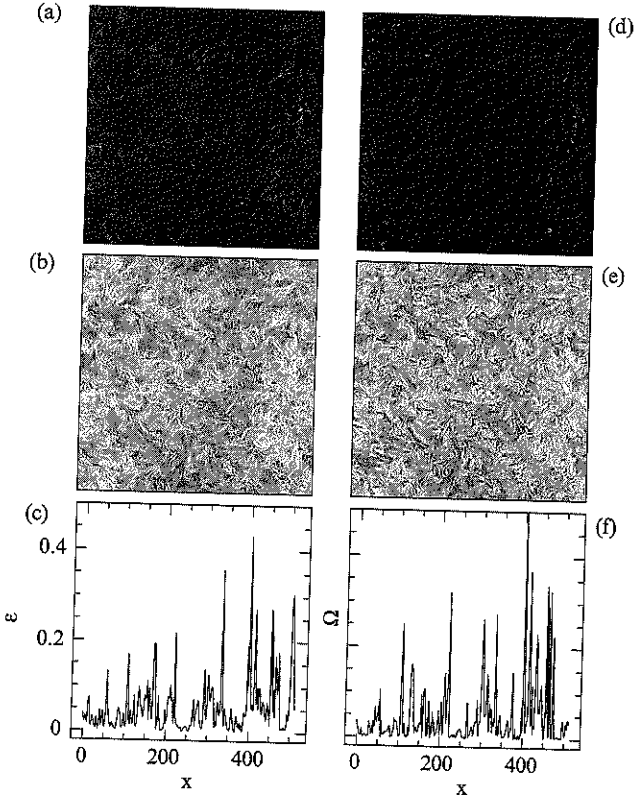

FIGURE 31. 512^3 DNS of the dissipation and enstrophy fields at $R_\lambda = 216$ [334]. Dissipation field: (a) 2D cut of $\epsilon(\mathbf{r})$; (b) 2D cut of $\ln \epsilon(\mathbf{r})$; (c) 1D cut of $\epsilon(\mathbf{r})$. Enstrophy field: (d) 2D cut of $\Omega(\mathbf{r})$; (e) 2D cut of $\ln \Omega(\mathbf{r})$; (f) 1D cut of $\Omega(\mathbf{r})$. In (a), (b), (d), and (e), ϵ and Ω are represented using a 256 gray scale coding from black (min) to white (max).

($n_\psi = 1$) and the third-order ($n_\psi = 3$) radially symmetric analyzing wavelets defined in Figure 1. From the wavelet transform skeleton defined by the WTMMM, we compute the partition functions $Z(q, a)$ from which we extract the $\tau_\epsilon(q)$ and $f_\epsilon(\alpha)$ multifractal spectra.

1. *Remark*

Let us point out that the WTMM definition of the $\tau_\epsilon^{WT}(q)$ spectrum [Eq. (22)] is slightly different from the one defined in Eq. (57) from the moments of the ϵ_l pdf ($< \epsilon_l^q > \sim l^{\tau_\epsilon(q)}$) and from the "standard" box-counting definition $\tau_\epsilon^{BC}(q)$ found in the literature, for example in Meneveau and Sreenivasan [227]:

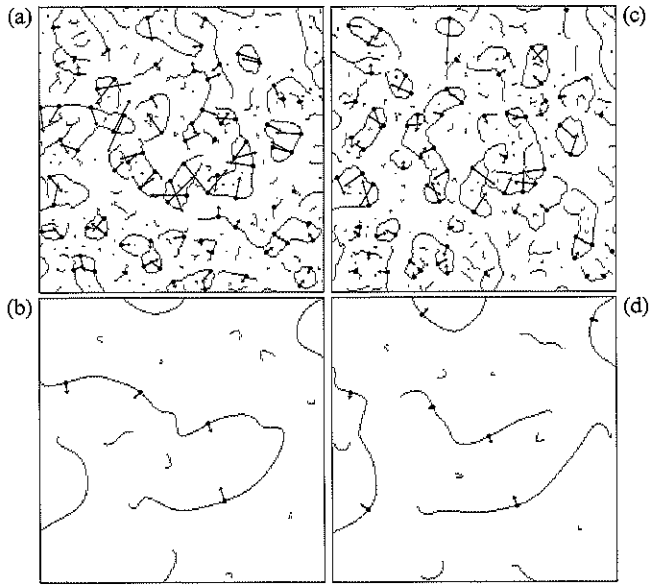

FIGURE 32. 2D wavelet transform analysis of the 2D cuts of the dissipation and enstrophy fields shown in Figure 31a and d, respectively. $\psi(\mathbf{x})$ is the first-order radially symmetric analyzing wavelet shown in Figure 1. Dissipation field: (a) $a = 2^2\sigma_W$; (b) $a = 2^4\sigma_W$. Enstrophy field: (c) $a = 2^2\sigma_W$; (d) $a = 2^4\sigma_W$. The local maxima of $\mathcal{M}_\psi$ along the maxima chains are indicated by (•) from which originates an arrow whose length is proportional to $\mathcal{M}_\psi$ and whose direction (with respect to the x-axis) is given by $\mathcal{A}_\psi$.

$$\tau_\epsilon^{WT}(q) = \tau_\epsilon(q) - d = \tau_\epsilon^{BC}(q) - dq = (q-1)D_q - dq \qquad (71)$$

where $d = 2$ when investigating 2D cuts of the 3D dissipation field and D_q are the generalized fractal dimensions defined in Refs. [20–26]. Note that the Legendre transforms used in the three different cases lead to the same estimate of the $f_\epsilon(\alpha)$ singularity spectrum.

2. *Numerical Computation of the $\tau_\epsilon(q)$ and $f_\epsilon(q)$ Multifractal Spectra*

Figure 32a and b illustrates the computation of both the maxima chains and the WTMMM of the 2D cut of ϵ shown in Figure 31a when using the first-order analyzing wavelet at two different scales. After linking these WTMMM across scales, one constructs the WT skeleton from which one computes the partition functions $Z(q, a)$ [Eq. (21)]. As shown in Figure 33a, the annealed average of $a^2 Z(q, a)(\bullet)$ displays some well-defined scaling behavior over the range of scales $2\sigma_W \lesssim a \lesssim 2^4\sigma_W$(where σ_W is the characteristic size of ψ at the smallest scale), when plotted versus a in a logarithmic representation and this for values of q in the interval $[-2, 4]$ for

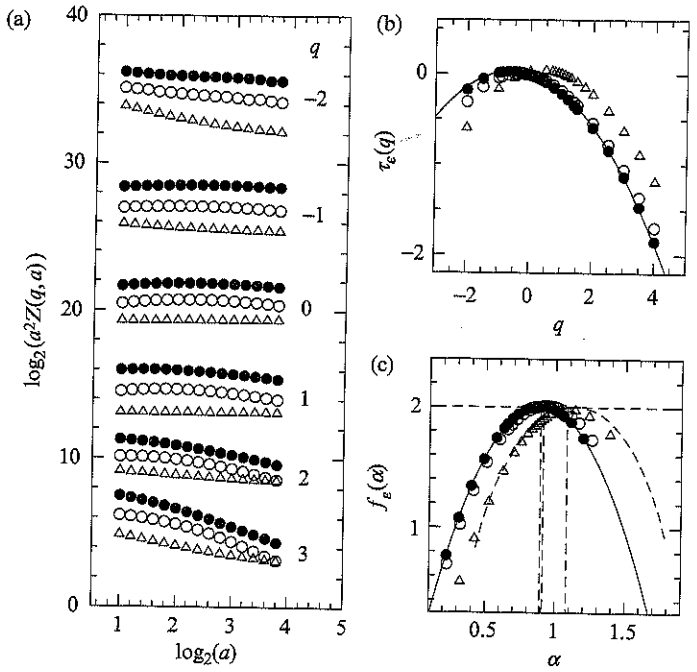

FIGURE 33. Determination of the $\tau_\epsilon(q)$ and $f_\epsilon(\alpha)$ spectra of 512 2D cuts of the dissipation field. The 2D WTMM method is used with either a first-order (•) or a third-order (○) radially symmetric analyzing wavelet (see Fig. 1). Results obtained with box-counting techniques (△) are shown for comparison. (a) $\log_2[a^2Z(q,a)]$ vs. $\log_2 a$; (b) $\tau_\epsilon(q)$ vs. q; (c) $f_\epsilon(\alpha)$ vs. α, after Legendre transforming the $\tau_\epsilon(q)$ curve in (b). In (a) the different data curves have been arbitrarily vertically shifted for the sake of clarity. In (b) and (c), the solid lines correspond, respectively, to the theoretical log-normal multifractal spectra (72) and (74) for the parameter values $C_1 = 0.11$ and $C_2 = 0.18$ [Eq. (73)]. In (c), the dashed line corresponds to the average $f(\alpha)$ spectrum obtained by Meneveau and Sreenivasan from the analysis of surrogate dissipation data using a box-counting algorithm [227].

which statistical convergence turns out to be achieved. Indeed some curvature can be observed in this logarithmic representation as the indication of some scale symmetry breaking as previously observed for the longitudinal velocity [81–83,85,221,246–258,267]. The extension of this statistical analysis to time averaging over a few turnover times is currently under progress. When processing to a linear regression fit of the data in Figure 33 over the range $2^{1.1}\sigma_W \leq a \leq 2^{3.6}\sigma_W$, one gets the $\tau_\epsilon(q)$ spectrum (•) shown in Figure 33b. In this accessible range of q values, the $\tau_\epsilon(q)$ spectrum obtained unambiguously deviates from a monofractal linear spectrum. Actually the data are remarkably well fitted by a parabola, the hallmark of log-normal multifractal spectra:

$$\tau_\epsilon(q) = -C_1 q - C_2 \frac{q^2}{2} \tag{72}$$

with

$$C_1 = 0.11 \pm 0.01, \qquad C_2 = 0.18 \pm 0.01 \tag{73}$$

By Legendre transforming this quadratic $\tau_\epsilon(q)$ spectrum, one gets data for the $f_\epsilon(\alpha)$ singularity spectrum that are well parameterized by the corresponding parabolic log-normal singularity spectrum:

$$f_\epsilon(\alpha) = 2 - \frac{(\alpha - 1 + C_1)^2}{2C_2} \tag{74}$$

We have checked that the estimate of the $f_\epsilon(\alpha)$ singularity spectrum from the scaling behavior of the partition functions $\alpha(q,a) = h(q,a) + 1$ [Eq. (29)] and $f(q,a) = D(q,a)$ [Eq. (30)] yields similar quantitative results. Figure 33 also shows for comparison the results (○) obtained when applying the 2D WTMM method with a third-order ($n_\psi = 3$) radially symmetric analyzing wavelet (the smoothing function ϕ being the isotropic 2D Mexican hat). An overall comparison with the previous results shows a remarkable robustness of the estimates of the $\tau_\epsilon(q)$ and $f_\epsilon(q)$ spectra with respect to the order of the analyzing wavelet. Both spectra are still strikingly well fitted by the log-normal multifractal model predictions [Eqs. (72) and (74), respectively] with the parameter values

$$C_1 = 0.07 \pm 0.01, \qquad C_2 = 0.19 \pm 0.01 \tag{75}$$

which, up to the numerical uncertainty, are quite consistent with the previous values in Eq. (73).

Figure 33 also shows for comparison the results (△) obtained when using classical box-counting techniques (indeed we use boxes with Gaussian shape in order to take advantage of part of our 2D WT software). It is clear in Figure 33a that the data obtained for $a^2Z(q,a)$ with the box-counting method significantly differ from those obtained with the 2D WTMM methodology. Actually, as reported in Figure 33b, the $\tau_\epsilon(q)$ data are still reasonably well accounted by the theoretical log-normal spectrum [Eq. (72)], but with significantly different parameter values:

$$C_1 = -0.09 \pm 0.01, \qquad C_2 = 0.20 \pm 0.01 \tag{76}$$

Note that the difference is not so much in the intermittency coefficient C_2, which is found to be robust to the method used to estimate it and in good agreement with the results of previous DNS studies [231,274,282,313, 326,327]. Let us emphasize that the C_2 values in Eqs. (73), (75), and (76) are at the lower bound of the range of values (0.20 to 0.28) found in

experimental measurements based on surrogate dissipation data [227,277, 303–305,323,324]. The main difference between the 2D WTMM and the box-counting results concerns the estimate of the coefficient C_1 of the linear term in $\tau_\epsilon(q)$. This is a direct consequence of the normalization constraint $\tau_\epsilon(1) = 0$ intrinsic to the box-counting method, which implies the relationship $C_1 = -C_2/2$ between the two parameters of the log-normal $\tau_\epsilon(q)$ spectrum [Eq. (72)]. The results reported in Figure 33 dramatically reveal the failure of commonly used box-counting algorithms when the considered measure results from a nonconservative log-normal multifractal process as characterized by a negative cancellation exponent [335–337] $\tau_\epsilon(1) = -0.20 \pm 0.01$, the signature of a signed measure (i.e., a distribution that varies in sign on small scales). As a consequence, the $f_\epsilon(\alpha)$ spectrum is misleadingly shifted to the right when using box-counting techniques as illustrated in Figure 33c (this shift is also present when studying 1D cuts of the dissipation field as reported in Roux's thesis [221]). This observation seriously questions the validity of most of the experimental and numerical box-counting estimates of the $f_\epsilon(\alpha)$ singularity spectrum reported so far in the literature. Figure 33c shows for comparison some average $f_\epsilon(\alpha)$ spectrum obtained by Meneveau and Sreenivasan [227] from the analysis of surrogate dissipation data; the agreement with our box-counting estimate is very good for the left increasing ($q > 0$) branch while the right decreasing ($q < 0$) branch departs somehow to a larger value of α as an indication of a slightly larger intermittency coefficient $C_2 = 0.25$ as compared to the value $C_2 = 0.20$ in Eq. (76). This is an additional indication that surrogate dissipation is likely to be more intermittent than real dissipation [282].

3. *WTMMM Probability Density Functions*

This subsection is mainly devoted to the analysis of the joint probability density function $P_a(\mathcal{M}, \mathcal{A})$ as computed from the WT skeletons of 512 2D cuts of the dissipation field with the first-order radially symmetric analyzing wavelet ($n_\psi = 1$). Figure 34a and b show the pdfs $P_a(\mathcal{M}) = \int d\mathcal{A} P_a(\mathcal{M}, \mathcal{A})$ and $P_a(\mathcal{A}) = \int d\mathcal{M} P_a(\mathcal{M}, \mathcal{A})$ for three different values of the scale parameter a in the scaling range. First let us focus on the results shown in Figure 34b for $P_a(\mathcal{A})$. $P_a(\mathcal{A})$ does not evolve accross scales and is almost flat. Actually some oscillations are observed with maxima for $\mathcal{A} = 0, \pi/2, \pi$ and $3\pi/2$ as an indication of some anisotropy induced by the cubic lattice discretization in the DNS. All the multifractal properties of ϵ 2D cuts are thus contained in the way the shape of $P_a(\mathcal{M})$ evolves when one decreases the scale parameter a as shown in Figure 34a. Actually, for the three selected scales, all the data points fall, within a good approximation, on a log-normal curve (see for comparison the pdfs in Fig. 28a), which is a strong indication

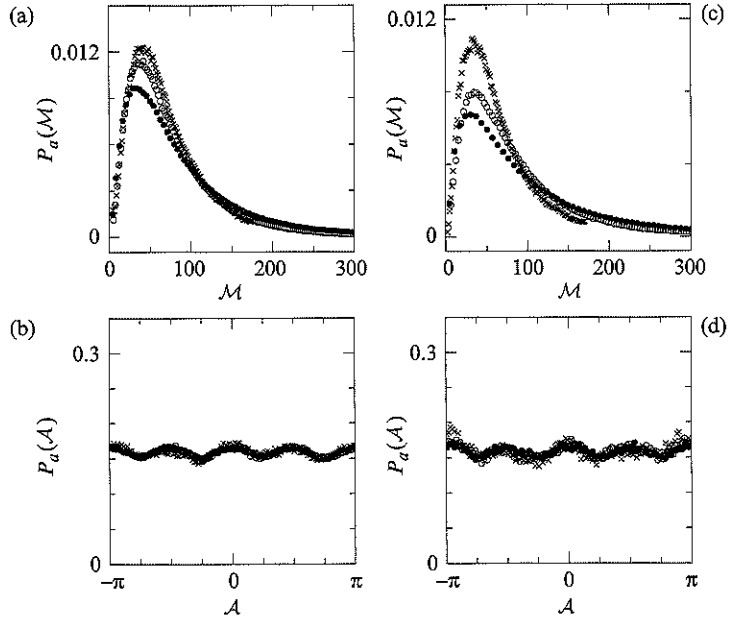

FIGURE 34. Pdfs of the WTMMM coefficients of 512 2D cuts of the dissipation and enstrophy fields as computed with the first-order radially symmetric analyzing wavelet. Dissipation field: (a) $P_a(\mathcal{M})$ vs. $\mathcal{M}$; (b) $P_a(\mathcal{A})$ vs. $\mathcal{A}$. Enstrophy field: (c) $P_a(\mathcal{M})$ vs. $\mathcal{M}$; (d) $P_a(\mathcal{A})$ vs. $\mathcal{A}$. The symbols correspond to the following scales $a = 2^1\sigma_W(\bullet), 2^2\sigma_W(\circ)$, and $2^3\sigma_W(\times)$.

that the WTMMM have a log-normal distribution in the inertial range. This observation of log-normal statistics strengthens the previous estimates of log-normal quadratic $\tau_\epsilon(q)$ and $f_\epsilon(\alpha)$ spectra. (We refer the reader to Wang *et al.* [282] for similar conclusions on the entire 3D dissipation field when using box-counting techniques.)

4. *Space-Scale Correlation Function Analysis*

As pointed out in Section III.C, to go from log-normal diagnosis to the demonstration of the existence of an underlying multiplicative structure in the 2D fluctuations of the dissipation field, one can take advantage of the space-scale unfolding provided by the WT skeleton to compute the cross-scale correlation functions. Figure 35a shows the results of the computation of $C_\epsilon(\Delta x, a_1, a_2)$ when averaging over the 512 2D cuts of ϵ. One can see that for $\Delta x > sup(a_1, a_2)$, all the data points fall onto a unique curve when plotted versus $\log_2(\Delta x)$, independently of the considered pair of scales

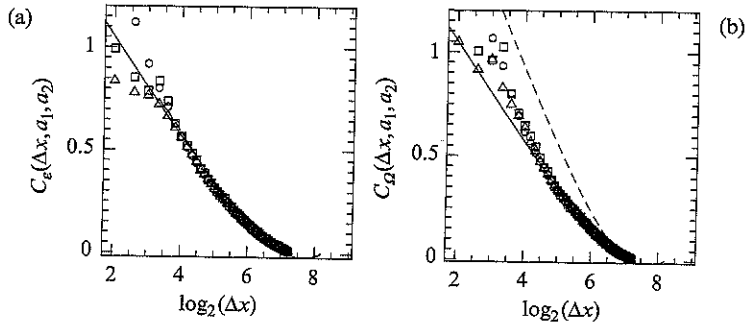

FIGURE 35. Magnitude correlation function $C(\Delta x, a_1, a_2)$ [Eq. (49)] vs. $\log_2(\Delta x)$, as computed from the WT skeleton of 512 images. The analyzing wavelet is the radially symmetric first-order wavelet shown in Figure 1. The symbols have the following meaning: $a_1 = 1, a_2 = 2(\circ)$; $a_1 = 2, a_2 = 3(\square)$; and $a_1 = 1, a_2 = 3(\triangle)$ in σ_W units. (a) Dissipation field ϵ; the solid line represents the theoretical prediction given by Eq. (50) with $\sigma^2 = C_2 \ln 2 = 0.12$ [$C_2 = 0.18$ as given by Eq. (73)]. (b) Enstrophy field Ω; the solid line has the same meaning as in (a); the dashed line represents the theoretical curve given by Eq. (50) when fixing $\sigma^2 = C_2 \ln 2 = 0.20$ [$C_2 = 0.29$ as given by Eq. (78)].

(a_1, a_2). Moreover this curve is in remarkable agreement with the theoretical prediction [Eq. (50)] for the random cascading process when plugging into this equation the value $\sigma^2 = C_2 \ln 2 = 0.12$ as previously estimated in Eq. (73). These consistent observations strongly suggest that a 2D nonconservative log-normal cascading process provides a reasonable model for the intermittent fluctuations observed along 2D cuts of the dissipation field.

C. Application of the 2D WTMM Method to 2D Cuts of a Turbulent 3D Enstrophy Field

Let us now proceed to a comparative statistical analysis of the corresponding numerical enstrophy field $\Omega(\mathbf{r})$. Figure 31d and illustrates a 2D cut of $\Omega(\mathbf{r})$ in linear and in semilogarithmic representations, respectively. The intermittent aspect of $\Omega(\mathbf{r})$ is enlightened on the 1D cut shown in Figure 31f. We proceed, as for the dissipation field in Section V.B, by applying the 2D WTMM method described in Section II.C to 512 (512×512) images of Ω with analyzing wavelets of different orders and we compare the $\tau_\Omega(q)$ and $f_\Omega(\alpha)$ multifractal spectra obtained with the corresponding estimates from box-counting computations.

1. *Numerical Computation of the Multifractal $\tau_\Omega(q)$ and $f_\Omega(q)$ Spectra*

Figure 32c and d illustrates the maxima chains and the WTMMM of the 2D cut of Ω shown in Figure 31d as computed with the first-order ($n_\psi = 1$)

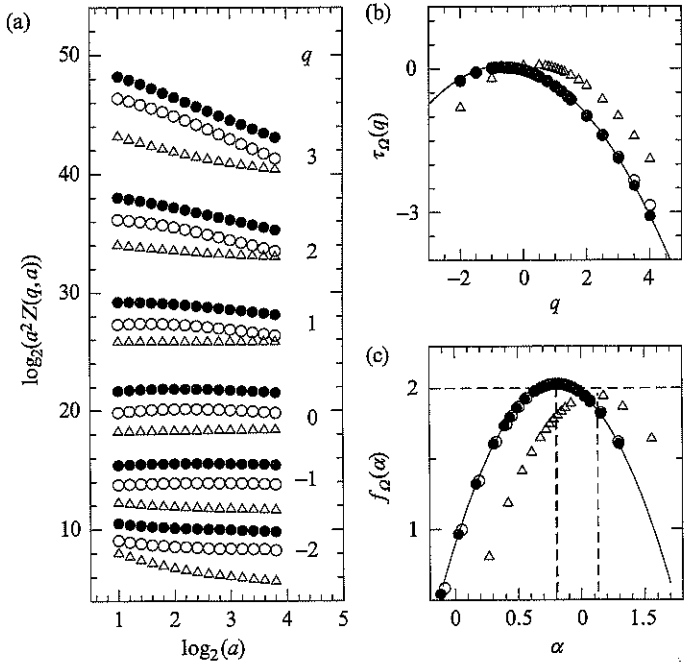

FIGURE 36. Determination of the $\tau_\Omega(q)$ and $f_\Omega(\alpha)$ spectra of 512 2D cuts of the enstrophy field. The 2D WTMM method is used with either a first-order (•) or a third-order (○) radially symmetric analyzing wavelet (see Fig. 1). Results obtained with box-counting techniques (△) are shown for comparison. (a) $\log_2[a^2 Z(q,a)]$ vs. $\log_2 a$; (b) $\tau_\Omega(q)$ vs. q; (c) $f_\Omega(\alpha)$ vs. α, after Legendre transforming the $\tau_\Omega(q)$ curve in (b). In (a) the different data curves have been arbitrarily vertically shifted for the sake of clarity. In (b) and (c), the solid lines correspond to the theoretical log-normal multifractal spectra (77) and (79) for the parameter values $C_1 = 0.19$ and $C_2 = 0.29$ [Eq. (78)].

analyzing wavelet (Fig. 1) at two different scales. After linking these WTMMM across scales, one constructs the WT skeleton from which one computes the partition functions $Z(q, a)$ [Eq. (21)]. As shown in Figure 36a, the annealed average of $a^2 Z(q, a)$(•) displays some well-defined scaling behavior over the range of scales $2\sigma_W \lesssim a \lesssim 2^4 \sigma_W$ for $-2 \lesssim q \lesssim 4$. Indeed some slight but systematic curvature can be noticed in the log–log plots very much like what has been observed for the dissipation in Figure 33a. If we proceed as in Section V.B to a linear regression fit of the data over the range $2^{1.0}\sigma_W \leq a \leq 2^{3.4}\sigma_W$, one gets the $\tau_\Omega(q)$ spectrum (•) shown in Figure 36b, which is again in quite good agreement with a parabolic log-normal spectrum:

$$\tau_\Omega(q) = -C_1 q - C_2 \frac{q^2}{2} \tag{77}$$

with

$$C_1 = 0.19 \pm 0.01, \qquad C_2 = 0.29 \pm 0.01 \tag{78}$$

Consistently, we find in Figure 36c that the corresponding $f_\Omega(\alpha)$ singularity spectrum is remarkably well fitted by the parabolic log-normal curve:

$$f_\Omega(\alpha) = 2 - \frac{(\alpha - 1 + C_1)^2}{2C_2} \tag{79}$$

Figure 36b and c also show for comparison the results (○) obtained when using the third-order ($n_\psi = 3$) analyzing wavelet. The estimates of the $\tau_\Omega(q)$ and $f_\Omega(\alpha)$ spectra are in very good agreement with the results obtained previously with the first-order ($n_\psi = 1$) analyzing wavelet. These spectra are still remarkably approximated by a parabola [Eqs. (77) and (79)] with the following parameter values:

$$C_1 = 0.18 \pm 0.01, \qquad C_2 = 0.28 \pm 0.01 \tag{80}$$

which are within the error bars of the values reported in Eq. (78).

The robustness of these multifractal spectra estimates with respect to some change in the shape of the analyzing wavelet is even more striking when one compares these estimates to those extracted from a box-counting algorithm (△). Very much like what we have observed for ϵ, this standard technique also yields parabolic spectra but with significantly different parameter values (mainly for C_1):

$$C_1 = -0.13 \pm 0.02, \qquad C_2 = 0.29 \pm 0.01 \tag{81}$$

because of the normalization requirement $\tau_\Omega(1) = 0$, i.e., $C_1 = -C_2/2$, inherent to this method. Let us point out that whatever the technique, the estimate of the intermittency parameter C_2 of the enstrophy [Eqs. (78), (80), (81)] is much larger than the corresponding value found for the dissipation [Eqs. (73), (75), (76)]. This confirms that the enstrophy field is likely to be more intermittent than the dissipation field as previously suggested [321–327]. However the WTMM method reveals that the $f_\Omega(\alpha)$ spectrum is noticeably shifted toward smaller α values (corresponding to stronger singularities) as compared to the box-counting estimate (Fig. 36c). We will come back to this point as well as to the possible nonconservative nature [$\tau_\Omega(1) \simeq -0.34 < 0$] of the underlying log-normal multiplicative structure.

2. *WTMMM Probability Density Functions*

The pdfs $P_a(\mathcal{M})$ and $P_a(\mathcal{A})$ of the WTMMM modulus and argument of the enstrophy field $\Omega(\mathbf{r})$ are shown in Figure 34c and d, respectively. Quantitatively one recovers similar results as previously observed for $\epsilon(\mathbf{r})$ (Fig. 34a and b). In Figure 34d, $P_a(\mathcal{A})$ is rather flat (with some small amplitude oscillations induced by the cubic lattice discretization in the DNS) and does not evolve across scales. When looking at $P_a(\mathcal{M})$ in Figure 34c, one sees that at each scale, the data points fall on a curve, which is well approximated by a log-normal pdf and which evolves across scales as governed by the log-normal $\tau_\Omega(q)$ spectrum computed just above [Eqs. (77) and (78)].

3. *Space-Scale Correlation Function Analysis*

In Figure 35b the results of the computation of the magnitude correlation function $C_\Omega(\Delta x, a_1, a_2)$ when averaging over the 512 2D cuts of Ω (**r**) are reported. One can see that consistently with a multiplicative cascade structure, all the data points fall onto a unique curve when plotted versus $\log_2(\Delta x)$, for $\Delta x > sup(a_1, a_2)$, and this independently of the considered pair of scales (a_1, a_2). As far as the pertinence of Eq. (50) for modeling the numerical data, it seems that when plugging this theoretical prediction into the parameter value $\sigma^2 = C_2 \ln 2 = 0.20$, according to the previous estimate of the intermittency parameter C_2 in Eq. (78), one gets a poorer agreement than when comparing it with the theoretical curve predicted for the dissipation field ($\sigma^2 = 0.12, C_2 = 0.18$). Actually, if one focuses on spatial distances Δx that are not too large (i.e., smaller than the integral scale L), for which the linear term $\sigma^2 \log_2(L/\Delta x)$ becomes dominant in Eq. (50), then the observed slope of $C_\Omega(\Delta x, a_1, a_2)$ is quite in agreement with the expected value $\sigma^2 = C_2 \ln 2 = 0.20$. The results in Figure 35b are thus an additional indication that a 2D nonconservative log-normal multiplicative process can be used to model the intermittent fluctuations observed in 2D cuts of the enstrophy field.

D. Discussion

We have used the 2D WTMM method to characterize statistically the multifractal properties of 2D cuts of both the dissipation and the enstrophy fields issued from $(512)^3$ DNS at $R_\lambda = 216$ [334]. As a general result, we find that the intermittent nature of the corresponding spatial landscape can be well modeled by a 2D nonconservative log-normal multiplicative process. To some extent this result is not so surprising since it is most likely that dissipation and enstrophy are not conserved along 2D cuts. We hope that the generalization in 3D of the WTMM method will allow us to decide whether this nonconservativity is a 2D cut effect that is likely to disappear when increasing the Reynolds number or if it is an intrinsic property of the

underlying 3D multiplicative spatial structures of both fields. Moreover the averaging over several turnover times will allow us to investigate larger values of $|q|$ (i.e., higher order moments) and possibly to evidence some departure from the theoretical log-normal multifractal spectra as suggested in Refs. [274,314,315] as an indication of some local anisotropy induced by strongly localized events (e.g., vorticity filaments). Work in this direction is in progress.

One of the main disturbing results reported in this section is the numerical demonstration that most of the numerical and experimental estimates of the multifractal spectra of ϵ and Ω fields previously reported in the literature are strongly biased by the normalization constraint $\tau(q=1)=0$ inherent to the commonly used box-counting techniques, which turn out to be quite inappropriate to study nonconservative multiplicative cascading processes. These techniques yield $f_{\epsilon,\Omega}(\alpha)$ spectra, which have almost the right width as given by the intermittency exponent C_2 but which are significantly shifted to the right (i.e., to larger α values corresponding to weakest singularities) with an estimate of the most frequent singularity $h(q=0)=\alpha(q=0)-1=-C_1$, which is misleadingly found positive instead of negative as revealed by our 2D WTMM analysis (Figs. 33c and 36c).

Finally, our comparative 2D WTMM multifractal analysis of the dissipation and enstrophy fields shows an unambiguous quantitative difference between the $f_\epsilon(\alpha)$ and $f_\Omega(\alpha)$ singularity spectra. The width of the later is significantly larger than the one of the former as given by the respective values of the intermittency parameter: $C_2^\Omega = 0.29 \pm 0.01 > C_2^\epsilon = 0.19 \pm 0.01$. Moreover $f_\Omega(\alpha)$ is maximum for $\alpha_\Omega(q=0) = h_\Omega(q=0)+1 = 1 - C_1^\Omega \simeq 0.80$, a value that is smaller than $\alpha_\epsilon(q=0) = h_\epsilon(q=0)+1 = 1 - C_1^\epsilon \simeq 0.90$ for which $f_\epsilon(\alpha)$ is maximum. These results demonstrate that the enstrophy spatial landscape is more intermittent than the dissipation spatial landscape in the sense that the support of its singularity exponent is wider and that it reaches smaller values of $h = \alpha - 1$ corresponding to stronger singularities. Note that for both fields the maximum of the $f_{\epsilon,\Omega}(\alpha)$ curves is equal to 2 $[\tau_\epsilon(q=0) = \tau_\Omega(q=0) = 0]$, which means that the corresponding 2D spatial landscapes are singular everywhere. These results confirm the conclusions of preliminary comparative box-counting studies of the dissipation and enstrophy fields [321–327]. We hope to extend this 2D WTMM analysis to the current highest accessible Reynolds number DNS with the specific goal of investigating the validity of several theoretical studies [265,266,318–320] that predict the asymptotic ($R_\lambda \to +\infty$) equality of the multifractal spectra of both fields, namely $\tau_\epsilon(q) = \tau_\Omega(q)$ and $f_\epsilon(\alpha) = f_\Omega(\alpha)$.

VI. Multifractal Analysis of Digitized Mammograms

Breast cancer, the most common cancer among women in western countries, has become a major problem of public health. Statistics indicate that in the United States approximately 1 in 10 women will develop breast cancer during her lifetime [338]. Each year, breast cancer kills about 10,000 women in France (120,000 in the world); it is still the leading cause of cancer-related death in women. It is a slowly evolving dicease; the average duration of tumor growth to obtain a palpable mass is about 10 to 15 years. Mammography (X-ray examination) is widely regarded as the most effective method for early detection of breast cancer. In the past 20 years, several national mass screening mammography programs [e.g., Health Insurance Plan of Greatest New-York (1982) and the Swedish 2-county Program of Mammography Screening for Breast Cancer (1992)] have shown that early diagnosis can significantly decrease breast cancer mortality about 23 to 31% in women aged 49 to 69 (see Dilhuydy and Barreau [339] for a complete discussion of the pros and cons of mass mammography). Because no way to prevent breast cancer (as opposed to lung cancer, for example) has been found so far, mammography actually plays a vital role in diagnosis of the decease as well as pretherapeutic management and control during and after treatment, whereas MRI (magnetic resonance imaging) and echography are helpful only when the mammogram is questionable.

However, the radiological interpretation of mammograms is a rather difficult task since the mammographic appearance of normal tissue is highly variable. In the context of breast cancer screening, abnormalities have to be detected at an early stage in a large number of asymptomatic women. For this reason, independent reading of screening mammograms by two expert radiologists is required to reduce the number of interpretation errors. In spite of this, about 10% to 30% of cancers that could have been detected are missed and a high percentage of patients called back at screening turn out not to have cancer.

Recently, much research has been devoted to developing reliable computer-aided diagnosis (CAD) methods (see Doi *et al.* [340] for a general review). Many of these methods are based on multiresolution analysis [341–344], difference image technique and global and local thresholding [345–349], statistical approaches [350–354], neural networks [355–360], fuzzy logic [361–363], and the wavelet transform (WT) and related techniques [342–344,360,362,364–371]. Currently most of these methods are often combined to detect and classify clusters of microcalcifications (MC), which are an important mammographic sign of early (*in situ*) breast cancer despite the fact that several benign diseases show MC as well [347,353,354,359,

360,362,366,367,369–373]. In the mid-1990s, fractal methods were applied to the analysis of radiographic images with some success in improving the performances of previous CAD schemes [352,374–379]. But most of these methods have been intrinsically elaborated based on the prerequesite that the background roughness fluctuations of normal breast texture are statistically homogeneous (i.e., monofractal) and uncorrelated. Regions that contain statistical aberrations that deviate from this monofractal picture are considered as abnormal regions in which tumors or MC are likely to be found. Our goal here is to propose the 2D WTMM method as an alternative method to perform multifractal analysis of digitized mammograms [115].

As we want to study scaling properties of digitized mammograms, we chose to use full-breast images from the Digital Database for Screening Mammography (DDSM) project [380], which provides online more than 2600 studies[1] sorted into three categories: normal, cancer, and benign. Mammograms were digitized using a 12-bit scanner with both a good spatial resolution of 43.5 μm. Full-breast images enable us to select about 50 overlapping 512×512 pixel squares; indeed, to master edge effects, only cores of the images were used for the computation of the WT skeleton and partition functions.

A. Application of the 2D WTMM Method to Mammographic Tissue Classification: Dense and Fatty Tissues

Several studies in the mid-1970s showed that an association existed between mammographic parenchymal patterns and the risk of developing breast cancer [381–383]. However, it appears that very few image processing works [363] have been devoted to automatic breast tissue density measurement, since Boyd *et al.* [383] studied the relation between mammographic densities and breast cancer risk using both radiological classification and semiautomatic user-assisted computer measurement based on gray-level histogram thresholding. Here we analyze normal mammary parenchyma with our multifractal 2D WTMM method with the specific goal of proposing a computerized method to calculate a breast density fluctuations index.

We have selected a set of 10 images in the DDSM database according to ACR breast density rating with some index ranking from 1 to 4, as assigned by an experienced mammographer: five fatty (rated 1 on ACR density scale) and five dense (rated 4) breasts. The main steps of the 2D WTMM computations are illustrated in Figure 37 on two full-breast images selected,

[1] http://marathon.csee.usf.edu/Mammography/Database.html.

respectively, to be representative of dense-glandular and fatty breasts. Figure 37a and e shows the original images, respectively, with the (superimposed) grid used to cut out 49 (512×512 pixels) subscenes. Figure 37b and f represents a zoom in the respective central subscenes. The corresponding WT modulus landscape and WT maxima chains computed

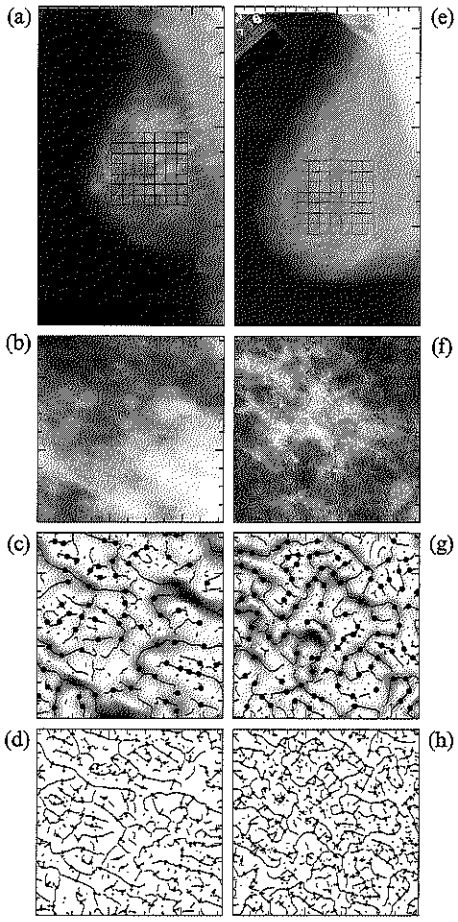

FIGURE 37. 2D wavelet transform analysis of two mammograms: (a–d) dense breast tissue and (e–h) fatty breast tissue. The analyzing wavelet is the first-order isotropic wavelet (ϕ is the isotropic gaussian function) shown in Figure 1. (a) and (e) are the two full breast images. (b) and (f) represent some zooming in the central part of the two original images. (c) and (g) show the WT modulus at the scale $a = 3\sigma_W$ with the same gray-level coding as in Figure 3c; the maxima chains are shown for comparison. In (d) and (h) only the maxima chains and the local maxima of $\mathcal{M}_\phi$ along these chains are represented (•) at the scale $a = 2.5\sigma_W$.

at the scale $a = 39$ pixels are shown in Figure 37c and g, respectively. Figure 37d and h represents, at a smaller scale, the location of the WTMMM (•) from which originate an arrow that represents the WT vector $\mathbf{T}_\epsilon[f](\mathbf{b}, a)$. Figure 38 shows the results of the computation of the partition functions $Z(q, a)$ [Eq. (21)], $h(q, a)$ [Eq. (29)], and $D(q, a)$ [Eq. (30)] obtained when averaging over 49 nonoverlapping (512 × 512) images cut out of the original dense and fatty mammograms. As shown in Figure 38a and b, both dense and fatty tissues display rather good scaling properties over two and a half octaves. The scaling actually deteriorates progressively when considering large scales, due to finite size effects. When proceeding to a linear regression fit of $\log_2[Z(q, a)]$ vs. $\log_2(a)$ over the range of scales extending from $a_{\min} = 1.6\sigma_W$ to $a_{\max} = 4\sigma_W$, one obtains the $\tau(q)$ spectra reported in Figure 38c. From a simple visual inspection, one realizes that dense and fatty breast tissues display quite different scaling properties. The latter presents a $\tau(q)$ spectrum, which is remarkably linear in the range $q \in [-3, 3]$ with a slope $H = 0.25 \pm 0.05$, while the former presents a larger slope $H = 0.65 \pm 0.05$ with some possible nonlinear departure, which might indicate multifractality. This monofractal vs. multifractal discrimination between fatty and dense breast tissues is also evidenced by the computation of the corresponding $D(h)$ singularity spectra in Figure 38d. However, the multifractal diagnosis for dense tissues requires further numerical analysis to ensure statistical convergence of the $\tau(q)$ exponents for large values of $|q|$. Nevertheless, what seems to be robust, considering the whole set of processed images, is the fact that fatty tissues display monofractal scaling behavior with a Hurst exponent H taking a value in the range [0.20,0.35] as an indication of antipersistent roughness fluctuations while dense tissues display (possibly multifractal) scaling with $H \in [0.55, 0.75]$ as an indication of persistent long-range correlations. Furthermore, in the most general case, we have shown that in any full-breast mammogram, those two kinds of tissue are present and only those two. In particular, one can assign a color (e.g., blue or red) to each square of the working grid according to its dense or fatty area identification. Work is in progress to make this segmentation independent of the square grid used to cut out subscenes. Finally, let us note that in previous work, Heine *et al.* [379,384] already used self-similarity (fractal) analysis to study mammographic density, using the Fourier power spectrum method to extract the scaling exponent $\beta = 2H + 2$ [Eq. (41)]. They obtained a histogram of β values with an average H of 0.469 and a rather small standard deviation of 0.045. This finding may be interpreted in light of our results. Indeed we may think that most of the images analyzed by Heine *et al.* Clearly contain both fatty ($H \in [0.20, 0.35]$) and dense ($H \in [0.55, 0.75]$) areas, so that the power spectrum exponent is an average of two dictinct behaviors.

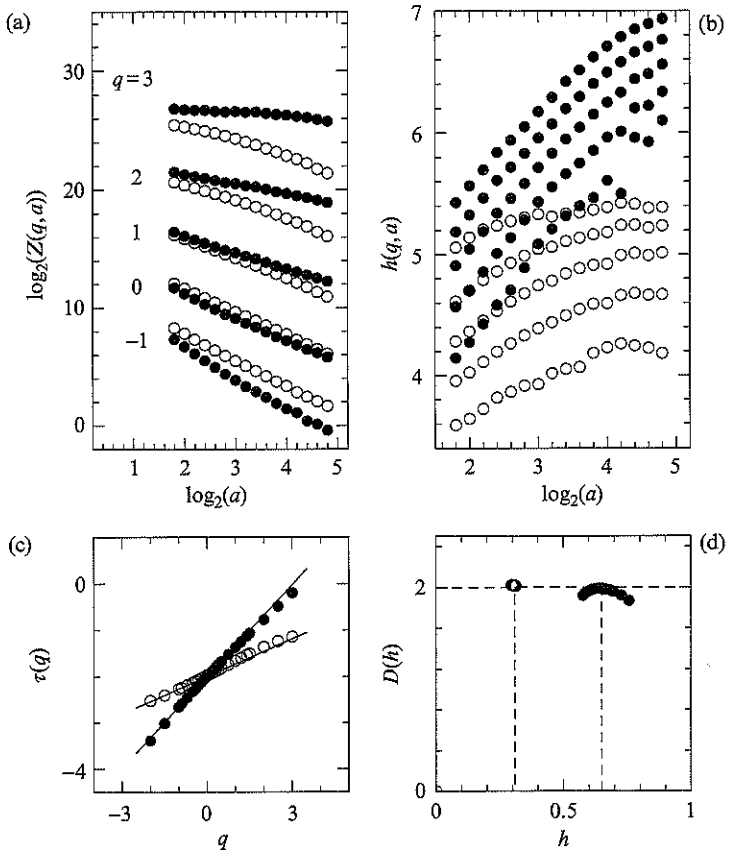

FIGURE 38. Determination of the $\tau(q)$ and $D(h)$ spectra of dense (•) and fatty (○) breasts with the 2D WTMM method. (a) $\log_2 z(q, a)$ vs. $\log_2 a$. (b) $h(q, a)$ vs. $\log_2 a$. (c) $\tau(q)$ vs. q. (d) $D(h)$ vs. h obtained from Eqs. (31) and (32). Same analyzing wavelet as in Figure 37. These results correspond to annealed averaging over 49 (512 × 512) squares cut out of full-breast images. a is expressed in σ_W units. In (a) and (b), q goes from −1 to 3 from bottom to top.

B. Detecting Microcalcifications through WT Skeleton Segmentation

The presence of clustered MC is one of the most important and sometimes the only sign of cancer in a mammogram. As a potential computer-aided diagnostic tool, let us show how our WT methodology can identify MC that are small calcium deposits in tissue, appearing as clusters of bright spots. Figure 39 illustrates how one can actually detect MC by inspecting the WT maxima chains. Indeed, at the smallest scale resolved by our WT microscope ($\sigma_W = 13$ pixels), MC, which can be considered as strong singularities, are

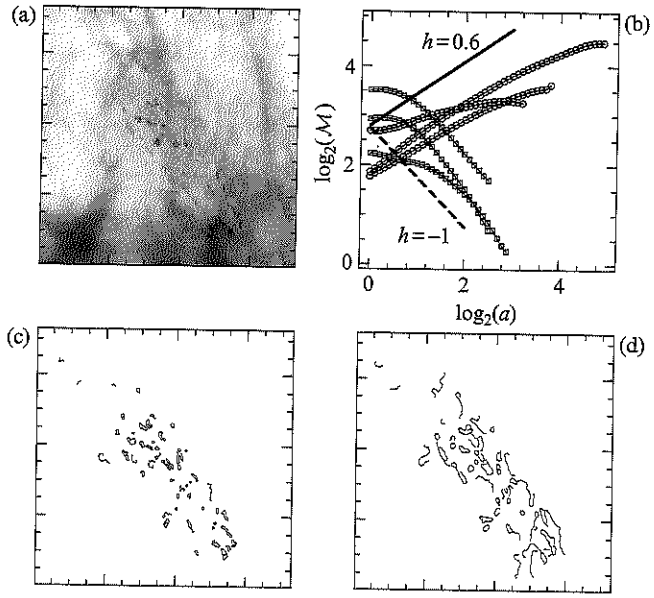

FIGURE 39. Detection and characterization of microcalcifications. (a) Original 726×726 image of dense breast tissue containing MC. (b) Scaling behavior of the WT modulus $\mathcal{M}_\psi$ along some maxima lines pointing toward dense tissue background (○) and microcalcifications (□). The solid (respectively dashed) straight line corresponds to the slope $h = 0.65$ (respectively -1) characteristic of background tissue roughness fluctuations (respectively MC). (c) and (d) show the maxima chains obtained after eliminating background tissue maxima chains at scales $a = \sigma_W$ (c) and $2.5\sigma_W$ (d), when using the WT skeleton space-scale information.

contour shaped by some maxima chains. Because the average size of MC is about $200\,\mu m$ (5 pixels), these singularities are *seen* by our mathematical microscope as Dirac singularities; thus the corresponding maxima lines pointing to the MC are likely to display scaling properties with a local Hölder exponent $h = -1 (\mathcal{M}_\psi[f] \sim a^{-1})$ down to scales of the order of the MC size where one should observe a crossover to the value $h = 0 (\mathcal{M}_\psi[f] \sim c^{st})$ as an indication of the discontinuity induced by the MC boundary. The behavior of the WT modulus along several maxima lines pointing to background points and to MC is illustrated in Figure 39b. One can thus classify these lines according to the behavior of $\mathcal{M}_\psi[f]$ along these lines, and then separate MC ($h \sim -1$) from dense background tissue ($h \sim 0.65 \pm 0.05$) as experienced on synthetic images in Section III.D. Figure 39c and d shows the maxima chains that are found to correspond to MC at two different scales. We see that these maxima chains can be used not only to detect MC at the smallest resolved scale (Fig. 39c), but also to perform MC clustering when investigating largest scales (Fig. 39d).

As pointed out in Section III.D, the MC WT subskeleton can be used to compute the corresponding partition functions, and thus to fully characterize the fractal geometry of the MC cluster. Figure 40 shows the results of the computation of the partition functions from the subskeleton of WT maxima lines pointing toward MC ($h \approx -1$). Let us recall that in this case $h(q, a)$ (Fig. 40a) is simply the average scaling behavior (see Fig. 39b) along all the maxima lines of this subskeleton. As expected, one retrieves a crossover between small scale scaling properties ($h \approx 0$ induced by the MC boundaries) and larger scale ($2\sigma_W \leq a \leq 3.7\sigma_W$) scaling properties

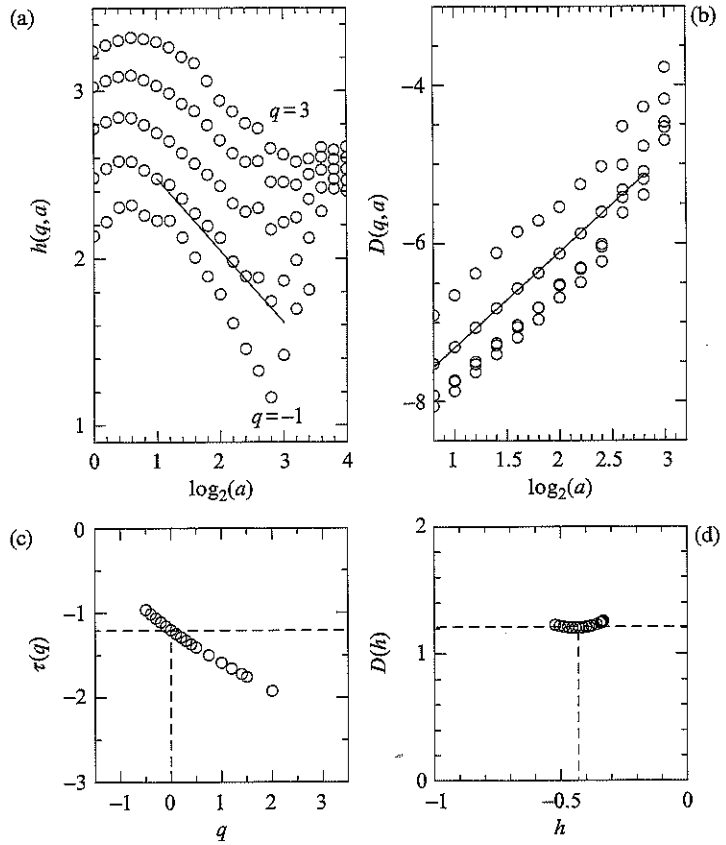

FIGURE 40. Determination of the $\tau(q)$ and $D(h)$ spectra of the MC cluster shown in Figure 39a. The partition functions are computed from the MC WT skeleton obtained after eliminating the background tissue maxima lines (see Figure 39). (a) $h(q, a)$ vs. $\log_2 a$. (b) $D(q, a)$ vs. $\log_2 a$. (c) $\tau(q)$ vs. q. (d) $D(h)$ vs. h obtained from Eqs. (31) and (32). Same analyzing wavelet as in Figure 37. a is expressed in σ_W units. The solid line in (a) corresponds to the slope $h = -0.45$ and in (b) to $D_F = 1.2$.

($h \approx -0.4$) since maxima lines, pointing toward MC, have not all reached the asymptotic ($h = -1$) Dirac singularities behavior because of finite size effects. In the same finite range of scales, $D(q, a)$ (Fig. 40b) displays good scaling properties for q values between -1 and 3, which results, to a good approximation, in a $D(h)$ singularity spectrum that reduces to a single point $h \approx -0.4$ (Fig. 40d). This result is consistent with the slope of the corresponding $\tau(q)$ spectrum (Fig. 40c) that is found to be linear up to numerical uncertainty. Moreover, from the slope of $D(q = 0, a)$ vs. $\log a$, as well as from the estimate of $\tau(0) = -D_F$, one can assign with no ambiguity the fractal dimension $D_F = 1.2 \pm 0.05$ to the MC cluster, which is definitely larger than 1 and smaller than 2, the hallmark of fractal geometry. We have also applied our methodology to a small number of benign and malign clusters; work is in progress to determine to what extent the fractal dimension of a MC cluster can be used as a discriminating index between a benign state and malignancy.

We have presented a new space-scale methodology for studying, within the same algorithmic framework, background tissue properties and abnormal singularities associated with breast cancer. For its ability to reveal and distinguish persistent and nonpersistent long-range correlations, the 2D WTMM method looks very promising in classifying tissues by quantifying breast density fluctuations in a very accurate way. Furthermore, we plan to improve detection and segmentation of MC by mixing and combining the 2D WTMM method with neural network techniques to assist in diagnosis of digitized mammograms.

VII. Conclusion

To summarize, we have presented a first step toward a statistical theory of multifractal images based on the wavelet theory. The 2D WTMM method [106–110] relies on the computation of partition functions from the WT skeleton defined by the wavelet transform modulus maxima. This skeleton provides an adaptative space-scale partition of the fractal distribution under study from which one can extract the $\tau(q)$ and $D(h)$ [or $f(\alpha)$] multifractal spectra as the equivalent of thermodynamic functions. With some appropriate choice of the analyzing wavelet, we have shown that the WTMM method provides a natural but necessary generalization of the classical box-counting and structure function techniques that both have intrinsic and fundamental limitations. Indeed we believe that the 2D WTMM method for characterizing the roughness fluctuations of a fractal landscape, a rough surface, a turbulent flow, or the image of a fractal object is likely to become as useful as the well-known phase portrait reconstruction, Poincaré section, and first return map techniques for the analysis of chaotic time series [385–388]. Besides the new concepts involved in this methodology and its potential theoretical interest, there is a more concrete and technical contribution [139] that is likely to have a strong impact on future research. For both image analysis [107,108,139] and image synthesis [109,139] purposes, we have implemented new algorithms and developed new software that can be routinely used to analyze as well as to model experimental data. In particular, some of these numerical tools take advantage of the space-scale information contained in the WT skeleton to go beyond the classical (one-point) multifractal description via the estimate of (two-point) space-scale correlation functions. Prior to experimental applications, all these numerical tools were calibrated via systematic test applications on random self-affine surfaces (e.g., isotropic fractional Brownian surfaces and anisotropic monofractal rough surfaces [108]) as well as on synthetic multifractal rough surfaces [109]. To illustrate the wide range of potential applications of this wavelet-based image processing method, we have reported the most significant results obtained when applying the 2D WTMM methodology to three rather different experimental situations, namely the statistical analysis of high-resolution satellite images of the cloud structure, of 2D cuts of the dissipation and enstrophy fields in 3D direct numerical simulations of homogeneous and isotropic trubulence, and of digitized mammograms. We are convinced that this methodology will lead to significant progress in the understanding of the multiscale mechanisms that underly the formation of rough surfaces and the spatiotemporal evolution of intermittent fields in various domains of fundamental as well as applied sciences such as erosion and corrosion processes, deposition and growth phenomena, catalysis, fracture propagation, turbulence, medical imaging, and many other areas in physics, astrophysics, chemistry, biology, geology, meteorology, and material sciences.

Acknowledgments

We are very grateful to E. Bacry, R. F. Cahalan, A. Davis, M. H. Dilhuydy, S. Jaffard, L. Lalonde, J. M. Lina, A. Marshak, J. F. Muzy, and P. Saint-Jean for very interesting and helpful discussions. We are very indebted to Y. Gagne, Y. Malécot, and S. Ciliberto for permission to use their experimental turbulent signals and to M. Meneguzzi for allowing us access to his DNS numerical data. We want to acknowledge M. H. Dilhuydy and L. Lalonde for many helpful and illuminating conversations relevant to

mammography and for providing additional training mammograms. The work concerning the analysis of Landsat satellite images of cloud structure was supported by NATO (Grant CRG 960176) and was performed while S. G. Roux held a National Research Council–NASA/GSFC Research Associateship. The work concerning the analysis of DNS turbulent dissipation and enstrophy fields is currently supported by the Centre National de la Recherche Scientifique under GDR "Turbulence."

References

1. B. B. Mandelbrot, *Fractals: Form, Chance and Dimensions* (Freeman, San Francisco, 1977).
2. B. B. Mandelbrot, *The Fractal Geometry of Nature* (Freeman, San Francisco, 1982).
3. *Random Fluctuations and Pattern Growth*, edited by H. E. Stanley and N. Ostrowski (Kluwer Academic, Dordrecht, 1988).
4. J. Feder, *Fractals* (Pergamon, New York, 1988).
5. T. Vicsek, *Fractal Growth Phenomena* (World Scientific, Singapore, 1989).
6. *The Fractal Approach to Heterogeneous Chemistry: Surfaces, Colloids, Polymers*, edited by D. Avnir (John Wiley & Sons, New York, 1989).
7. F. Family and T. Vicsek, *Dynamics of Fractal Surfaces* (World Scientific, Singapore, 1991).
8. *Fractals and Disordered Systems*, edited by A. Bunde and S. Havlin (Springer-Verlag, Berlin, 1991).
9. *Fractals in Natural Science*, edited by T. Vicsek, M. Schlesinger, and M. Matsushita (World Scientific, Singapore, 1994).
10. *Fractals in Geoscience and Remote Sensing, Image Understanding Research Series, Vol. 1, ECSC-EC-EAEC*, edited by G. G. Wilkinson, J. Kanellopoulos, and J. Megier (Brussels, Luxemburg, 1995).
11. A. L. Barabási and H. E. Stanley, *Fractal Concepts in Surface Growth* (Cambridge University Press, Cambridge, 1995).
12. *Fractal Aspects of Materials, Material Research Society Symposium Proceeding, Vol. 367*, edited by F. Family, P. Meakin, B. Sapoval, and R. Wool (Pittsburg, 1995).
13. B. Sapoval, *Les Fractales* (Aditech, Paris, 1988).
14. *On Growth and Form: Fractal and Non-Fractal Patterns in Physics*, edited by H. E. Stanley and N. Ostrowski (Martinus Nijhof, Dordrecht, 1986).
15. *Fractals in Physics*, edited by L. Pietronero and E. Tosatti (North-Holland, Amsterdam, 1986).
16. *Fractals in Physics, Essays in honour of B. B. Mandelbrot, Physica D, Vol. 38, Fractals in Physics, Essays in honour of B. B. Mandelbrot, Physica D, Vol. 38*, edited by A. Aharony and J. Feder (North-Holland, Amsterdam, 1989).
17. B. J. West, *Fractal Physiology and Chaos in Medecine* (World Scientific, Singapore, 1990).
18. U. Frisch, *Turbulence* (Cambridge University Press, Cambridge, 1995).
19. J. D. Farmer, E. Ott, and J. A. Yorke, *Physica D* **7,** 153 (1983).
20. P. Grassberger and I. Procaccia, *Phys. Rev. Lett.* **50,** 346 (1983).
21. P. Grassberger and I. Procaccia, *Physica D* **9,** 189 (1983).
22. R. Badii and A. Politi, *Phys. Rev. Lett.* **52,** 1661 (1984).
23. R. Badii and A. Politi, *J. Stat. Phys.* **40,** 725 (1985).
24. P. Grassberger, R. Badii, and A. Politi, *J. Stat. Phys.* **51,** 135 (1988).
25. G. Grasseau, Ph.D. thesis, University of Bordeaux I, 1989.
26. F. Argoul, A. Arneodo, J. Elezgaray, G. Grasseau, and R. Murenzi, *Phys. Rev. A* **41,** 5537 (1990).
27. L. V. Meisel, M. Johnson, and P. J. Cote, *Phys. Rev. A* **45,** 6989 (1992).
28. *The Science of Fractal Images, The Science of Fractal Images*, edited by H. O. Peitgen and D. Saupe (Springer-Verlag, New York, 1987).
29. R. F. Voss, *Physica D* **38,** 362 (1989).
30. G. A. Edgard, *Measures, Topology and Fractal Geometry* (Springer-Verlag, Berlin, 1990).
31. S. Davies and P. Hall, Technical Report No. SRR 96-008, School of Mathematical Sciences, National Australian University (1996).
32. B. Dubuc, J. F. Quiniou, C. Roques-Carmes, C. Tricot, and S. W. Zucker, *Phys. Rev. A* **39,** 1500 (1989).
33. T. Higuchi, *Physica D* **46,** 254 (1990).
34. N. P. Greis and H. P. Greenside, *Phys. Rev. A* **44,** 2324 (1991).
35. W. Li, *Int. J. Bifurcation Chaos.* **1,** 583 (1991).
36. J. Schmittbuhl, J. P. Violette, and S. Roux, *Phys. Rev. E* **51,** 131 (1995).
37. A. Scotti, C. Meneveau, and S. G. Saddoughi, *Phys. Rev. E* **51,** 5594 (1995).
38. B. Lea-Cox and J. S. Y. Wang, *Fractals* **1,** 87 (1993).
39. C. K. Peng, S. V. Buldyrev, M. Simons, H. E. Stanley, and A. L. Goldberger, *Phys. Rev. E* **49,** 1685 (1994).
40. M. S. Taqqu, V. Teverovsky, and W. Willinger, *Fractals* **3,** 785 (1995).
41. A. R. Mehrabi, H. Rassamdana, and M. Sahimi, *Phys. Rev. E* **56,** 712 (1997).
42. B. Pilgram and D. T. Kaplan, *Physica D* **114,** 108 (1998).
43. G. Parisi and U. Frisch, in *Turbulence and Predictability in Geophysical Fluid Dynamics and Climate Dynamics, Proc. of Int. School*, edited by M. Ghil, R. Benzi, and G. Parisi (North-Holland, Amsterdam, 1985), p. 84.
44. A. S. Monin and A. M. Yaglom, *Statistical Fluid Mechanics* (MIT Press, Cambridge, MA, 1975), Vol. 2.
45. A. L. Barabási and T. Vicsek, *Phys. Rev. A* **44,** 2730 (1991).
46. A. L. Barabási, P. Széfalusy, and T. Vicsek, *Physica A* **178,** 17 (1991).
47. J. F. Muzy, E. Bacry, and A. Arneodo, *Phys. Rev. Lett.* **67,** 3515 (1991).
48. J. F. Muzy, E. Bacry, and A. Arneodo, *Int. J. Bifurcation Chaos* **4,** 245 (1994).
49. A. Arneodo, E. Bacry, and J. F. Muzy, *Physica A* **213,** 232 (1995).
50. J. F. Muzy, E. Bacry, and A. Arneodo, *Phys. Rev. E* **47,** 875 (1993).
51. A. Grossmann and J. Morlet, S.I.A.M.*J. Math. Anal.* **15,** 723 (1984).
52. A. Grossmann and J. Morlet, in *Mathematics and Physics, Lectures on Recent Results*, edited by L. Streit (World Scientific, Singapore, 1985), p. 135.
53. P. Goupillaud, A. Grossmann, and J. Morlet, *Geoexploration* **23,** 85 (1984).
54. *Wavelets, Wavelets,* edited by J. M. Combes, A. Grossmann, and P. Tchamitchian (Springer-Verlag, Berlin, 1989).
55. Y. Meyer, *Ondelettes* (Herman, Paris, 1990).
56. *Les Ondelettes en 1989, Les Ondelettes en 1989,* edited by P. G. Lemarié (Springer-Verlag, Berlin, 1990).
57. *Wavelets and Applications, Wavelets and Applications,* edited by Y. Meyer (Springer, Berlin, 1992).
58. I. Daubechies, *Ten Lectures on Wavelets* (S.I.A.M, Philadelphia, 1992).
59. *Wavelets and Their Applications, Wavelets and Their Applications,* edited by M. B. Ruskai, G. Beylkin, R. Coifman, I. Daubechies, S. Mallat, Y. Meyer, and L. Raphael (Jones and Barlett, Boston, 1992).
60. C. K. Chui, *An Introduction to Wavelets* (Academic Press, Boston, 1992).

61. *Progress in Wavelets Analysis and Applications, Progress in Wavelets Analysis and Applications,* edited by Y. Meyer and S. Roques (Editions frontières, Gif-sur-Yvette, 1993).
62. A. Arneodo, F. Argoul, E. Bacry, J. Elezgaray, and J. F. Muzy, *Ondelettes, Multifractales et Turbulences: de l'ADN aux croissances cristallines* (Diderot Editeur, Art et Sciences, Paris, 1995).
63. *Wavelets: Theory and Applications, Wavelets: Theory and Applications,* edited by G. Erlebacher, M. Y. Hussaini, and L. M. Jameson (Oxford University Press, Oxford, 1996).
64. M. Holschneider, *Wavelets: An Analysis Tool* (Oxford University Press, Oxford, 1996).
65. S. Mallat, *A Wavelet Tour in Signal Processing* (Academic Press, New York, 1998).
66. B. Torresani, *Analyse Continue par Ondelettes* (Editions de Physique, Les Ulis, 1998).
67. T. C. Halsey, M. H. Jensen, L. P. Kadanoff, I. Procaccia, and B. I. Shraiman, *Phys. Rev. A* **33,** 1141 (1986).
68. P. Collet, J. Lebowitz, and A. Porzio, *J. Stat. Phys.* **47,** 609 (1987).
69. G. Paladin A. Vulpiani, *Phys. Rep.* **156,** 148 (1987).
70. B. B. Mandelbrot, *Fractals and Multifractals: Noise, Turbulence and Galaxies,* Vol. 1 of Selecta (Springer-Verlag, Berlin, 1989).
71. D. Rand, Ergod. Th. *Dyn. Sys.* **9,** 527 (1989).
72. S. Zhong and S. Mallat, *IEEE Trans. Pattern Anal. Machine Intelligence* **14,** 710 (1992).
73. S. Hwang and W. L. Mallat, *IEEE Trans. Inform. Theory* **38,** 617 (1992).
74. E. Bacry, J. F. Muzy, and A. Arneodo, *J. Stat. Phys.* **70,** 635 (1993).
75. S. Jaffard, SIAM *J. Math. Anal.* **28,** 944 (1997).
76. H. G. E. Hentschel, *Phys. Rev. E* **50,** 243 (1994).
77. T. Bohr and T. Tèl, in *Direction in Chaos, Vol. 2,* edited by B. L. Hao (World Scientific, Singapore, 1988), p. 194.
78. S. F. Edwards and P. W. Anderson, *J. Phys. F* **5,** 965 (1975).
79. A. Arneodo, in Ref. [63], p. 349.
80. J. F. Muzy, E. Bacry, and A. Arneodo, in Ref. [61], p. 323.
81. A. Arneodo, J. F. Muzy, and S. G. Roux, *J. Phys. II France* **7,** 363 (1997).
82. A. Arneodo, S. Manneville, and J. F. Muzy, *Eur. Phys. J. B* **1,** 129 (1998).
83. A. Arneodo, B. Audit, E. Bacry, S. Manneville, J. F. Muzy, and S. G. Roux, *Physica A* **254,** 24 (1998).
84. S. G. Roux, J. F. Muzy, and A. Arneodo, *Eur. Phys. J. B* **8,** 301 (1999).
85. A. Arneodo, S. Manneville, J. F. Muzy, and S. G. Roux, *Phil. Trans. R. Soc. London A* **357,** 2415 (1999).
86. A. Arneodo, J. Delour, and J. F. Muzy, in *Wavelet Applications in Signal and Image Processing VIII,* edited by A. Aldroubi, A. F. Laine, and M. A. Unser p. 58 (2000).
87. J. Delour, J. F. Muzy, and A. Arneodo, *Eur. Phys. J. B* **23,** 243 (2001).
88. A. Arneodo, F. Argoul, E. Bacry, J. F. Muzy, and M. Tabard, *Phys. Rev. Lett.* **68,** 3456 (1992).
89. A. Arneodo, F. Argoul, J. F. Muzy, M. Tabard, and E. Bacry, *Fractals.* **1,** 629 (1993).
90. A. Arneodo, F. Argoul, J. F. Muzy, and M Tabard, *Phys. Lett. A* **171,** 31 (1992).
91. A. Arneodo, F. Argoul, J. F. Muzy, and M. Tabard, *Physica A* **188,** 217 (1992).
92. A. Kuhn, F. Argoul, J. F. Muzy, and A. Arneodo, *Phys. Rev. Lett.* **73,** 2998 (1994).
93. A. Arneodo, E. Bacry, P. V. Graves, and J. F. Muzy, *Phys. Rev. Lett.* **74,** 3293 (1995).
94. A. Arneodo, Y. Daubenton-Carafa, E. Bacry, P. V. Graves, J. F. Muzy, and C. Thermes, *Physica D* **96,** 291 (1996).
95. A. Arneodo, Y. Daubenton-Carafa, B. Audit, E. Bacry, J. F. Muzy, and C. Thermes, *Eur. Phys. J. B* **1,** 259 (1998).
96. A. Arneodo, Y. Daubenton-Carafa, B. Audit, E. Bacry, J. F. Muzy, and C. Thermes, *Physica A* **249,** 439 (1998).
97. B. Audit, C. Thermes, C. Vaillant, Y. Daubenton-Carafa, J. F. Muzy, and A. Arneodo, *Phys. Rev. Lett.* **86,** 2471 (2001).
98. B. Audit, C. Vaillant, A. Arneodo, Y. Daubenton-Carafa, and C. Thermes, *J. Mol. Biol.* **316,** 903 (2002).
99. A. Arneodo, J. P. Bouchaud, R. Cont, J. F. Muzy, M. Potters, and D. Sornette, preprint cond-mat/9607120 at http://xxx.lanl.gov.
100. A. Arneodo, J. F. Muzy, and D. Sornette, *Eur. Phys. J. B* **2,** 277 (1998).
101. A. Arneodo, E. Bacry, and J. F. Muzy, *Phys. Rev. Lett.* **74,** 4823 (1995).
102. A. Arneodo, E. Bacry, S. Jaffard, and J. F. Muzy, *J. Stat. Phys.* **87,** 179 (1997).
103. A. Arneodo, E. Bacry, S. Jaffard, and J. F. Muzy, *J. Fourier Anal. Appl.* **4,** 159 (1998).
104. A. Arneodo, E. Bacry, S. Jaffard, and J. F. Muzy, *CRM Proc. Lecture Notes.* **18,** 315 (1999).
105. J. C. Vassilicos and J. C. Hunt, *Proc. R. Soc. London.* **435,** 505 (1991).
106. J. Arrault, A. Arneodo, A. Davis, and A. Marshak, *Phys. Rev. Lett.* **79,** 75 (1997).
107. A. Arneodo, N. Decoster, and S. G. Roux, *Phys. Rev. Lett.* **83,** 1255 (1999).
108. A. Arneodo, N. Decoster, and S. G. Roux, *Eur. Phys. J. B* **15,** 567 (2000).
109. N. Decoster, S. G. Roux, and A. Arneodo, *Eur. Phys. J. B* **15,** 739 (2000).
110. S. G. Roux, A. Arneodo, and N. Decoster, *Eur. Phys. J. B* **15,** 765 (2000).
111. J. P. Antoine, P. Carette, R. Murenzi, and B. Piette, *Signal Process.* **31,** 241 (1993).
112. E. Freysz, B. Pouligny, F. Argoul, and A. Arneodo, *Phys. Rev. Lett.* **64,** 745 (1990).
113. A. Arneodo, F. Argoul, J. F. Muzy, B. Pouligny, and E. Freysz, in Ref. [59], p. 241.
114. J. Canny, *IEEE Trans. Pattern Anal. Machine Intelligence.* **8,** 679 (1986).
115. P. Kestener, J. Lina, P. Saint-Jean, and A. Arneodo, *Image Anal. Stereol.* **20,** 169 (2001).
116. D. Marr, *Vision* (W. H. Freemann and Co, San Francisco, 1982).
117. A. Rosenfeld M. Thurston, *IEEE Trans. Comput. C* **20,** 562 (1971).
118. R. Murenzi, Ph.D. thesis, University of Louvain la Neuve, 1990.
119. R. Murenzi, in Ref. [54], p. 239.
120. D. Schertzer and S. Lovejoy, *J. Geophys. Res.* **92,** 9693 (1987).
121. D. Schertzer and S. Lovejoy, *Phys. Chem. Hyd. J.* **6,** 623 (1985).
122. S. Lovejoy and D. Schertzer, in Ref. [10], p. 102.
123. D. Schertzer, S. Lovejoy, F. Schmitt, Y. Ghigisinskaya, and D. Marsan, *Fractals.* **5,** 427 (1997).
124. S. Jaffard and Y. Meyer, *Memoirs A.M.S.* **123,** n.587 (1996).
125. M. Ben Slimane, Ph.D. thesis, E.N.P.C., France, 1996.
126. S. Jaffard, *Pub. Math.* **35,** 155 (1991).
127. E. Bacry, A. Arneodo, U. Frisch, Y. Gagne, and E. Hopfinger, in *Turbulence and Coherent Structures,* edited by M. Lesieur and O. Metais (Kluwer, Dordrecht, 1991), p. 203.
128. M. Vergassola, R. Benzi, L. Biferale, and D. Pisarenko, *J. Phys. A* **26,** 6093 (1993).
129. M. Vergassola and U. Frisch, *Physica D* **54,** 58 (1991).
130. S. Jaffard, *C. R. Acad. Sci. Paris, Serie I: Math.* **326,** 555 (1998).
131. R. Badii, Ph.D. thesis, University of Zurich, 1987.
132. P. Cvitanovic, in *Proceedings Group Theoretical Methods in Physics,* edited by R. Gilmore (World Scientific, Singapore, 1987).
133. M. J. Feigenbaum, M. H. Jensen, and I. Procaccia, *Phys. Rev. Lett.* **57,** 1503 (1986).
134. M. H. Jensen, L. P. Kadanoff, and I. Procaccia, *Phys. Rev. A* **36,** 1409 (1987).
135. A. B. Chhabra, R. V. Jensen, and K. R. Sreenivasan, *Phys. Rev. A* **40,** 4593 (1989).
136. A. B. Chhabra and R. V. Jensen, *Phys. Rev. Lett.* **62,** 1327 (1989).
137. A. B. Chhabra, C. Meneveau, R. V. Jensen, and K. R. Sreenivasan, *Phys. Rev. A* **40,** 5284 (1989).
138. W. H. Press, B. P. Flannery, S. A. Teukolsky, and W. T. Vetterling, *Numerical Recipes* (Cambridge University Press, Cambridge, 1992).

139. N. Decoster, Ph.D. thesis, University of Bordeaux I, 1999.
140. B. B. Mandelbrot and J. W. Van Ness, *S.I.A.M. Rev.* **10,** 422 (1968).
141. J. Beran, *Statistics for Long-Memory Process* (Chapman & Hall, New York, 1994).
142. G. Wornell and A. V. Oppenheim, *IEEE Trans. Signal Proc.* **40,** 611 (1992).
143. R. F. Peltier and J. Levy Véhel, *INRIA Report No. 2396* (1994).
144. P. Flandrin, *IEEE Trans. Inform. Theory.* **35,** 197 (1989).
145. P. Flandrin, *IEEE Trans. Inform. Theory.* **38,** 910 (1992).
146. P. Flandrin, *Temps-Fréquence* (Hermès, Paris, 1993).
147. E. Masry, *IEEE Trans. Inform. Theory.* **39,** 260 (1993).
148. P. Abry, P. Goncalvès, and P. Flandrin, *Lectures Note Statistics.* **105,** 15 (1995).
149. P. Abry, *Ondelettes et Turbulence—Multirésolution, Algorithmes de Décomposition, Invariance d'Echelles et Signaux de Pression* (Diderot Editeur, Arts et Sciences, Paris, 1997).
150. P. Abry and D. Veitch, *IEEE Trans. Inform. Theory.* **44,** 2 (1998).
151. P. Abry, D. Veitch, and P. Flandrin, *J. Time Ser. Anal.* **19,** 253 (1998).
152. L. Abry and P. Delbeke, *Stoch. Proc. Applic.* **86,** 177 (2000).
153. D. Veitch and P. Abry, *IEEE Trans. Inform. Theory.* **45,** 878 (1999).
154. P. Abry, P. Flandrin, M. S. Taqqu, and D. Veitch, in *Self-Similarity in Network Traffic*, edited by K. Parks and W. Willinger (John Wiley & Sons, New York, 1998).
155. A. H. Tewfik and M. Kim, *IEEE Trans. Inform. Theory.* **38,** 904 (1992).
156. J. Pando and L. Z. Fang, *Phys. Rev. E* **57,** 3593 (1998).
157. J. Simonsen, A. Hansen, and O. M. Nes, *Phys. Rev. E* **58,** 2779 (1998).
158. B. Audit, E. Bacry, J. F. Muzy, and A. Arneodo, *IEEE Trans. Inform. Theory* **48,** 2938 (2002).
159. P. Lévy, *Processus Stochastiques et Mouvement Brownien* (Gauthier-Villars, Paris, 1965).
160. R. F. Voss, in *Fundamental Algorithms for Computer Graphics*, edited by R. A. Earnshaw (Springer-Verlag, Heidelberg, 1985), p. 805.
161. A. Arneodo, E. Bacry, and J. F. Muzy, *J. Math. Phys.* **39,** 4142 (1998).
162. M. E. Cates and J. M. Deutsch, *Phys. Rev. A* **35,** 4907 (1987).
163. A. P. Siebesma, in *Universality in Condensed Matter*, edited by R. Julien, L. Peliti, R. Rammal, and N. Boccara (Springer-Verlag, Heidelberg, 1988), p. 188.
164. J. O'Neil and C. Meneveau, *Phys. Fluids A* **5,** 158 (1993).
165. A. Arneodo, E. Bacry, S. Manneville, and J. F. Muzy, *Phys. Rev. Lett.* **80,** 708 (1998).
166. M. Greiner, J. Geisemann, P. Lipa, and P. Carruthers, *Z. Phys. C* **69,** 305 (1996).
167. M. Greiner, J. Geisemann, and P. Lipa, *Phys. Rev. E* **56,** 4263 (1997).
168. J. Lévy-Véhel, *Fractals.* **3,** 755 (1995).
169. J. Lévy-Véhel, in Ref. [10], p. 85.
170. M. Unser and A. Aldroubi, *Proc. IEEE* **84,** 626 (1996).
171. *Wavelet Applications in Signal and Image Processing VIII., Wavelet Applications in Signal and Image Processing VIII., Vol. 4119 of SPIE Conference Proceedings* edited by A. Aldroubi, A. F. Laine, and M. A. Unser (2000).
172. S. Lovejoy, *Science.* **216,** 185 (1982).
173. R. F. Cahalan, in *Advances in Remote Sensing and Retrieval Methods*, edited by A. Deepak, H. Fleming, and J. Theon (Deepak Pub, Hampton, 1989), p. 371.
174. V. Ramanatahn, R. D. Cess, E. F. Harrison, P. Minnis, B. R. Barkston, E. Ahmad, and D. Hartmann, *Science* **243,** 57 (1989).
175. R. D. Cess, G. L. Potter, J. P. Blanchet, G. J. Boer, S. J. Ghan, J. T. Kiehl, M. Le Treut, Z.-X. Li, X.-Z. Lang, J. F. B. Mitchell, J.-J. Morcrette, D. A. Randall, M. R. Riches, E. Roeckner, U. Schlese, A. Slingo, K. E. Taylor, W. M. Washington, R. T. Wetherald, and I. Yagai, *Science* **245,** 513 (1989).
176. F. S. Rys and A. Waldvogel, in *Fractal in Physics*, edited by L. Pietronero and E. Tosatti (North-Holland, Amsterdam, 1986), p. 461.
177. R. M. Welch and B. A. Wielicki, *Clim. Appl. Meteorol.* **25,** 261 (1986).
178. J. I. Yano and Y. Takeuchi, *J. Meteorol. Soc. Jpn.* **65,** 661 (1987).
179. R. M. Welch, K. S. Kuo, B. A. Wielicki, S. K. Sengupta, and L. Parker, *J. Appl. Meteorol.* **27,** 341 (1988).
180. R. F. Cahalan and J. H. Joseph, *Mon. Weather Rev.* **117,** 261 (1989).
181. G. Sèze and L. Smith, in *Proceedings of the Seventh Conference on Atmospheric Radiation*, American Meteorological Society, San Francisco, CA (1990), p. 47.
182. A. Davis, S. Lovejoy, and D. Schertzer, in *Scaling, Fractals and Nonlinear Variability in Geophysics*, edited by S. Lovejoy and D. Schertzer (Kluwer, Dordrecht, 1991), p. 303.
183. Y. Tessier, S. Lovejoy, and D. Schertzer, *J. Appl. Meteorol.* **32,** 223 (1993).
184. A. Davis, A. Marshak, W. J. Wiscombe, and R. F. Cahalan, *J. Geophys. Res.* **99,** 8055 (1994).
185. W. D. King, C. T. Maher, and G. A. Hepburn, *J. Appl. Meteorol.* **20,** 195 (1981).
186. C. Duroure and B. Guillemet, *Atmos. Res.* **25,** 331 (1990).
187. B. Baker, *J. Atmos. Sci.* **49,** 387 (1992).
188. S. P. Malinowski and I. Zawadski, *J. Atmos. Sci.* **50,** 5 (1993).
189. A. V. Korolev and I. P. Mazin, *J. Appl. Meteorol.* **32,** 760 (1993).
190. S. P. Malinowski, M. Y. Leclerc, and D. G. Baumgardner, *J. Atmos. Sci.* **51,** 397 (1994).
191. A. Davis, A. Marshak, W. J. Wiscombe, and R. F. Cahalan, *J. Atmos. Sci.* **53,** 1538 (1996).
192. A. Marshak, A. Davis, W. J. Wiscombe, and R. F. Cahalan, *J. Atmos. Sci.* **54,** 1423 (1997).
193. S. Cox, D. McDougal, D. Randall, and R. Schiffer, *Bull. Am. Meteorol. Soc.* **68,** 114 (1987).
194. B. A. Albrecht, C. S. Bretherton, D. Jonhson, W. H. Schubert, and A. S. Frisch, *Bull. Am. Meteorol. Soc.* **76,** 889 (1995).
195. R. Boers, J. B. Jensen, P. B. Krummel, and H. Gerber, *Quart. J. R. Meteorol. Soc.* **122,** 1307 (1996).
196. H. W. Baker and J. A. Davies, *Remote Sens. Environ.* **42,** 51 (1992).
197. A. Davis, A. Marshak, R. F. Cahalan, and W. J. Wiscombe, *J. Atmos. Sci.* **54,** 241 (1997).
198. R. F. Cahalan and J. B. Snider, *Remote Sens. Environ.* **28,** 95 (1989).
199. S. Lovejoy, D. Schertzer, P. Silas, Y. Tessier, and D. Lavallée, *Ann. Geophys.* **11,** 119 (1993).
200. S. M. Gollmer, M. Harshvardan, R. F. Cahalan, and J. S. Snider, *J. Atmos. Sci.* **52,** 3013 (1995).
201. W. J. Wiscombe, A. Davis, A. Marshak, and R. F. Cahalan, *Proceedings of the Fourth Atmospheric Radiation Measurement (ARM) Science Team Meeting*, Charleston, U.S. Department of Energy 11 (1995).
202. A. Davis, A. Marshak, H. Gerber, and W. J. Wiscombe, *J. Geophys. Res* (1998) Unpublished.
203. D. Lovejoy and S. Schertzer, in *Turbulence and Chaotic Phenomena in Fluids*, edited by T. Tatsumi (North-Holland, Amsterdam, 1984), p. 505.
204. D. Lovejoy and S. Schertzer, in *Fractals: Their Physical Origin and Properties*, edited by L. Pietronero (Plenum, New York, 1989), p. 49.
205. J. Wilson, D. Schertzer, and S. Lovejoy, in *Scaling, Fractals and Nonlinear Variability in Geophysics*, edited by D. Schertzer and S. Lovejoy (Kluwer, Dordrecht, 1991), p. 185.
206. D. Schertzer and S. Lovejoy, in Ref. [10], p. 11.

207. A. Davis, A. Marshak, W. J. Wiscombe, and R. F. Cahalan, *Proceedings of the 2nd Workshop on Nonstationary Random Processes and Their Applications* (1995), preprint.
208. L. M. Romanova, *Izv. Acad. Sci. USSR Atmos. Oceanic Phys.* **11,** 509 (1975).
209. A. Davis, Ph.D. thesis, McGill University, Montreal, 1992.
210. R. F. Cahalan, W. Ridgway, W. J. Wiscombe, T. L. Bell, and J. B. Snider, *J. Atmos. Sci.* **51,** 2434 (1994).
211. R. D. Cess, M. H. Zhang, Y. Zhou, X. Jing, and V. Dvortsov, *J. Geophys. Res.* **101,** 23299 (1996).
212. K. Stamnes, S.-C. Tsay, W. J. Wiscombe, and K. Jayaweera, *Appl. Opt.* **27,** 2502 (1988).
213. R. F. Cahalan, W. Ridgway, W. J. Wiscombe, S. Gollmer, and M. Harshvardan, *J. Atmos. Sci.* **51,** 3776 (1994).
214. A. Marshak, A. Davis, W. J. Wiscombe, and R. F. Cahalan, *J. Geophys. Res.* **100,** 26247 (1995).
215. M. Tiedke, *Mon. Weather Res.* **124,** 745 (1996).
216. A. Davis, A. Marshak, W. J. Wiscombe, and R. F. Cahalan, in *Current Topics in Nonstationary Analysis,* edited by G. Treviño *et al.* (World Scientific, Singapore, 1996), p. 97.
217. M. Harshvardan, B. A. Wielicki, and K. M. Ginger, *J. Climate.* **7,** 1987 (1994).
218. R. F. Cahalan, M. Nestler, W. Ridgway, W. J. Wiscombe, and T. L. Bell, in *Proceedings the 4th International Meeting on Statistical Climatology,* edited by J. Sansom (New Zealand Meteorological Service, Wellington, 1990), p. 28.
219. A. Davis, S. Lovejoy, and D. Schertzer, *SPIE Proc.* **1558,** 37 (1991).
220. A. Marshak, A. Davis, W. J. Wiscombe, and G. Titov, *Remote Sens. Environ.* **52,** 72 (1995).
221. S. G. Roux, Ph.D. thesis, University of Aix-Marseille II, 1996.
222. A. N. Kolmogorov, *C. R. Acad. Sci. USSR.* **30,** 301 (1941).
223. G. Ruiz-Chavarria, C. Baudet, and S. Ciliberto, *Physica D* **99,** 369 (1996).
224. C. H. Meong, W. R. Cotton, C. Bretherton, A. Chlond, M. Khairoutdinov, S. Krueger, W. S. Lewellen, M. K. McVean, J. R. M. Pasquier, H. A. Rand, A. P. Siebesma, B. Stevens, and R. I. Sykes, *Bull. Am. Meteorol. Soc.* **77,** 261 (1996).
225. A. Marshak, A. Davis, R. F. Cahalan, and W. J. Wiscombe, *Phys. Rev. E* **49,** 55 (1994).
226. U. Frisch and S. A. Orszag, *Phys. Today* **24,** (1990).
227. C. Meneveau and K. R. Sreenivasan, *J. Fluid Mech.* **224,** 429 (1991).
228. *Turbulence: A Tentative Dictionary, Turbulence: A Tentative Dictionary,* edited by P. Tabeling and O. Cardoso (Plenum, New York, 1995).
229. K. R. Sreenivasan and R. A. Antonia, *Annu. Rev. Fluid Mech.* **29,** 435 (1997).
230. M. Briscolini, P. Santangelo, S. Succi, and R. Benzi, *Phys. Rev. E* **50,** R1745 (1994).
231. A. Vincent and M. Meneguzzi, *J. Fluid Mech.* **225,** 1 (1995).
232. C. W. Van Atta and W. Y. Chen, *J. Fluid Mech.* **44,** 145 (1970).
233. F. Anselmet, Y. Gagne, E. J. Hopfinger, and R. A. Antonia, *J. Fluid Mech.* **140,** 63 (1984).
234. Y. Gagne, Ph.D. thesis, University of Grenoble, 1987.
235. B. Castaing, Y. Gagne, and E. J. Hopfinger, *Physica D* **46,** 177 (1990).
236. C. Baudet, S. Ciliberto, and Phan Nhan Tien, *J. Phys. II France* **3,** 293 (1993).
237. G. Stolovitzky and K. R. Sreenivasan, *Phys. Rev. E* **48,** R33 (1993).
238. J. Maurer, P. Tabeling, and G. Zocchi, *Europhys. Lett.* **26,** 31 (1994).
239. J. Herweijer and W. Van de Water, *Phys. Rev. Lett.* **74,** 4651 (1995).
240. A. Arneodo *et al.*, *Europhys. Lett.* **34,** 411 (1996).
241. R. Benzi, L. Biferale, G. Paladin, A. Vulpiani, and M. Vergassola, *Phys. Rev. Lett.* **67,** 2299 (1991).
242. P. Kailasnath, K. R. Sreenivasan, and G. Stolovitzky, *Phys. Rev. Lett.* **68,** 2766 (1992).
243. A. Praskovsky and S. Oncley, *Phys. Rev. Lett.* **7,** 3999 (1994).
244. P. Tabeling, G. Zocchi, F. Belin, J. Maurer, and H. Willaime, *Phys. Rev. E* **53,** 1613 (1996).
245. F. Belin, P. Tabeling, and H. Willaime, *Physica D* **93,** 52 (1996).
246. B. Castaing, Y. Gagne, and M. Marchand, *Physica D* **68,** 387 (1993).
247. G. Pedrizetti, E. Novikov, and A. Praskovsky, *Phys. Rev. E* **53,** 475 (1996).
248. R. Benzi, S. Ciliberto, R. Tripiccione, C. Baudet, F. Massaioli, and S. Succi, *Phys. Rev. E* **48,** R29 (1993).
249. R. Benzi, S. Ciliberto, C. Baudet, G. R. Chavarria, and R. Tripiccione, *Europhys. Lett.* **24,** 275 (1993).
250. R. Benzi, S. Ciliberto, C. Baudet, and G. R. Chavarria, *Physica D* **80,** 385 (1995).
251. Y. Gagne, M. Marchand, and B. Castaing, *J. Phys. II France* **4,** 1 (1994).
252. A. Naert, L. Puech, B. Chabaud, J. Peinke, and B. Castaing B. Hebral, *J. Phys. II France* **4,** 215 (1994).
253. B. Chabaud, A. Naert, J. Peinke, F. Chillà, B. Castaing, and B. Hebral, *Phys. Rev. Lett.* **73,** 3227 (1994).
254. B. Dubrulle and B. Castaing, *J. Phys. II France* **5,** 895 (1995).
255. F. Chillà, J. Peinke, and B. Castaing, *J. Phys. II France* **6,** 455 (1996).
256. Y. Malécot, C. Auriault, H. Kahalerras, Y. Gagne, O. Chanal, B. Chabaud, and B. Castaing, *Eur. Phys. J. B* **16,** 549 (2000).
257. O. Chanal, B. Chabaud, B. Castaing, and B. Hebral, *Eur. Phys. J. B* **17,** 309 (2000).
258. A. Arneodo, S. Manneville, J. F. Muzy, and S. G. Roux, *Appl. Comput. Harmonic Anal.* **6,** 374 (1999).
259. R. Peinke and J. Friedrich, *Phys. Rev. Lett.* **78,** 863 (1997).
260. R. Peinke and J. Friedrich, *Physica D* **102,** 147 (1997).
261. P. O. Amblard and J. M. Brossier, *Eur. Phys. J. B* **12,** 335 (1999).
262. P. Marcq and A. Naert, *Phys. Fluids* **13,** 2590 (2001).
263. J. Davoudi and M. R. R. Tabar, *Phys. Rev. Lett.* **82,** 1680 (1999).
264. J. P. Laval, B. Dubrulle, and S. Nazarenko, *Phys. Fluids* **13,** 1995 (2001).
265. I. Arad, B. Dhruva, S. Kurien, V. S. L'vov, I. Procaccia, and K. R. Sreenivasan, *Phys. Rev. Lett.* **81,** 5330 (1998).
266. I. Arad, V. S. L'vov, and I. Procaccia, *Phys. Rev. E* **59,** 6753 (1999).
267. S. Kurien and K. R. Sreenivasan, *Phys. Rev. E* **62,** 2206 (2000).
268. L. Biferale and F. Toschi, *Phys. Rev. Lett.* **86,** 4831 (2001).
269. A. N. Kolmogorov, *J. Fluid Mech.* **13,** 82 (1962).
270. A. M. Obukhov, *J. Fluid Mech.* **13,** 77 (1962).
271. I. Hosokawa and K. Yamamoto, *Phys. Fluids A* **4,** 457 (1992).
272. A. A. Praskovsky, *Phys. Fluids A* **4,** 2589 (1992).
273. S. T. Thoroddsen and C. W. Van Atta, *Phys. Fluids A* **4,** 2592 (1992).
274. S. Chen, G. D. Doolen, R. H. Kraichnan, and Z. S. She, *Phys. Fluids A* **5,** 458 (1992).
275. G. Stolovitzky, P. Kailasnath, and K. R. Sreenivasan, *Phys. Rev. Lett.* **69,** 1178 (1992).
276. G. Sreenivasan and K. R. Stolovitzky, *Rev. Mod. Phys.* **66,** 229 (1994).
277. A. A. Praskovsky and S. Oncley, *Europhys. Lett.* **28,** 635 (1994).
278. S. T. Thoroddsen, *Phys. Fluids* **7,** 691 (1995).
279. S. Chen, G. D. Doolen, R. H. Kraichnan, and L. P. Wang, *Phys. Rev. Lett.* **74,** 1755 (1995).
280. V. Borue and S. A. Orszag, *Phys. Rev. E* **53,** R21 (1996).
281. R. Benzi, R. Struglia, and R. Tripiccione, *Phys. Rev. E* **53,** R5565 (1996).
282. L. P. Wang, S. Chen, J. G. Brasseur, and J. C. Wyngaard, *J. Fluid Mech.* **309,** 113 (1996).
283. A. Tsinober, E. Kit, and T. Dracos, *J. Fluid Mech.* **242,** 169 (1992).
284. L. Shtilman, M. Spector, and A. Tsinober, *J. Fluid Mech.* **247,** 65 (1993).

285. L. Richardson, *Proc. R. Soc. London Ser. A* **110,** 709 (1926).
286. S. Kida, *J. Phys. Soc. Jpn.* **60,** 5 (1990).
287. E. A. Novikov, *Physica A* **2,** 814 (1990).
288. E. A. Novikov, *Phys. Rev. E* **50,** 3303 (1995).
289. B. Dubrulle, *Phys. Rev. Lett.* **73,** 959 (1994).
290. Z. S. She and E. C. Waymire, *Phys. Rev. Lett.* **74,** 262 (1995).
291. B. Dubrulle, *J. Phys. II France* **6,** 1825 (1996).
292. Z. S. She and E. Leveque, *Phys. Rev. Lett.* **72,** 336 (1994).
293. A. B. Chhabra and K. R. Sreenivasan, *Phys. Rev. Lett.* **68,** 2762 (1992).
294. B. Jouault, P. Lipa, and M. Greiner, *Phys. Rev E* **59,** 2451 (1999).
295. D. Sornette, in *Scale Invariance and Beyond*, edited by B. Dubrulle, F. Graner, and D. Sornette (EDP Sciences, Les Ulis, 1997), p. 235.
296. W. X. Zhou and D. Sornette, *Physica D* **165,** 94 (2002).
297. B. B. Mandelbrot, *C. R. Acad. Sci. Paris Ser. A* **278,** 289, 355 (1974).
298. B. B. Mandelbrot, *J. Fluid Mech.* **62,** 331 (1974).
299. J. P. Kahane and J. Peyrière, *Adv. Math.* **22,** 131 (1976).
300. G. M. Molchan, *Commun. Math. Phys.* **179,** 681 (1996).
301. A. Naert, R. Friedrich, and J. Peinke, *Phys. Rev. E* **56,** 6719 (1997).
302. P. Naert and A. Marcq, *Physica D* **124,** 368 (1998).
303. C. Meneveau and K. R. Sreenivasan, *Nucl. Phys.* **B2,** 49 (1987).
304. C. Meneveau and K. R. Sreenivasan, *Phys. Rev. Lett.* **59,** 1424 (1987).
305. C. Meneveau and K. R. Sreenivasan, *Phys. Lett. A* **137,** 103 (1989).
306. E. Aurell, U. Frisch, J. Lutsko, and M. Vergassola, *J. Fluid Mech.* **238,** 467 (1992).
307. G. Paladin and A. Vulpiani, *Phys. Rev. A* **35,** 1971 (1987).
308. C. Meneveau and M. Nelkin, *Phys. Rev. A* **39,** 3732 (1989).
309. U. Frisch and M. Vergassola, *Europhys. Lett.* **14,** 439 (1991).
310. W. Van de Water, B. Van der Vorst, and E. Van de Wetering, *Europhys. Lett.* **16,** 443 (1991).
311. J. Molenaar, J. Herweijer, and W. Van de Water, *Phys. Rev. E* **52,** 496 (1995).
312. I. Hosokawa, S. Oide, and K. Yamamoto, *Phys. Rev. Lett.* **77,** 4548 (1996).
313. A. Bershadskii, T. Nakano, D. Fukayama, and T. Gotoh, *Eur. Phys. J. B* **18,** 95 (2000).
314. A. Bershadskii and A. Tsinober, *Phys. Rev. E* **48,** 282 (1993).
315. A. Bershadskii, E. Kit, A. Tsinober, and H. Vaisburd, *Fluid Dyn. Res.* **14,** 71 (1994).
316. R. Badii and P. Talkner, *Phys. Rev. E* **59,** 6715 (1999).
317. R. Badii and P. Talkner, *Phys. Rev. E* **60,** 4138 (1999).
318. V. L'vov and I. Procaccia, *Phys. Fluids* **8,** 2565 (1996).
319. G. He, S. Chen, R. H. Kraichnan, R. Zhang, and Y. Zhou, *Phys. Rev. Lett.* **81,** 4636 (1998).
320. M. Nelkin, *Phys. Fluids* **11,** 2202 (1999).
321. E. Siggia, *J. Fluid Mech.* **107,** 375 (1981).
322. R. Kerr, *J. Fluid Mech.* **153,** 31 (1985).
323. C. Meneveau, K. R. Sreenivasan, G. P. Kailasnath, and M. S. Fan, *Phys. Rev. A* **41,** 894 (1990).
324. M. S. Shafi, Y. Zhu, and R. A. Antonia, *Phys. Fluids* **8,** 2245 (1996).
325. N. Cao, S. Chen, and K. R. Sreenivasan, *Phys. Rev. Lett.* **76,** 616 (1996).
326. S. Chen, K. R. Sreenivasan, and M. Nelkin, *Phys. Rev. Lett.* **79,** 1253 (1997).
327. S. Chen, K. R. Sreenivasan, M. Nelkin, and N. Cao, *Phys. Rev. Lett.* **79,** 2253 (1997).
328. W. Van de Water and J. Herweijer, *Bull. Am. Phys. Soc.* **41,** 1782 (1996).
329. R. Camussi and R. Benzi, *Phys. Fluids* **9,** 257 (1997).
330. O. N. Boratov and R. B. Pelz, *Phys. Fluids* **9,** 1400 (1997).
331. S. Grossmann, D. Lohse, and A. Reeh, *Phys. Fluids* **9,** 3817 (1997).
332. R. A. Antonia and B. R. Pearson, *Europhys. Lett.* **40,** 123 (1997).
333. B. Dhruva, Y. Tsuji, and K. R. Sreenivasan, *Phys. Rev. E* **56,** R4928 (1997).
334. M. Meneguzzi, Private communication.
335. E. Ott, Y. Du, K. R. Sreenivasan, A. Juneja, and A. K. Suri, *Phys. Rev. Lett.* **69,** 2654 (1992).
336. Y. Du and E. Ott, *Physica D* **67,** 387 (1993).
337. A. L. Bertozzi and A. B. Chhabra, *Phys. Rev. E* **49,** 4716 (1994).
338. M. J. Broeders and A. L. Verbeek, in *Radiological Diagnosis of Breast Diseases*, edited by M. Friedrich and E. Sickles (Springer-Verlag, Berlin, 1997), p. 1.
339. M. H. Dilhuydy and B. Barreau, *Eur. J. Radiol.* **24,** 86 (1997).
340. K. Doi, M. L. Giger, R. M. Nishikawa, K. R. Hoffmann, H. MacMahon, R. A. Schmidt, and K. G. Chua, *Acta Radiol.* **34,** 426 (1993).
341. A. F. Laine, S. Schuler, J. Fan, and W. Huda, *IEEE Trans. Med. Imaging* **13,** 725 (1994).
342. W. Qian, M. Kallergi, L. P. Clarke, H.-D. Li, P. Venugopal, D. Song, and R. A. Clark, *Med. Phys.* **22,** 1247 (1995).
343. R. A. Devore, B. Lucier, and Z. Yang, in *Wavelets in Medicine and Biology*, edited by A. Aldroubi and M. Unser (CRC Press, Boca Raton, FL, 1996), p. 145.
344. J. J. Heine, S. R. Deans, D. K. Cullers, R. Stauduhar, and L. P. Clarke, *IEEE Trans. Med. Imaging* **16,** 503 (1997).
345. H. P. Chan, K. Doi, C. J. Vyborny, R. A. Schmidt, C. E. Metz, K. L. Lam, T. Ogura, Y. Wu, and H. MacMahon, *Invest. Radiol.* **25,** 1102 (1990).
346. D. R. Davies and D. H. Dance, *Phys. Med. Biol.* **35,** 1111 (1990).
347. J. Dengler, S. Behrens, and J. F. Desage, *IEEE Trans. Med. Imaging* **12,** 634 (1993).
348. R. M. Nishikawa, M. L. Giger, K. Doi, C. J. Vyborny, and R. A. Schmidt, *Med. Phys.* **20,** 1161 (1993).
349. A. Bazzani, A. Bevilacqua, D. Bollini, R. Campanini, N. Lanconelli, A. Riccardi, and D. Romani, in *Digital Mammography: IWDM 2000, 5th International Workshop*, edited by M. Yaffe (Medical Physics Publishing, Madison, 2001).
350. N. Karssemeijer, in *Proceedings of the 12th International Conference on Information Processing Medical Imaging*, (Springer-Verlag, Berlin, 1991), p. 227.
351. N. Karssemeijer, *Int. J. Pattern Recog. Artificial Intell.* **7,** 1357 (1993).
352. C. E. Priebe, J. L. Solka, R. A. Lorey, G. W. Rogers, W. L. Poston, M. Kallergi, W. Qian, L. P. Clarke, and R. A. Clark, *Cancer Lett.* **77,** 183 (1994).
353. H. D. Li, M. Kallergi, L. P. Clarke, V. K. Jain, and R. A. Clark, *IEEE Trans. Med. Imaging* **14,** 565 (1995).
354. W. J. H. Veldkamp, N. Karssemeijer, J. D. M. Otten, and J. H. C. L. Hendricks, *Med. Phys.* **27,** 2600 (2000).
355. Y. Wu, K. Doi, M. L. Giger, and R. M. Nishikawa, *Med. Phys.* **19,** 555 (1992).
356. Y. Wu, M. L. Giger, K. Doi, C. J. Vyborny, and R. A. Schmidt, *Radiology* **187,** 81 (1993).
357. H. P. Chan, S. C. B. Lo, B. Sahiner, K. L. Lam, and M. A. Helvie, *Med. Phys.* **22,** 1555 (1995).
358. W. Zhang, K. Doi, M. L. Giger, R. M. Nishikawa, and R. A. Schmidt, *Med. Phys.* **23,** 595 (1996).
359. B. Zheng, W. Qian, and L. P. Clarke, *IEEE Trans. Med. Imaging* **15,** 589 (1996).
360. S. Yu L. Guan, *IEEE Trans. Med. Imaging* **19,** 115 (2000).
361. H. Cheng, Y. M. Lui, and R. I. Feiimanis, *IEEE Trans. Med. Imaging* **17,** 442 (1998).
362. M. A. Gavrielides, J. Y. Lo, R. Vargas-Voracek, and C. E. FloydJr., *Med. Phys.* **27,** 13 (2000).
363. P. K. Saha, J. K. Udupa, E. F. Conant, D. P. Chakraborty, and D. Sullivan, *IEEE Trans. Med. Imaging* **20,** 792 (2001).

364. H. Yoshida, K. Doi, R. M. Nishikawa, K. Muto, and M. Tsuda, *Acad. Rep. Tokyo Inst. Polytech.* **17,** 24 (1994).
365. H. Yoshida, R. M. Nishikawa, M. L. Giger, and K. Doi, *Proc. SPIE.* **2825,** 805 (1996).
366. H. Yoshida, K. Doi, R. M. Nishikawa, M. L. Giger, and R. A. Schmidt, *Acad. Radiol.* **3,** 621 (1996).
367. R. N. Strickland and H. I. I. Hahn, *IEEE Trans. Med. Imaging* **15,** 218 (1996).
368. W. Zhang, H. Yoshida, R. M. Nishikawa, and K. Doi, *Med. Phys.* **25,** 949 (1998).
369. J. M. Lado, P. G. Tahoces, A. J. Mendez, M. Souto, and J. J. Vidal, *Med. Phys.* **26,** 1294 (1999).
370. T. Netsch and H. O. Peitgen, *IEEE Trans. Med. Imaging* **18,** 774 (1999).
371. W. Qian, L. Li, X. Sun, and R. A. Clark, in *Wavelet Applications in Signal and Image Processing VIII, SPIE Conference Proceedings*, edited by A. Aldroubi, A. F. Laine, and M. A. Unser , p. 596–604 (2000).
372. J. K. Park and H. W. Kim, *IEEE Trans. Med. Imaging* **18,** 231 (1999).
373. S. K. Lee, C. S. Lo, C. M. Wang, P. C. Chung, C. I. Chang, C. W. Yang, and P. C. Hsu, *Int. J. Med. Informatics* **60,** 29 (2000).
374. C. B. Caldwell, S. J. Stapleton, D. W. Holdsworth, R. A. Jong, W. J. Weiser, G. Cooke, and M. J. Yaffe, *Phys. Med. Biol.* **35,** 235 (1990).
375. F. Lefebvre, H. Benali, R. Gilles, E. Kahn, and R. Di Paola, *Med. Phys.* **22,** 381 (1995).
376. D. L. Thiele, C. Kimme-Smith, T. D. Johnson, M. McCombs, and L. W. Bassett, *Med. Phys.* **23,** 549 (1996).
377. H. Guillemet, H. Benali, E. Kahn, and R. Di Paola, *Acta Stereol.* **15/2,** 125 (1996).
378. V. Velanovich, *Am. J. Med.* **311,** 211 (1996).
379. J. J. Heine, S. R. Deans, R. P. Velthuizen, and L. P. Clarke, *Med. Phys.* **26,** 2254 (1999).
380. M. Heath, K. W. Bowyer, and D. Kopans*et al.*, in *Digital Mammography*, (Kluwer Academic, Dordrecht, 1998), p. 457.
381. J. N. Wolfe, *Cancer.* **37,** 2486 (1976).
382. A. M. Boyd and N. F. Oza, *Epidemiol. Rev.* **15,** 196 (1993).
383. N. F. Boyd, J. W. Byng, R. A. Jong, E. K. Fishell, L. E. Little, A. B. Miller, G. A. Lockwood, D. L. Tritchler, and M. J. Yaffe, *J. Natl. Cancer Inst.* **87,** 670 (1995).
384. J. J. Heine and R. P. Velthuizen, *Med. Phys.* **27,** 2644 (2000).
385. *Universality in Chaos, Universality in Chaos,* edited by P. Cvitanovic (Hilger, Bristol, 1984).
386. *Chaos, Chaos,* edited by B. L. Hao (World Scientific, Singapore, 1984).
387. H. G. Schuster, *Deterministic Chaos* (Physik Verlag, Weimheim, 1984).
388. P. Bergé, Y. Pomeau, and C. Vidal, *Order within Chaos* (Wiley, New York, 1986).

An Analysis of the Geometric Distortions Produced by Median and Related Image Processing Filters

E. R. DAVIES

Machine Vision Group, Department of Physics, Royal Holloway College, University of London, Egham, Surrey, TW20 0EX, United Kingdom

ISSN 1076-5670/03